Analysis on the main controls and drivers of natural fracture distribution in the Lower Triassic sandstones in the West Netherlands Basin

Frederieke Othilde Tutuarima

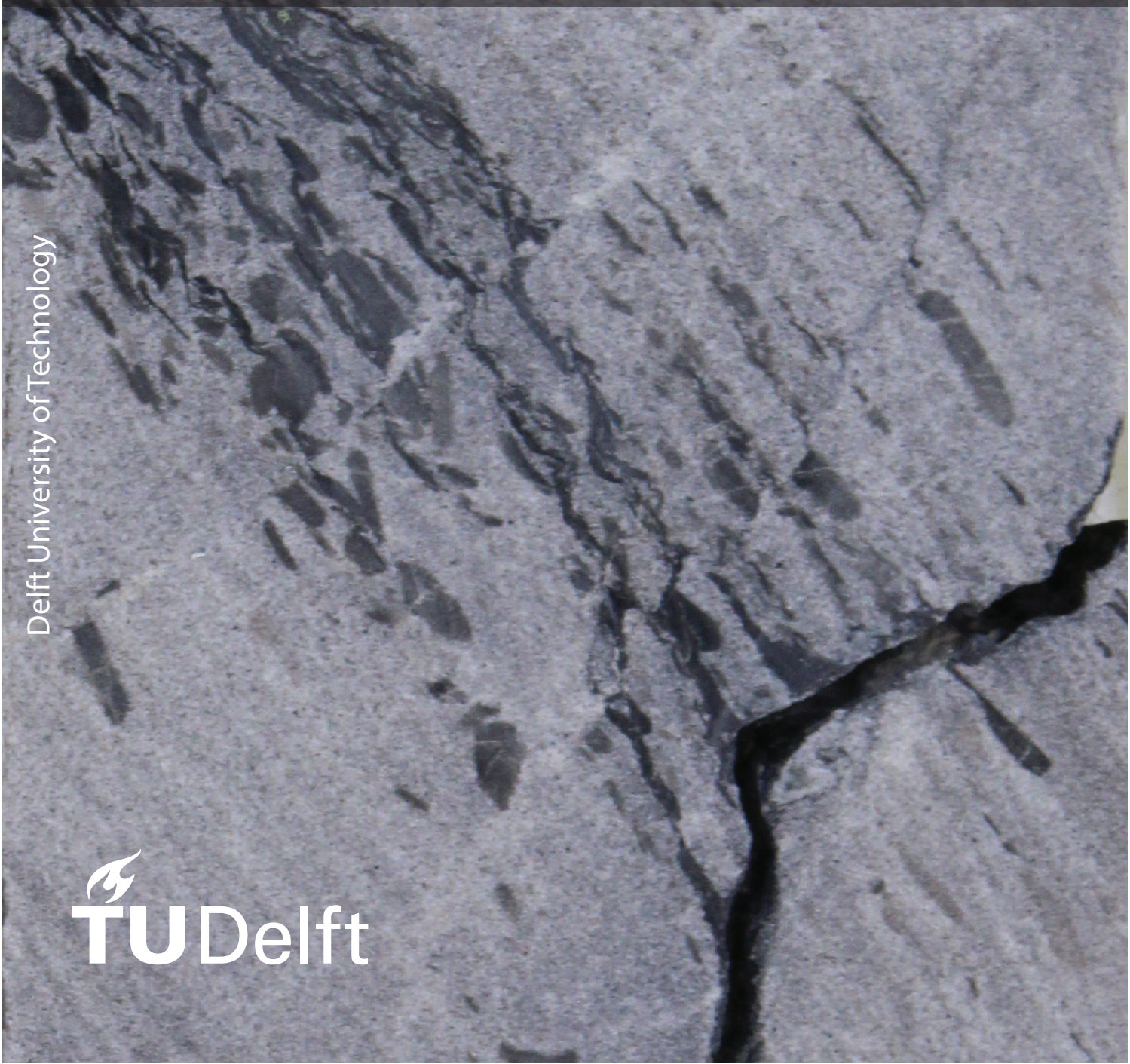

Delft University of Technology

TU Delft

Analysis on the main controls and drivers of natural fracture distribution in the Lower Triassic sandstones in the West Netherlands Basin

by
Frederieke Othilde Tutuarima

Submitted in partial fulfillment
of the requirements for the degree of
Master of Science
in Applied Earth Sciences
Geo-Energy Engineering track

at
Delft University of Technology
2023

To be defended publicly on: 16/06/2023
This thesis is approved by the following members of the Thesis Committee:
Dr. Pierre-Olivier Bruna, Applied Geology
Dr. Hemmo Abels, Applied Geology
Prof.dr. Giovanni Bertotti, Applied Geology
MSc. Emilio Cecchetti, Applied Geology
Dr. Anne Pluymakers, Applied Geophysics and Petrophysics

Abstract

In the geothermal exploration well, NLW-GT-01, in the West Netherlands Basin, a very tight reservoir with low porosity ($\leq$5.0%) and matrix permeability ($\leq$ 0.1mD) has been encountered in the Main Buntsandstein Subgroup. The impact of natural fractures, which can significantly impact fluid flow in tight reservoirs, has been studied. However, there is a lack of consensus in different studies on the fracture classification.

In this study, a re-evaluation is performed of the well data of the NLW-GT-01 and VAL-01 wells. An analysis comparing core, geophysical, and image logs is performed to document the drivers and characteristics of natural fracture distribution in the WNB and investigate the geological and geomechanical parameters influencing the development of fractures in the Main Buntsandstein Subgroup.

On the core of NLW-GT-01 and VAL-01, five types of fractures are classified veins, joints, Mode II fractures, stylolites and drilling-induced fractures. The natural fractures have a dominant NW-SE strike orientation. The drilling-induced fractures and the borehole breakouts indicate a NE-SW oriented in-situ minimum stress and an NW-SE oriented maximum stress. The natural fractures are favourably oriented to be open based on their orientation compared to the in-situ stress orientation.

The fractures are associated with large-scale tectonic events. During the burial of the formation related to the extensional phase of the WNB during the Mesozoic, veins, joints, conjugate fractures, and stylolites could be formed. During the inversion of the basin in the Late Mesozoic-Cenozoic, tectonic stylolites could have been formed, and the previously formed conjugate fractures could have been reactivated.

Natural fractures are concentrated in more heterolithic intervals of the VAL-01 and NLW-GT-01 wells in both image logs and cores. These heterolithic sections display alternations of medium sandstones with silt- and claystones. The identification of more fractures in VAL-01 compared to NLW-GT-01 can be explained by the difference in basin location. VAL-01 is located in the centre of the basin where distal playa environments produced more fine-grained material alternating with coarser sands. The more proximal NLW-GT-01 is dominated by fluvial sands. The lithological variability produces Young's and Shear modulus variability that seems to be driving increased fracture density rather than the absolute value of the Young's modulus causes this.

Preface

With this master's thesis, I will end my Master's Applied Earth Sciences with a specialization in Geo-Energy Engineering. Studying in Delft, especially at this faculty, has been an amazing and unique experience.

For me studying in Delft means having endless opportunities, being encouraged to do new things, going in the field, working with very scarce data sets and implementing uncertainties, but also being thrown in the deep, coming up with creative solutions and being challenged. I have had a great time here and had the pleasure of working with a very nice and open group of students and academics. I am very grateful for everyone I met and everything I have learned over the past years. They say that doing a Master Thesis is one of the most challenging things you will do, but it has also been very rewarding.

I would like to thank Pierre-Olivier Bruna and Emilio Cecchetti for being my supervisors over the past months. Thank you for all your time and help, I have learned a lot from your professional expertise and technical insights but I also learned how to present with confidence, make a conveying story and develop myself as a person. I really enjoyed working closely together with you two! I also want to express my gratitude towards Giovanni Bertotti and Hemmo Abels. They have helped me a lot during our bimonthly meetings, where they had a lot of valuable feedback and advice. Aside from that during my master and bachelor, I have learned a lot from you in different courses! Lastly, I want to thank Anne Pluymakers for her participation in my thesis committee and reviewing my thesis.

Aside from that, I would also like to thank Rien Corstanje, who was a true hero in answering all my questions on the WellCAD program all the way from Kuala Lumpur and Andre Slupnik from TNO, who helped me in the Kernhuis in Zeist.

To conclude, I want to thank my family and friends for supporting me through this process. Especially Sven, my mom and Myrthe, with whom I have shared many conversations, coffee breaks, lunch walks and long phone calls. You have helped me de-stress, stay focused and always brought a smile on my face.

Thank you all!

Frederieke Tutuarima

Contents

List of Figures

List of Tables

Chapter 1

Introduction

1.1 Context of the Study

The subsurface has to be thoroughly evaluated to assess reservoirs for geo-energy purposes such as oil and gas production and geothermal energy. The production potential of these reservoirs relies significantly on the primary porosity and permeability of the formations. In cases where the matrix quality is poor, fractures in reservoirs can significantly impact fluid flow by increasing rock permeability (Nelson, 2001). The fractures form the primary conduits for fluid flow in very tight reservoirs. Interpretation of fractures relies on studying outcrops, evaluating cores, analyzing seismic lines, and examining boreholes. However, accurately characterizing the natural fracture permeability is challenging and varies spatially (Aadnoy & Bell, 1998). These diverse data sets enable the evaluation of fractures across different scales and dimensions. It is essential to correctly characterise the fractures and assess their uncertainty when exploiting them to fully understand their effect.

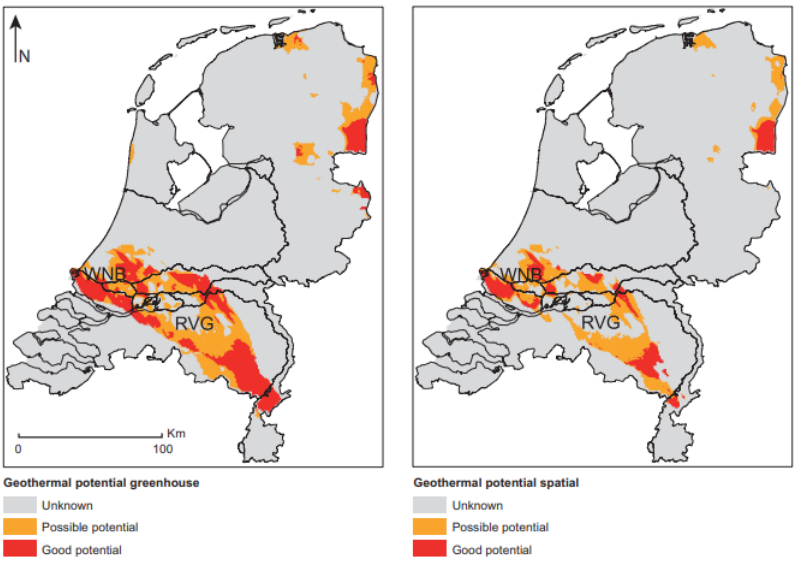

Figure 1.1: Map of the geothermal potential of the Triassic in the Netherlands, with the potential areas for greenhouses (left) and spatial heating (right) (Kramers et al., 2012)

This thesis focuses on the densely populated southern region of the Netherlands, which is characterised by its significant concentration of numerous heat-intense industries and greenhouses (Kramers et al., 2012). This area has a high potential for geothermal energy as it forms a high-demand spot (figure 1.1). Several formations could potentially form suitable aquifers for geothermal production as the Cenozoic, Upper Jurassic-Lower Cretaceous, Triassic, and Rotliegend reservoirs. Furthermore, geothermal heat has been delivered in two geothermal systems within the unexplored hydrocarbon play of the Lower Carboniferous (Dinantian) Limestones (Mijnlieff, 2020).

These aquifers are situated in the West Netherlands Basin (WNB), part of a wide-ranging system of transtensional basins (de Jager, 2007). Of these aquifers, the Main Buntsandstein Subgroup is situated at a depth between 2-4 km and has temperatures from 60-120° C. It is geologically more complex due to its multi-phased diagenetic history (Purvis & Okkerman, 1996a). In 2017, a well (NLW-GT-01) was drilled to explore its geothermal potential. Here a very tight reservoir with low porosity ($\leq 5.0\%$) and matrix permeability (≤ 0.1 mD) was encountered (Felder & Fernandez, 2018; Boersma et al., 2021).

Geothermal production from fractures in tight reservoirs has already been exploited in the northwest of Europe. In the Upper Rhine Graben, for example, geothermal production is related to naturally fractured rock or enhanced geothermal systems (Vidal & Genter, 2018), and in the Lower Carboniferous Limestone in the Campine Basin, partially cemented fractures are essential for the geothermal reservoir potential in the Balmatt project (Swennen et al., 2021).

The impact of natural fractures to unlock the geothermal potential of the Main Buntsandstein in the WNB has been studied by Boersma et al. (2021). They concluded that the assumed-to-be open fractures observed in the NLW-GT-01 could substantially increase the effective permeability and provide sufficient heat production from the Main Buntsandstein in this area. Potentially open fractures interpreted from image analysis in another well (VAL-01) in the WNB by a study performed by Atlas Geoscience (1998) support that interpretation.

However, there is a lack of consensus in different studies on fracture assessment in these wells (Kourta & Jocker, 2018; Vinci, 2018; Boersma et al., 2021), which makes the fracture studies uncertain. The number of interpreted natural open fractures ranges from over 300 to a small 58 in NLW-GT-01 over the image log interval by Schlumberger (2017) and Boersma et al. (2021), respectively. This can be attributed to a misclassification of natural and drilling-induced fractures.

1.2 Research Objective

A concordant classification is critical for accurately interpreting the natural fracture densities and assessing the open fractures, which could contribute to enhanced natural permeability by the fractures. This study re-evaluates the well data from NLW-GT-01 and

VAL-01 to address these discrepancies and assess the open natural fractures. Aside from that, it is crucial to note that the small-scale features identified in these wells are limited to their immediate surroundings (Boersma et al., 2020). Therefore, integrating data from different locations and scales is necessary to assess the fractures in the West Netherlands Basin.

This study aims to document the drivers, controls, and characteristics of natural fracture distribution in the West Netherlands Basin (WNB) and to investigate the geological and geomechanical parameters that influence the development of fractures in the Main Buntsandstein Subgroup, which can be used to optimise the planning of future geothermal doublets and to de-risk upcoming operations.

In order to reach our goals, the following research questions are proposed:

- Which natural and drilling-induced fractures are classified in the core and image logs of NLW-GT-01 and VAL-01?
- What are the drivers and controls on natural fracture distribution?
- How are the fractures related to the tectonic history of the basin?

1.3 Report Structure

This study consists of 8 chapters. Chapter 1 briefly introduces the research project, including the research questions and an overview of the report. Chapter 2 provides background information on the geological history of the study area. All the available data are discussed in Chapter 3. In Chapter 4, the workflow of this project is discussed, explaining the data acquisition of core, image log, and wireline logs, the data integration and the method to classify the fractures, and identify the controls and drivers of fracture generation. Chapter 5 gives the results of the lithological description, fracture characterisation, and geomechanical properties for the two wells NLW-GT-01 and VAL-01 and discusses the relative chronology of the fractures in NLW-GT-01, the structural drivers of fracture generation and controls on fracture distribution in the Main Buntsandstein in the West Netherlands basin. Chapter 6 contains the discussion, and the conclusion will be discussed in chapter 7.

Chapter 2

Geological Background

2.1 Present-day Situation

The West Netherlands Basin (WNB) is located in the southwestern part of the Netherlands and the adjacent offshore areas with an NW-SE trend (van Balen et al., 2000; de Jager, 2007)(figure 2.1). The London Brabant Massif and the Oosterhout Platform form the southern boundaries of the basin by a clear series of normal faults (Kombrink et al., 2012). In the north, the Zandvoort Ridge and Ijmuiden High separate the WNB from the Central Netherlands Basin and the offshore Broad Fourteens Basin by a series of normal faults (Kombrink et al., 2012). The transition to the Indefatigable Platform runs across different fault blocks(Kombrink et al., 2012). To the southeast, the basin merges into the Roer Valley Graben (Geluk et al., 1996; van Balen et al., 2000; de Jager, 2007; Kombrink et al., 2012; Willems et al., 2020).

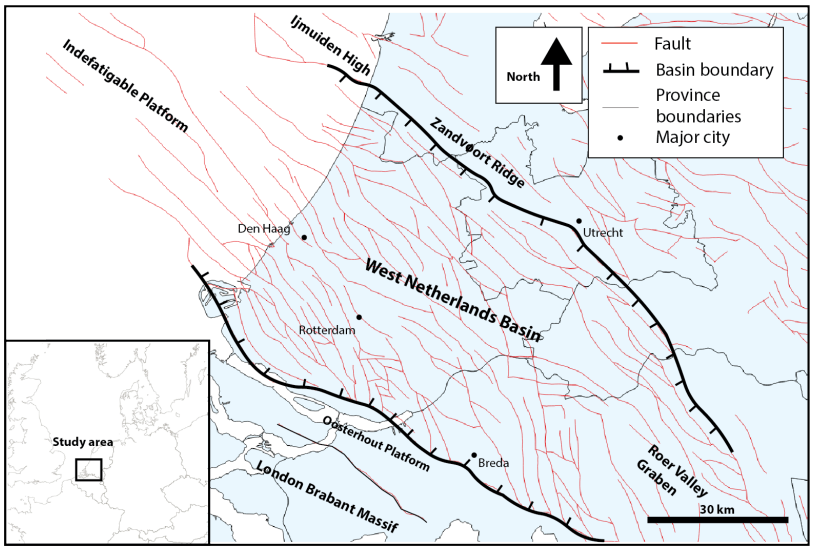

Figure 2.1: Fault map showing the present-day setting of the West Netherlands Basin (https://www.dinoloket.nl/en/subsurface-models)

The WNB is characterized by up to 5000 m thick Permian to Tertiary deposits (Worum et al., 2005; de Jager, 2007). Most faults in the WNB were inverted from an extensional to a compressional regime by dextral and sinistral transpression, forming a 50 km wide and 250 km long, complex horst and graben system (Worum et al., 2005; de Jager, 2007; Pharaoh et al., 2010). The present-day maximum horizontal stress is oriented NE-SW (Heidbach et al., 2018).

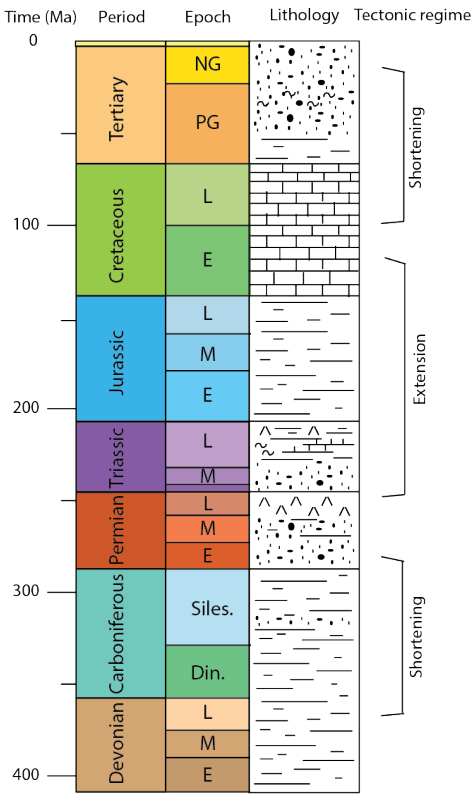

Figure 2.2: Schematic overview of the geological history of the West Netherlands basin (after de Jager, 2007 and dinoloket.nl)

2.2 Structural History

The West Netherlands Basin formed in response to three tectonic phases during the Early Permian, the Mesozoic, and the Late Mesozoic-Cenozoic. The initial foundation structure of the WNB was formed in the Paleozoic by the assembly of Pangea (van Wijhe, 1987; Pharaoh et al., 2010). During the Saalian event in the Stephanian-Early Permian, wrench faulting led to the reactivation of the Paleozoic NW-SE faults and developed a conjugate set with NE-SW to NNE-SSW strikes (van Wijhe, 1987; van Balen et al., 2000; Worum et al., 2005; de Jager, 2007).

During the Mesozoic, Pangea began to split due to an E-W-oriented extensional regime (de Jager, 2007), which led to the opening of the Tethys and North Atlantic oceans (Worum et al., 2005). The rifting occurred during the Triassic (Geluk, 1998; de Jager, 2007) in four phases: the Hardegsen phase, the Early-, the Mid-, and the Late-Kimmerian phase. This rifting phase created the West Netherlands Basin as a system of grabens with an N-S to NW-SE strike (van Wijhe, 1987; Geluk, 1998; van Balen et al., 2000; de Jager, 2007).

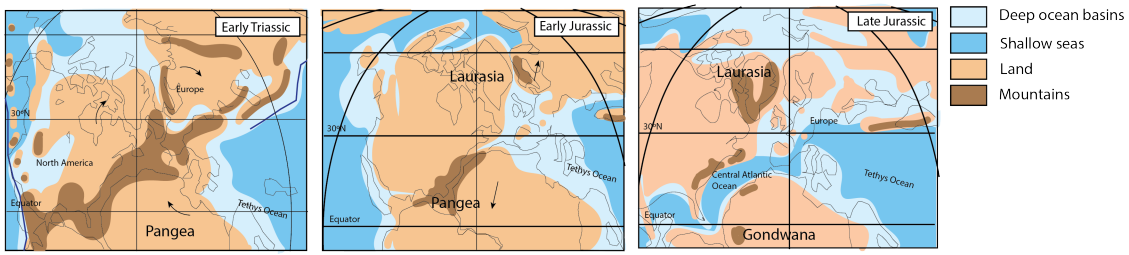

Figure 2.3: Schematic overview of Western Europe during the rifting of Pangea (after Scotese and McKerrow 1990)

Crustal extension across the North Sea graben system decreased gradually during the Early Cretaceous and ended during the Aptian to Albian (van Wijhe, 1987; van Balen et al., 2000; Pharaoh et al., 2010). During the Late Aptian-Santonian, the WNB was tectonically quiescent and subsided regionally (van Wijhe, 1987). During the Late Cretaceous, the WNB was inverted in three tectonic phases (van Balen et al., 2000; Worum et al., 2005; de Jager, 2007; Kilhams et al., 2018), alternating with periods of tectonic quiescence (van Wijhe, 1987). Compressional and transpressional stresses reactivated pre-existing N-S to NW-SE trending faults from the Late Jurassic and Early Cretaceous (van Wijhe, 1987; de Jager, 2007).

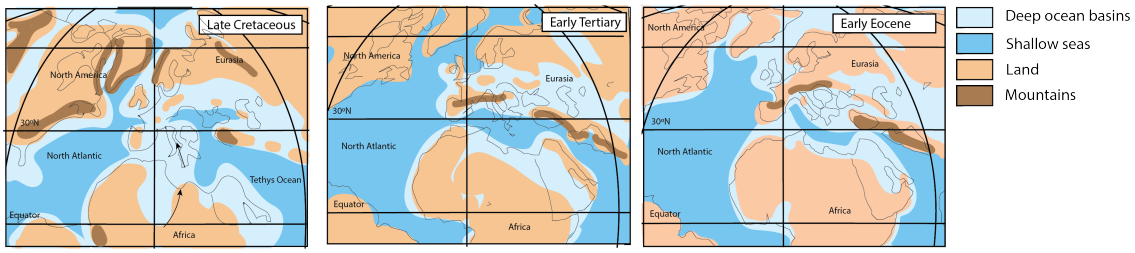

Figure 2.4: Schematic overview of Western Europe during the inversion of the West Netherlands Basin (after Scotese, 1990)

This period is followed by a period of regional subsidence (van Wijhe, 1987; van Balen et al., 2000; de Jager, 2007). This relaxation of the stresses resulted locally in normal reactivation of the faults (de Jager, 2007).

2.3 The Main Buntsandstein Subgroup

The Main Buntsandstein Subgroup is part of the Lower Germanic Trias Group and consists of the Volpriehausen, Detfurth, and Hardegsen Formations. This thesis focuses on the Volpriehausen and Detfurth Formation, originating from the Olenekian (TNO-GDN, 2023b, 2023a). These sediments were deposited through fluvial systems in an endhoeric basin in arid to semi-arid conditions (Purvis & Okkerman, 1996a; Geluk, 1998, 2005). A major fluvial system in the south-eastern Netherlands supplied clastics during the Early to Middle Triassic with additional clastics from the London Brabant Massif (Geluk et al., 1996; Geluk, 1998, 2005).

2.3.1 Volpriehausen Formation (RBMV)

The Volpriehausen Formation is a 100-200 m thick formation consisting of the Lower Sandstone, the Upper Sandstone, and the Clay-Siltstone Formation. The Lower Volpriehausen Sandstone is grey arkosic, fine to medium-grained with occasional silt lamination's, an abundance of small-scale mud clasts, and a quartz content of just below 50% (Geluk, 2005; Matev, 2011). It is cemented by high percentages of calcite and dolomite (Geluk et al., 1996; Matev, 2011; TNO-GDN, 2023b) and has an average porosity of up to 10% in the WNB (Geluk et al., 1996). The Upper Volpriehausen Sandstone is a sandstone that

contains several claystone intercalations and mud clasts (Geluk & Röhling, 1997; Matev, 2011). It is generally a more reddish brown, silty sandstone with dolomite, anhydrite, and ankerite cement (Geluk et al., 1996; Geluk, 2005). The sandstones are deposited in a fluvial and aeolian environment (Geluk & Röhling, 1997; Geluk, 1998, 2005; TNO-GDN, 2023b).

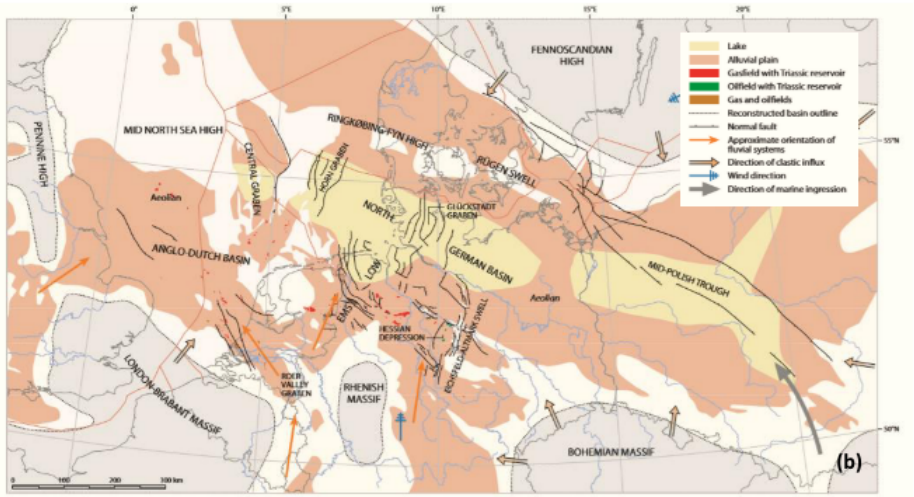

Figure 2.5: Distribution of depositional facies of the main Buntsandstein subgroup in Europe (Bachmann et al., 2010)

In the southwestern region of the WNB, the formation is more sand-rich, implying a proximal position to the major fluvial system. At the same time, thick claystones define the Volpriehausen Formation towards the south-eastern area, indicating a more distal location from the main channel (figure 2.6) (Geluk, 2005; Maniar, 2019; Matev, 2011). To the north and east, the Volpriehausen Sandstone grades into the Clay-Siltstone formation, which is formed by a succession of predominantly lacustrine siltstones and claystones with subordinate sandstones.

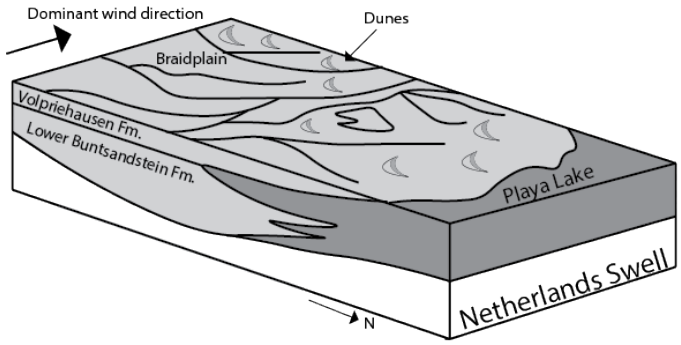

Figure 2.6: Depositional model for the Lower Buntsandstein and Volpriehausen Formation in the southern Netherlands. Light shading is predominantly sandstones; darker shading indicates predominantly claystones (Geluk et al., 2005)

2.3.2 Detfurth Formation (RBMV)

The Detfurth Formation comprises a Lower Sandstone member, a Claystone member, and an Upper Sandstone member (TNO-GDN, 2023a) with a total thickness between 20-60 m in the WNB (Geluk et al., 1996; TNO-GDN, 2023a). The Lower Detfurth Sandstone member is a massive basal sandstone (Geluk, 1998, 2005; TNO-GDN, 2023a), deposited in a fluvial and aeolian environment (Geluk & Röhling, 1997). It is one of the best reservoir intervals in the Main Buntsandstein Subgroup, according to Geluk et al. 1996. The unit is quartz cemented and has an average porosity of 15-20% measured in the West Netherlands Basin (Geluk et al., 1996; TNO-GDN, 2023a) with a quartz grain content of up to 60%.

The Detfurth Claystone represents the expansion of lacustrine conditions over the area during a more humid period. It consists of homogeneous anhydritic claystones with intercalations of siltstone, which, in the southern off- and onshore, grade into aeolian sandstones (Geluk, 1998, 2005; TNO-GDN, 2023a). The Detfurth shows a transition from the fluvial-dominated Volpriehausen to the more aeolian desert environment in the Hardegsen indicating a general shift towards a more arid environment (Geluk, 2005; Matev, 2011).

2.4 Geothermal Potential

The Main Buntsandstein Subgroup is one of the Triassic intervals containing potential geothermal reservoirs. However, the transmissivity of the Triassic reservoirs is generally low, smaller than 2 Dm (ThermoGis-v2.1, 2018). The reservoir quality, porosity, and permeability are primarily related to the facies and depositional environment of the sediments. The reservoir quality is subsequently significantly modified due to diagenetic processes like compaction, cementation, and dissolution (Mijnlieff, 2020).

The initial porosity at the time of deposition of the Main Buntsandstein Subgroup was between 10-20% (Geluk et al., 1996). During early diagenesis, the formation is cemented and compacted (Bath et al., 1987; Purvis & Okkerman, 1996b; Spain & Conrad, 1997; Kunkel et al., 2018). During the late diagenesis phase, the framework grains become overall more tightly packed due to mechanical compaction with continued burial (Maniar, 2019). Late Cretaceous–Paleogene erosion down to Triassic strata resulted in renewed near-surface conditions, where leaching by meteoric water led to intergranular porosity and permeability (Bath et al., 1987; Purvis & Okkerman, 1996b; Spain & Conrad, 1997; Mijnlieff, 2020).

In general, only the basin fringes of the Main Buntsandstein distributional area have a the transmissivity higher than the minimum threshold of 10 Dm. However, based on the mapped Triassic reservoirs, Thermo-Gisv2.1 gives an estimated Heat Initial in Place (HIP) of 334,930 PJ of source potential (Mijnlieff, 2020). The permeability created by fracture networks can target this potential heat. In Germany, four projects targeting the Triassic sandstones have been realized in the Upper Rhine Graben, the eastern extent of the Roer Valley Graben. These four projects produce geothermal water from highly fractured damage zones around faults (Rijkers et al., 2014). It is, therefore, interesting to further investigate the impact of fractures on the geothermal potential in the WNB.

Chapter 3

Available Data

This chapter provides an overview of the well data, its quality, and the seismic data. Based on this, the subsequent analysis will be performed, and interpretations will be made.

3.1 Well Data

3.1.1 Locations

Two wells, one located at the basin's edge (NLW-GT-01) and the other in the centre of the basin (VAL-01), are used to describe and interpret the fracture characteristics of the Main Buntsandstein in the West Netherlands Basin (figure 3.1).

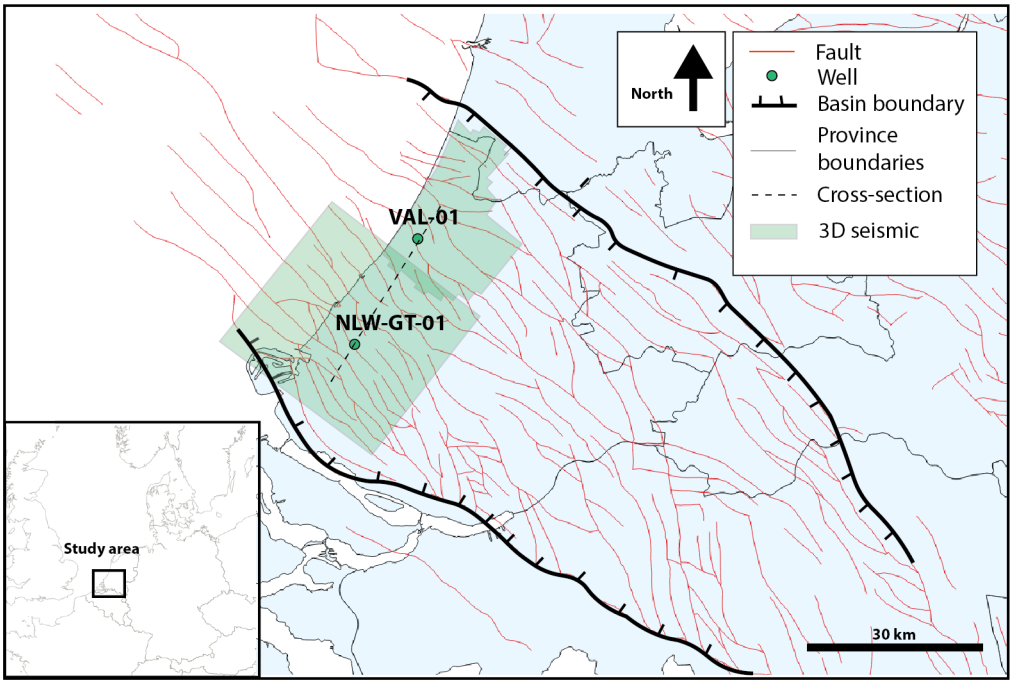

Figure 3.1: Fracture map with well locations NLW-GT-01 and VAL-01 (https://www.dino loket.nl/en/subsurface-models)

3.1.2 Data Overview

Table 3.1 shows an overview of the available data used in this project. The wireline logs, image logs, core photos, and well data are publicly available on nlog.nl, a database for subsurface data in the Netherlands. The cores and polymer slabs are stored and available for analysis at the Centraal Kernhuis of TNO in Zeist.

Table 3.1: Overview of available data on NLW-GT-01 and VAL-01

	Core	**Wireline logs**						**Image log**
		Gamma Ray	**Caliper**	**Neutron**	**Density**	**Sonic**	**Resistivity**	
NLW-GT-01	x	x	x	x	x	x	x	FMI
VAL-01	x	x	x	x	x	x	x	AST

In 1998, the NAM drilled the VAL-01 well to a depth of 3222 m in Valkenburg for the exploration of hydrocarbons, where they explored the Delftland (Lower Cretaceous), Buntsandstein (Triassic), and Rotliegend Formations (Permian). Over the Triassic interval from 2646.0 m MD to 3216 m MD, wireline tests and an image log were made. Aside from that, a 59.7 m long core covering depths between 2820.8-2881 m MD was acquired. The core covers 6 m of the Hardegsen Formation, 31 m Detfurth Formation and 22 m of the Volpriehausen Formation. The well deviates with a dip direction of 210° at a dip angle of 15° over the Triassic interval.

Table 3.2: Overview of well information on NLW-GT-01 and VAL-01 (nlog.nl)

Well	**NLW-GT-01**	**VAL-01**
Company	Trias Westland B.V.	NAM
Drilling contractor	KCA Deutag Drilling Ltd	KCA Deutag Drilling Ltd
Country	The Netherlands	The Netherlands
Start of drilling	09-11-2017	03-04-1998
Type of drilling	Geothermal exploration	Hydrocarbon exploration
Status	Completed to Cretaceousreservoir	Abandoned
Total depth	4447.00 m t.o.v. Rotary table	3222.00 m t.o.v. Kelly Bushing
Result drilling	Water	Dry
Vertial position of Kelly Bushing / Rotary table	8.42 t.o.v NAP	7.57 t.o.v. NAP
Borehole trajectory	Deviated	Deviated

In 2017, the NLW-GT-01 well was drilled for geothermal energy to a depth of 4 km by Trias Westland (Trias Westland, 2017). The well aimed to explore and research both the Lower Cretaceous sandstone at a depth of 2.5 km and the Triassic at a depth of 4 km, to decrease the risk in future explorations projects (Trias Westland, 2017). Well logs and an image log were acquired over the Triassic interval from 4060 m MD to 4447 m MD. Aside from that, a 29.7 m long core covering depths between 4250-4279.7 m MD was acquired. The core covers 5 m of the Detfurth Formation and 25 m of the Volpriehausen Formation. The well deviates over the Triassic interval with an orientation of a dip direction of 70° at a dip angle of 40° (Schlumberger, 2018).

3.1.3 Data Quality

Wireline Logs

The different wireline logs have a range of resolutions. The depth of investigation can differ from 0-250 cm into the formation, and the vertical sampling distance from 1-80 cm. In figure 3.2, the depth of investigation and the vertical resolution are given for the Gamma Ray, Caliper, Neutron, Density, Sonic, and Resistivity log (Mazaheri et al., 2015).

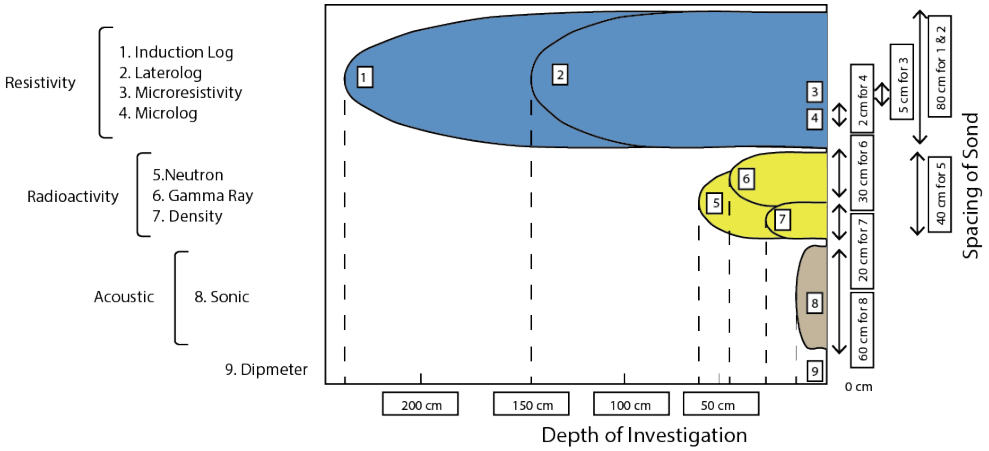

Figure 3.2: Depth of investigation and resolution of different petrophysical logs, redrawn from Darling (2005) by Mazaheri et al., 2015

Image Logs

Two tools are used for acquiring images in NLW-GT-01 and VAL-01 , one based on electrical resistivity (FMI) and the other on acoustic imaging methods (AST). Acoustic image logs provide an oriented image with a resolution of the order of 1 cm. The oriented FMI image has a vertical resolution down to 5 mm (Haller & Porturas, 1998; Goodall et al., 1998; Prioul & Jocker, 2009; Lai et al., 2018; Teama et al., 2018), vertical sampling of 0.1 mm, and a depth of investigation of 30 cm (Teama et al., 2018).

On the AST, the contrast in amplitude are represented (Geoscience, 1998). High impedance indicates high-density or non-porous media and low impedance porous and low-density formations. The resistivity is a function of grain size, porosity, cementation, and mineralogy, as well as borehole size, shape, and surface features. For rocks of similar mineralogy cementation and fluid type, the pixel tone of the image is observed to be a function of grain size (Gonçalves & Ewert, 1998; Khoshbakht et al., 2012; Teama et al., 2018).

Electrical images can be displayed using two types of colour designation (dark colour represents low resistivity and light colour represents high resistivity (Major et al., 1998; Lai et al., 2018)), one where the colour range covers the entire resistivity population (static) and the other where the sampled population is limited to the resistivity values over a specified depth interval (dynamic) (Goodall et al., 1998; Mahmood et al., 2023).

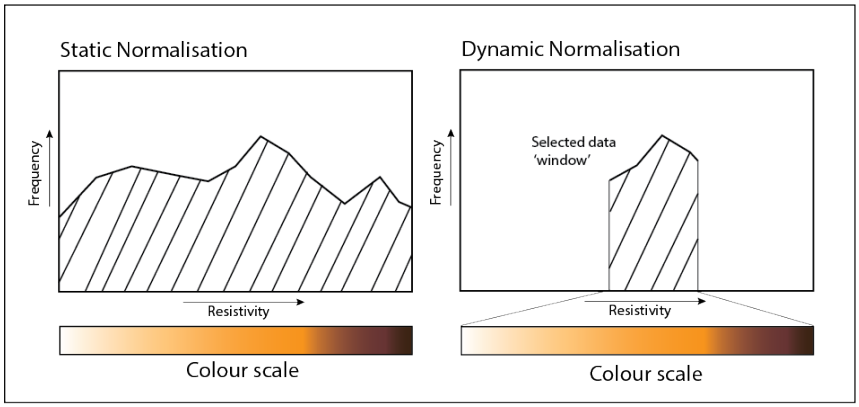

Figure 3.3: Colour designation of Static and Dynamic Normalization of electrical resistivity data (after Goodall et al., 2018)

The two types of image display are complementary for comparison with core data: dynamic normalisation is used for detailed comparisons of sedimentary structures, rock fabric details, and bedding information, while static normalisation is preferred for correlating lithological, structural changes or facies changes at compressed vertical scales (Goodall et al., 1998; Lai et al., 2018; Mahmood et al., 2023).

3.2 Seismic lines

A composite line from two different seismic surveys, L3NAM2001AR-1 (around VAL-01) and L3NAM 2016CR-1 (around NLW-GT-01), has been realized. The composite line is going SW-NE from Naaldwijk (NLW-GT-01) to Valkenburg (VAL-01) perpendicular to the basin. The interpretation of the horizon tops is from the DGM-diep V4 seismic interpretations (https://www.nlog.nl/dgm-diep-v4-onshore), where the Main Buntsandstein is situated between the Altena and the Lower Triassic horizons. A basic fault interpretation has been made based on this composite line.

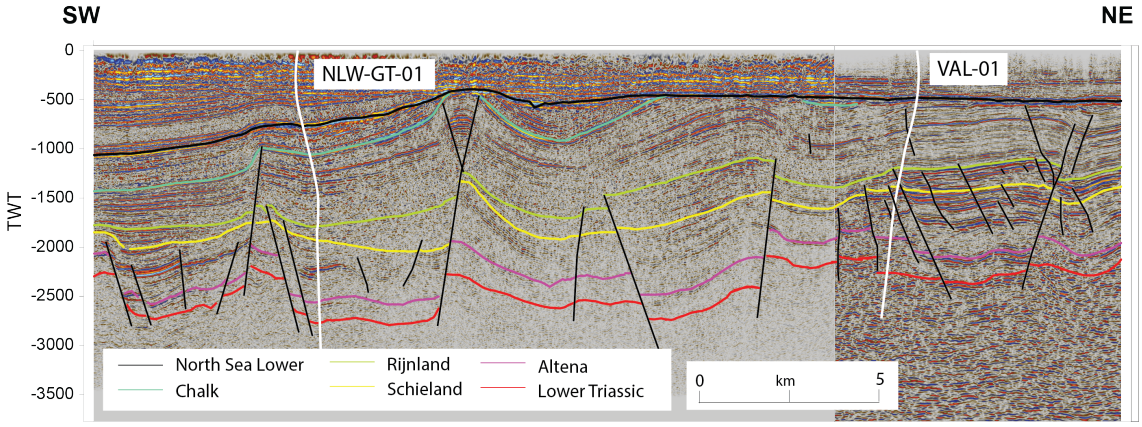

Figure 3.4: Geological cross-section across the WNB from SW-NE including NLW-GT-01 and VAL-01 and the horizons (DGM4) and fault interpretation

Chapter 4

Method

The core, image logs and wireline logs are evaluated to assess the lithology, the fractures and the geomechanical properties of the rock (figure 4.1). This workflow is applied to two wells, NLW-GT-01 and VAL-01, to identify the main controls and drivers of natural fractures in the Main Buntsandstein in the West Netherlands Basin. This chapter goes into the methods applied in each step of the analysis.

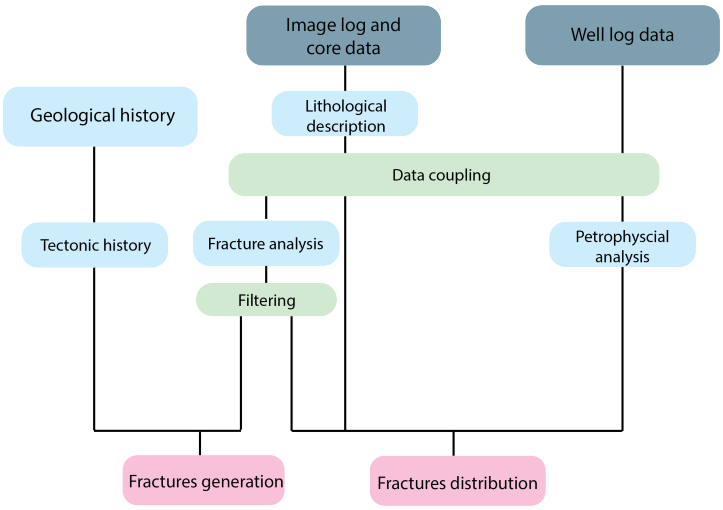

Figure 4.1: Overall workflow for this thesis. The main steps involve 1) core analysis, 2) image log analysis, 3) petrophysical analysis, 4) data coupling and filtering. See the text for additional details on the data and each analysis step.

4.1 Core Analysis

The core is analysed at a cm to mm scale to capture heterogeneities at the scale of the fractures.

For the lithological description, the grain size was mapped over the core interval according to Wentworth, 1922. The lithofacies and set boundaries were identified based on grain

size distribution, lithology, and texture. Sedimentary structures and bioturbated sections were noted.

For the structural analysis, the depth of each discontinuity is measured at the centre of the core slab. The sense of movement, the mineralisation, and the smoothness of the discontinuity plane are marked and the orientation, length, aperture and offset are measured.

4.2 Log Analysis

For this project, the wireline logs are used to estimate the lithology, the fractures, and the geomechanical properties.

4.2.1 Gamma Ray and Density Logs

A Gamma Ray log measures the natural emission of gamma rays of a formation. Elements such as uranium, thorium, and potassium in claystones are responsible for most natural radioactivity. However, other rocks, such as carbonates and feldspar-rich rocks, are also radioactive. The Gamma Ray log is used to interpret sandstones with typically 20-40 API gamma ray emissions, and claystones over 100 API (Schlumberger, n.d.). This can be used to depth match the core and the wireline logs.

The Bulk Density of the formation is a measurement based on the reduction in gamma ray flux between a source and a detector. Several factors influence the bulk density of the formation. The lithology and mineralogy, as different rock types, have varying densities. The porosity of the formation, where a higher porosity of the formation leads to lower densities and vice-versa. The porosity can be affected by compaction and diagenesis (Schlumberger, 2001). The Density log is used to compute the geomechanical logs.

4.2.2 Image Logs

This study uses an image log to identify individual fractures on a borehole wall. The image logs are analysed in WellCAD for fracture and bedding picking (Appendix A.1). On an unwrapped image log, planar features as bedding planes and fractures appear as sine waves. The sine wave amplitude indicates the dip magnitude, and the low point of the wave describes the dip direction (or azimuth) (Goodall et al., 1998; Haller & Porturas, 1998; Teama et al., 2018; Lai et al., 2018; Mahmood et al., 2023).

On the AST, the contrast in amplitude are represented (Geoscience, 1998). High impedance indicates high-density or non-porous media and low impedance porous and low-density formations. Discontinuities are characterised with low impedance sinusoidal waves on AST images (Lai et al., 2018).

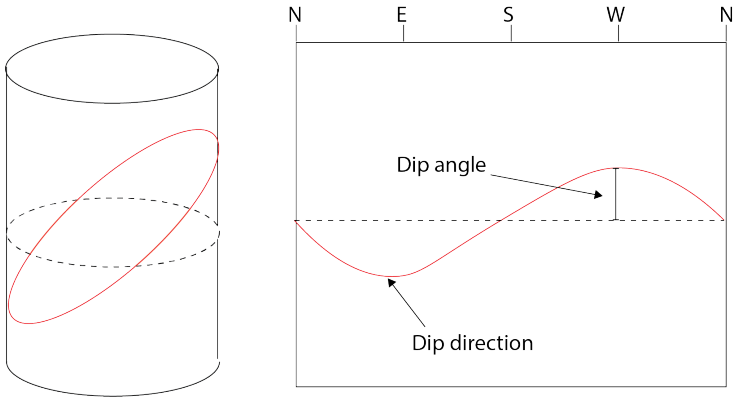

Figure 4.2: Fracture appearance on an unwrapped image log

Depending on the resolution and the difference in resistivity of the fracture and formation, fractures can be identified (Khoshbakht et al., 2012). The appearance of the fractures can give an indication of the fracture cementation and type:

- Due to the intrusion of conductive drilling mud into the fracture or due to pyrite cement, open fractures in a clay-free formation appear to be low resistive in the images (Haller & Porturas, 1998; Lai et al., 2018; Mahmood et al., 2023).
- When a fracture is cemented by calcite or anhydrite, the fractures appear resistive. When it is cemented with quartz is will appear less resistive (Gonçalves & Ewert, 1998; Haller & Porturas, 1998; Mahmood et al., 2023).
- Partially open fractures have discontinuous sinusoidal wave appearances on image logs (Haller & Porturas, 1998).
- In gas-bearing sections on the dynamically normalised image, fractures may appear conductive. This is misleading as the fractures are resistive (and cemented), but the matrix is even more resistive due to the very high gas content (Haller & Porturas, 1998; Lai et al., 2018).
- Most stylolites are non-planar, and recognition of non-planar and thin features in FMI is challenging (Khoshbakht et al., 2012).

In the FMI images, fractures are classified as high-resistibe, low-resistive, and shear fractures based on their appearance in the image log and the hydraulic conductivity. On the AST logs, this differentiation is not made.

4.2.3 Acoustic Logs

Geomechanical properties are properties describing the deformation and strength of a rock. A rock can be deformed by applied stresses when it exceeds the rock's strength by either compressional, tensile, or shear stresses. Strain is a measure of the deformation due to the

applied stress. The geomechanical properties are calculated based on the V_p, the V_s, and the density logs (ρ) according to the following equations (Hunfeld et al., 2021):

$$\text{Poisson's ratio}: \quad \nu = \frac{V_p^2 - 2V_s^2}{2(V_p^2 - V_s^2)} \tag{4.1}$$

$$\text{Shear modulus}: \quad G = \rho V_s^2 \tag{4.2}$$

$$\text{Young's modulus}: \quad E = 2G(1-\nu) \tag{4.3}$$

$$\text{Bulk modulus}: \quad K = \frac{E}{3(1-2\nu)} \tag{4.4}$$

Poisson's ratio gives the ratio of relative change in the radius and height of the rock. Shear modulus is the resistance to shearing deformation under applied stress. Young's modulus, similar to Poisson's ratio, gives the ratio of axial stress and resulting strain. The Bulk modulus is the stress over the volumetric strain. In figure 4.3, an overview of the geomechanical properties is given with the changes in stress and strain. A manual for this computation in WellCAD is given in Appendix A.2.

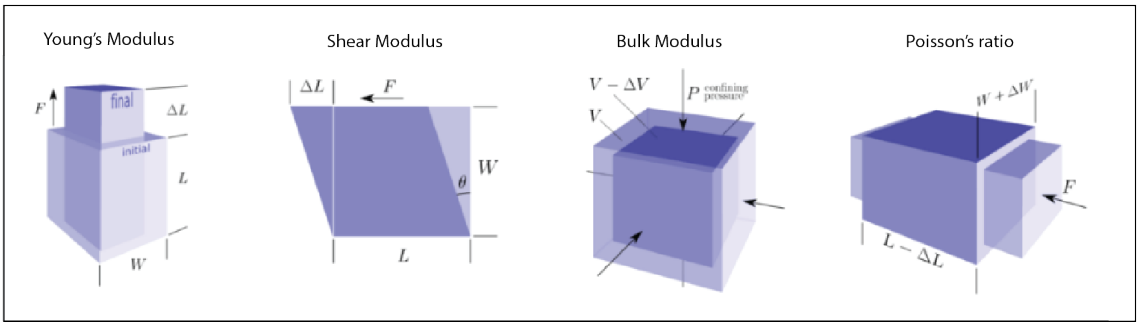

Figure 4.3: Geomechanical properties of the rock (Bianco E., 2013)

4.2.4 Depth Matching

The depth of cores often does not match the image logs' log depth due to errors introduced by the operators and equipment (Lai et al., 2018). The image log provides a continuous depth record of the cored interval. This means that the image logs can be used to accurately match the core to log depth and to identify if there are any intervals where core material may have been lost or damaged during the coring process (Goodall et al., 1998).

Due to spatial differences in measurements, problems can arise when comparing core data with electrical borehole images. Over intervals that have planar surfaces bisecting the borehole at high angles, there can be a depth offset of up to 1.8 m due to the differences in sampling diameter of the two techniques (Goodall et al., 1998).

A lithological description of the core is needed to depth shift the core to coincide with the

Gamma Ray logs. Individual sedimentary and structural features, which are distinctly seen in the core and on the image logs, are used to match the core to log depth accurately (Goodall et al., 1998; Lofts & Bristow, 1998; Major et al., 1998; Lai et al., 2018). The depth match starts with the correlation between the core and the image log, which is later correlated to the Gamma Ray log (Lofts & Bristow, 1998). It is common practice to use the Gamma Ray curve to establish a reliable reference curve of good quality. With the correct match between the image log and the core, the fractures identified on the core can be matched to the image log and oriented.

4.3 Fracture Classification

There are three types of natural fractures: extensional fractures (Mode I) and shear fractures (Mode II/III) (figure 4.4) (Fossen, 2010; Lorenz & Cooper, 2020). It thesis only focuses on Mode I and Mode II fractures. Mode I fractures form when opposing fracture walls move apart from each other in the direction normal to the fracture plane (Nelson, 2001; Davis & Kluth, 2012; Lorenz & Cooper, 2020). Mode I fractures form perpendicular to the minimum principle stress applied (Fossen, 2010), opening in the direction of the lowest principle stress (figure 4.5 (Davis & Kluth, 2012; Lorenz & Cooper, 2020)). The growth and spacing of Mode I fractures is well studied (Bai & Pollard, 2000). Mode I fractures often form perpendicular to the bedding (Bai et al., 2000), and are confined by the layer boundaries with their height equal to the layer thickness (Bai & Pollard, 2000). A Mode I fracture is called a joint when it is barren (not cemented) and a vein when filled with cement. A joint can enhance flow depending on its aperture, and a vein can create an impermeable barrier in the rock, baffling the flow. A fracture can also be partially cemented, cements may greatly reduce the local permeability of a fracture and the large scale flow connectivity of fracture systems and dissolution may greatly increase them. The partial cement can prevent a fracture from closing by sustaining the closing stress with cement bridges (Laubach et al., 2019).

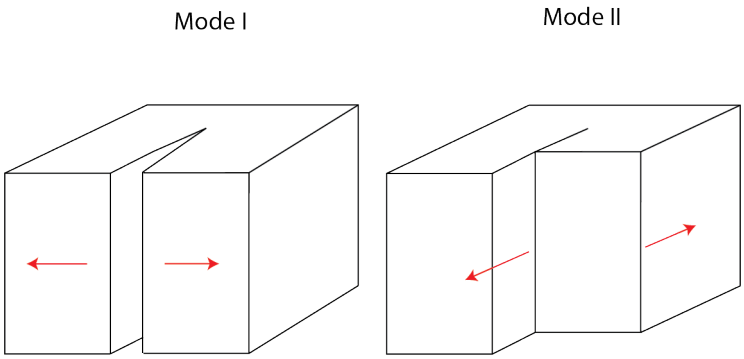

Figure 4.4: Fracture types, an extensional fracture (Mode I), shear fracture shearing parallel to fracture surface (Mode II) (modified after Fossen, 2010)

Mode II fractures form when opposing fracture walls move in opposite directions parallel to the fracture plane (Fossen, 2010; Lorenz & Cooper, 2020). They display offset and have the tendency to develop as pairs of conjugated sets. A conjugate pair consists of

two sets of shear fractures with a parallel strike but an opposite dip direction. They can be identified by an intersecting angle of 30-60°, striation on fracture plane perpendicular to the intersection point, and a compatible sense of movement with the conjugate model (Fossen, 2010). The three principle stresses can be determined in a conjugate pair (figure 4.5).

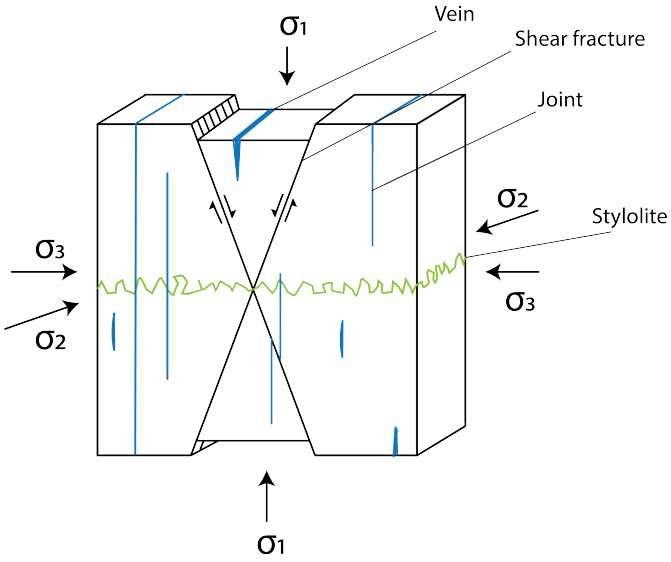

Figure 4.5: Fractures with associated principle stress directions (modified after Fossen, 2010)

There is also a third type of feature that accommodates localised contractional strain (Bruna, 2019): a stylolite. A stylolite is not a fracture, as it forms due to pressure-solution processes in high-pressure areas (Heald, 1955; Martin Baron, 2007).

This process creates an anastomosed surface consisting of rough lines displaying teeth-like peaks. These peaks are formed due to the difference in solubility of minerals (Bruna, 2019). Stylolite teeth form perpendicular to the maximal principle stress (Martin Baron, 2007). These features are sometimes called Anti-Mode I fractures (Lorenz & Cooper, 2020).

Table 4.1: Fracture characteristic per fracture type

Fracture Type	**Characteristics**	**Abbreviation**
Mode I, vein	Discontinuity, no displacement, a mineralized cement and regular width	V
Mode I, joint	Discontinuity, no displacement, no cement and regular width	J
Mode II, shear fracture	Discontinuity with displacement, striation slickenlines and an irregular width	Sh
Stylolite	Discontinuity with rough surface, a wiggly appearance, cannibalizing grains and causes separation with the matrix	St

4.4 Structural History and Related Fracturing

4.4.1 Relative Chronology

The relative chronology of the fractures forms the basis to understand the relative timing of the tectonic events. To determine the relative timing of fractures, it is necessary to examine their crossing relations. These intersections or terminations are known as abutment relations, providing information about the history and order of fracturing (Peacock, Nixon, Rotevatn, Sanderson, & Zuluaga, 2016).

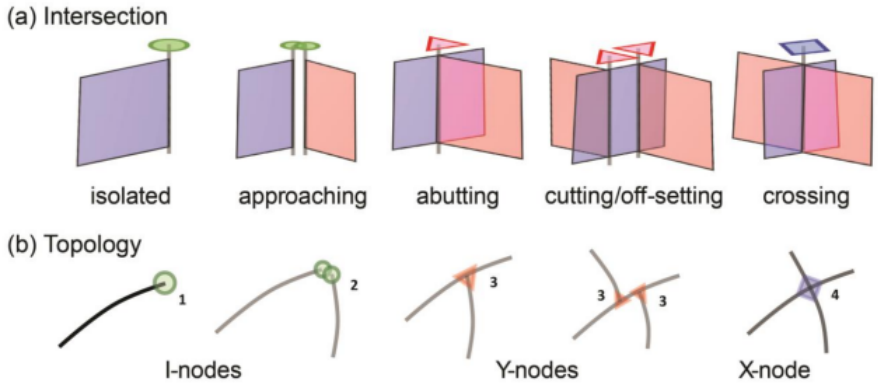

Figure 4.6: Abutment relations displaying different fracture intersections (a) and related topological terms (b). (Peacock et al., 2016)

Y or T intersections on joints indicate younger joints terminating against older joints. A Mode I fracture cannot propagate across a free surface of another Mode I fracture (Fossen, 2010; Peacock et al., 2016). However, if the first-formed joint is cemented, it no longer acts as a free surface, and a later joint can cut the older one, creating X intersections (Fossen, 2010; Peacock et al., 2016).

Y intersections on shear fractures are created when a newer fracture displaces an older fracture (Peacock et al., 2016). X intersections are synchronous when they are in a conjugated pairs configuration.

4.4.2 Stress Regimes Influencing Fracturing

Fractures form in response to stress, which can be caused by normal, reverse, or strike-slip stress regimes (Nelson, 2001; Fossen, 2010; Zoback, 2010). It is also possible that fractures form by a combined stress regime of either normal or reverse stress regimes with a strike-slip component (Zoback, 2010). The orientations which can be developed relative to the local state of stress are illustrated in figure 4.7. Fractures can be used to determine the direction of the principal stresses or loads at the time of their formation (Nelson, 2001; Zoback, 2010).

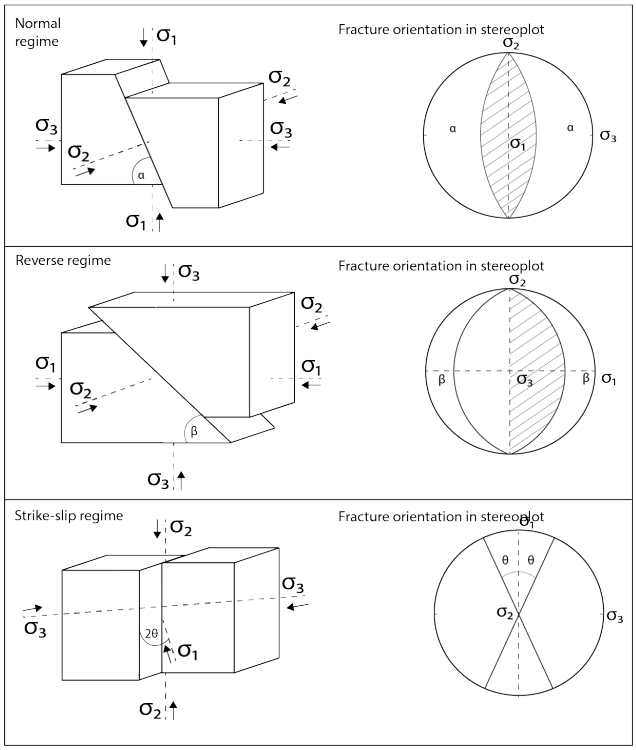

Figure 4.7: Stress regimes with associated principle stress directions and fractures (after Nelson, 2001)

The fractures need to be examined in the position in which they were formed to interpret the fracture orientations. If the bedding has tilted, the original position can be retrieved by back-tilting the fractures relative to the bedding orientation.

Another phenomenon is the occurrence of polymodal fault patterns, where three, four or more sets of fault planes have formed and slipped simultaneously (Healy et al., 2015). In figure 4.8, the fractures in accordance with the stress direction can be seen.

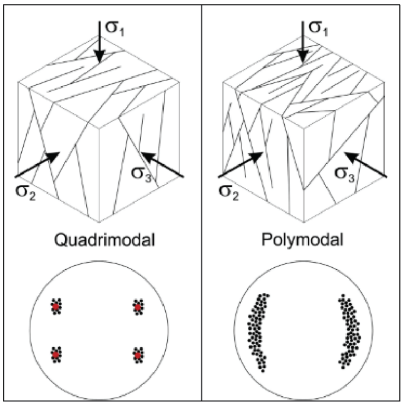

Figure 4.8: Schematic block diagrams of quadrimodal (left) and polymodal (right) faults systems according to Healy et al., 2015

4.5 Fracture Density Distribution Analysis

4.5.1 Fracture Density

Fracture density analysis describes the spread of fractures over the core and image log interval based on the spacing between the fractures and its frequency. The fracture density is the number of fractures per unit length (Makel, 2007; Lorenz & Cooper, 2020). In this thesis, the fracture density is calculated over a 1m interval.

It is important to realize that probability of encountering fractures parallel to the orientation of the well is much lower than fracture forming normal to the orientation of the well. A correction of fracture density should be applied accordingly. A correction coefficient equal to $(1/costheta)$(Tartarotti et al., 1998).

Based on the fracture density, the core or image log can be subdivided into units. This is a fracture stratigraphy (Laubach et al., 2009).

4.5.2 Fracture Distribution Analysis

Fracture stratigraphy reflects a specific loading history and mechanical stratigraphy during failure. Mechanical stratigraphy reflects the mechanical properties of rocks, including strength, elasticity, brittleness and ductility, based on the geomechanical properties. It is the by-product of depositional composition and structure, and chemical and mechanical changes superimposed on rock composition, texture, and interfaces after deposition (Laubach et al., 2009). It changes over time by alternations by amongst others due to diagenesis or burial.

To understand the fracture distribution over the core and image log over depth, it is compared to the Gamma Ray, the Density log and the geomechanical properties.

The logs are compared by looking at changes in the mean value over depth and by looking at the fluctuation in the parameters. The fluctuations are evaluated by the derivative of the parameter over an interval of 20 cm based on the minimum resolution of the wireline logs.

Chapter 5

Results

5.1 Fracture Types in the Main Buntsandstein Formation in the West Netherlands Basin

In the Detfurth and Volpriehausen Formation in the West Netherlands Basin, various geological features have been observed in the NLW-GT-01 and VAL-01 wells. This chapter focusses on the Mode I veins, Mode II fractures and stylolites which are distinctly recognized. The open fractures are discussed in chapter 5.2.

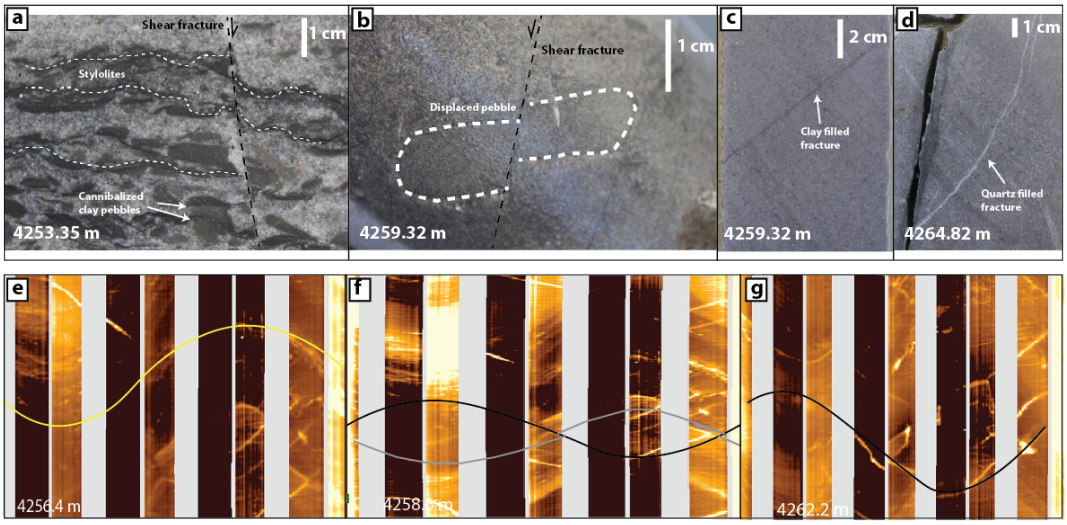

Figure 5.1: Fracture types observed in the Volpriehausen in NLW-GT-01(4254m-4267m) with the top panels (a-d) displaying the core photographs and the bottom panels (e-g) image logs. Shown are stylolites (a,e), shear fractures (b,f), Mode I fractures (c,d,g). Measured depths in the well of the examples are indicated.

Veins with either quartz or clay fill have been identified with apertures ranging from 1 mm to 2 cm. The quartz cements has been tested by hydrochloric acid and by scratching the surface. The clay filled fractures are less certain to be clay filled. The cement has not

been tested or analyzed with a thinsection. They are however likely to be filled with clay as there is an abundance of clay found in the sections of the core with clay filled fractures. In figure 5.1cd and 5.2b, examples of the veins can be seen in the NLW-GT-01 and VAL-01 well, respectively.

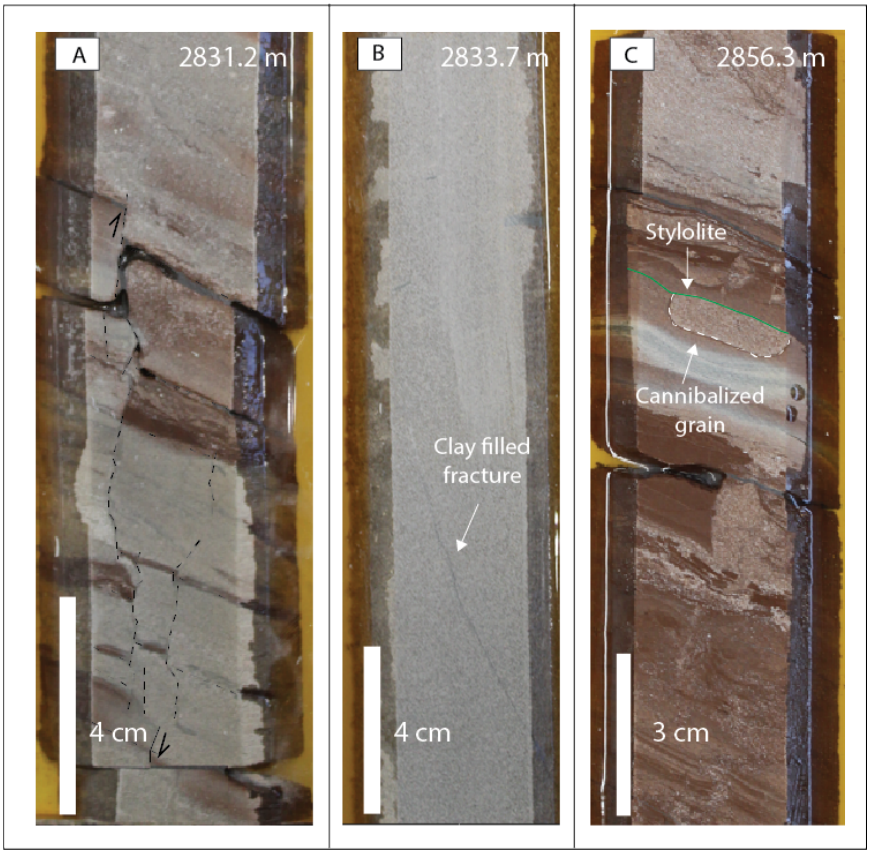

Figure 5.2: Fracture types observed in the Lower Triassic formation from the Volpriehausen in VAL-01(2829-2857m) displaying the core photographs of shear fractures (a), Mode I fractures (b), and stylolites (c). Measured depths in the well of the examples are indicated.

Shear fractures are identified on the core by the visible offset they create on the bedding or on individual coarse grains or pebbles. In figure 5.1b and 5.2a, two examples of these shear fractures are shown from the NLW-GT-01 and VAL-01 well, with offsets ranging from 1 mm to 15 cm. These fractures have rough fracture planes and are concentrated in the coarse-grained sections of the core.

Stylolites are characterized by the process of dissolution of grains, where they grow around insoluble grains (figure 5.1a and 5.2c). Stylolites are commonly found in coarse-grained core sections or around clay pebbles.

On both the image logs, the shear on most of the fractures is not observed. On the AST no difference in amplitude response have been seen fro the different fracture typesl The

stylolites have also not been seen on the AST, as they are probably below the resolution of the data. On the FMI. The clay cemented fractures show a medium resistive response and the quartz cemented as low resistive (figure 5.10).

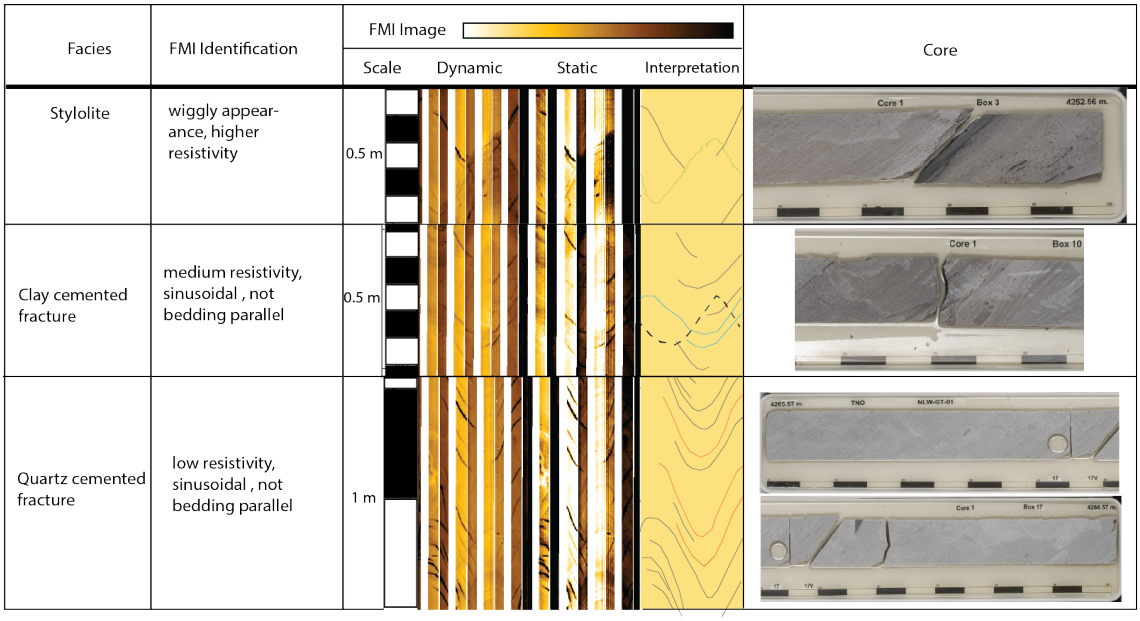

Figure 5.3: FMI and fracture facies characteristics in NLW-GT-01

The stylolites appear as light-coloured low resistive features with a wiggly cobweb appearance on the FMI, distinctly lighter than the matrix resistivity. They are often not interpreted on the FMI as they are below the data resolution.

Summary In NLW-GT-01, a total of 34 natural fractures and 40 open fractures is identified over a 30 m length slab. In VAL-01, a total of 87 natural fracture and 70 open fractures is identified over a 60 m length slab.

Table 5.1, an overview of each fracture type observed in the NLW-GT-01 and VAL-01 well can be seen along with their confidence levels. In Appendix XXX and XXX the complete data set of all the identified fractures and their properties can be found.

Table 5.1: Identified fractures on the slab of NLW-GT-01 and VAL-01

Fracture Type	**Confidence**	**Number of fractures in NLW-GT-01**	**Number of fractures in VAL-01**
Mode I, veins	High	19	45
Mode II, shear fractures	High	7	32
Stylolites	High	8	10
Open fractures	Low	49	70
Total		**83**	**157**

5.2 Joints and Drilling-Induced Fractures on the Core and Image Log

The fractures in the well, NLW-GT-01, have been thoroughly researched by several studies. In 2018, after acquiring the resistivity image log (FMI) and the dipole sonic, Schlumberger performed a fractures analysis. They interpreted over 300 natural fractures over the interval between 4250 m to 4380 m, parallel to the known present-day maximum horizontal stress (NW-SE) (Kourta & Jocker, 2018). At the same time, Panterra realized a detailed core analysis, with a lithological description indicating only five sections with fractures. They assessed the fracture analysis from Schlumberger and concluded that most interpreted fractures are thin clay layers (Vinci, 2018). The Main Buntsandstein Subgroup was further researched by Boersma et al. (2021), who interpreted 58 natural fractures over the logged interval, which is 6.7% of all the interpretable discontinuities on the image logs. They picked the fractures based on the continuity of the sinusoidal response of the fractures on the image logs. They concluded that the image log shows more features than the core data over the same interval.

A clear discrepancy in fracture characterisation can be seen between the three studies. This chapter re-evaluates the classification of drilling-induced fractures in the NLW-GT-01 and VAL-01 wells.

5.2.1 Induced Fractures

Induced fractures are fractures created in response to stress changes associated with drilling, coring, handling, and processing procedures (Lorenz & Cooper, 2017; Lai et al., 2018; Chatterjee & Mukherjee, 2023). Most cores and boreholes contain induced fractures of several types and various forms. It is essential to identify induced fractures and not confuse them with natural fractures. However, the distinctions between natural and induced fractures are not always obvious (Lorenz & Cooper, 2017), which could lead to an over or underestimation of the number of natural fractures.

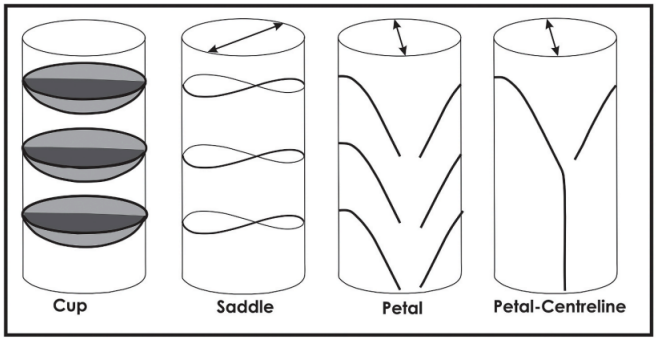

Figure 5.4: Schematic overview of drilling-induced fractures in cores (Chatterjee, 2023)

Induced fractures in the core are commonly characterized by rough, unmineralized, fresh breaks; lips at the core edge (figure 5.5); plumes that interact with the core edge and that

follow a core axis; and fracture planes that are consistently normal or parallel to the core axis (Lorenz & Cooper, 2017).

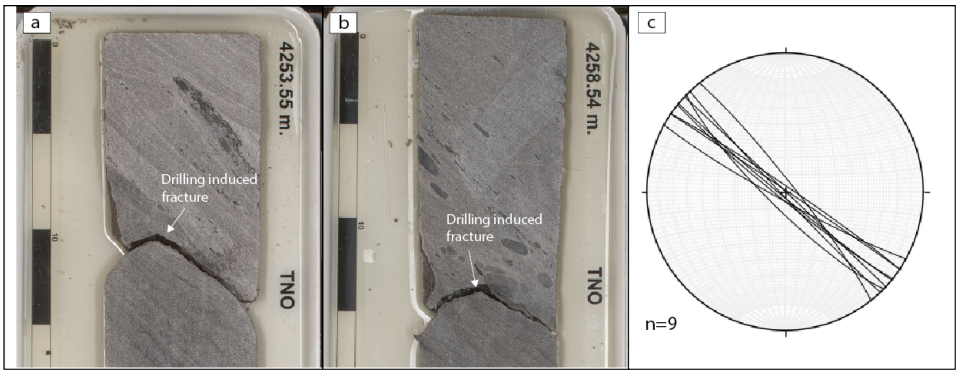

Figure 5.5: Two examples of petal fractures in NLW-GT-01 (a,b) and their orientations on a stereoplot (c)

Most induced fractures on the core form due to the weight of the drill bit on the formation or due to vertical relaxation of the stresses on the core (Lorenz & Cooper, 2017; Chatterjee & Mukherjee, 2023), such as bedding parallel fractures, petal fractures, saddle fractures, disc fractures, cup fractures or centerline fractures (figure 5.4). Over the core and image log of NLW-GT-01, nine of these petal fractures have been identified and oriented (figure 5.5). They are recognized by the angle in the fracture plane.

Another type of induced feature is a desiccation fracture. These are very thin cracks (less than 1 mm) that are created primarily on mud-rich intervals. The mud dries and shrinks, inducing small-scale cracks (Chatterjee & Mukherjee, 2023) (figure 5.6). On the core, countless of these very thin cracks at different orientations have been found. They are all located in the claystone sections of the core or inside clay pebbles.

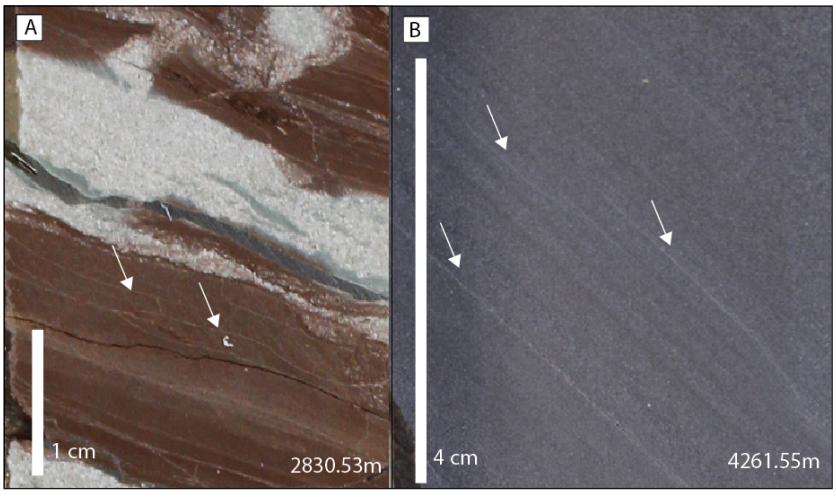

Figure 5.6: Desiccation fractures in VAL-01 (A) and NLW-GT-01 (B) indicated with the white arrows

Image logs can recognize drilling-induced fractures on the borehole wall as conductive fractures in resistivity logs and as poor reflectors of acoustic energy in acoustic logs due to the aperture of the fracture. They are extensively developed with constant orientation and typically show an en-echelon pattern as petal fractures (figure 5.7)(Haller & Porturas, 1998; Lai et al., 2018; Chatterjee & Mukherjee, 2023).

Another type of drilling-induced failure is the failure of the borehole wall. The borehole cross-section tends to become elliptical due to the regional stress field. Borehole wall failure may occur along the long axis of the ellipse and produces features termed "breakouts" (figure 5.7). Borehole breakouts can be recognized as reciprocal 180 degrees conductive or low amplitude stripes in image logs due to the accumulation of drilling mud. Breakouts are more common in less competent lithologies and indicate the horizontal present-day stress orientation (Price and Cosgrove, 1994).

Induced fracture are important as they are an indicator of the direction of present-day stress field. Based on the orientation of the drilling-induced fractures on the core, the minimum horizontal stress can be interpreted by their strike (Lorenz & Cooper, 2017; Lai et al., 2018; Chatterjee & Mukherjee, 2023).

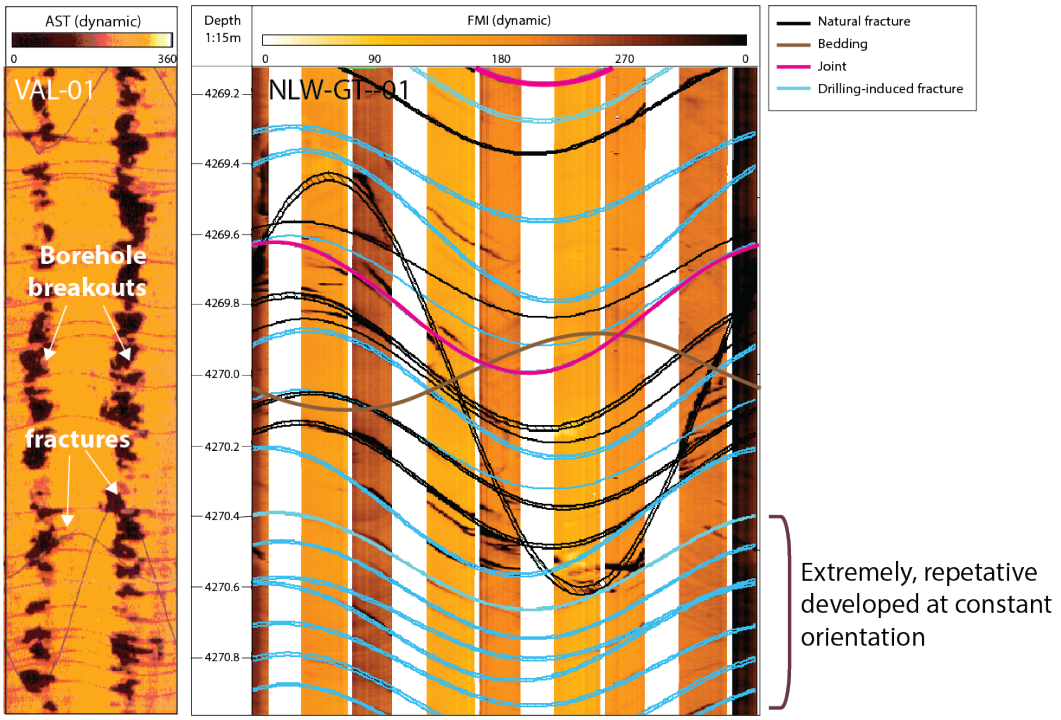

Figure 5.7: Borehole breakouts in VAL-01 (AST) and drilling induced fractures in NLW-GT-01(FMI). The natural fractures (black), drilling-induced (blue) and bedding (green) are indicated.

The drilling induced fractures in NLW-GT-01 are striking NW-SE perpendicular to the minimum horizontal stress direction. On the AST in VAL-01, these fractures are not ob-

served. The NE-SW oriented breakouts in VAL-01, imply a NW-SE maximum horizontal in-situ stress direction. In NLW-GT-01, there are no breakouts identified on the image log. The in-situ stress orientation from both NLW-GT-01 and VAL-01 coincides with the stress directions found in the literature (Chapter 2.1)

5.2.2 Classification of Fractures

The majority of the open fractures on the core of NLW-GT-01 and VAL-01 are hard to classify. They are planar, not bedding parallel, with smooth or rough fracture planes and open. The question is whether they are natural joints or drilling-induced fractures. They are classified based on their orientation, as they cannot be distinguished based on their appearance. The same holds for the fractures identified on the image logs. This chapter explains the classification criteria for the fractures on the core and the image logs. In figure 5.8, a flow chart of the process is depicted. The fracture classification on the image log build on the classification of the core. The uncertainty in the classification can be tested back comparing the initial fracture classification on the core with the interpretation on the image log.

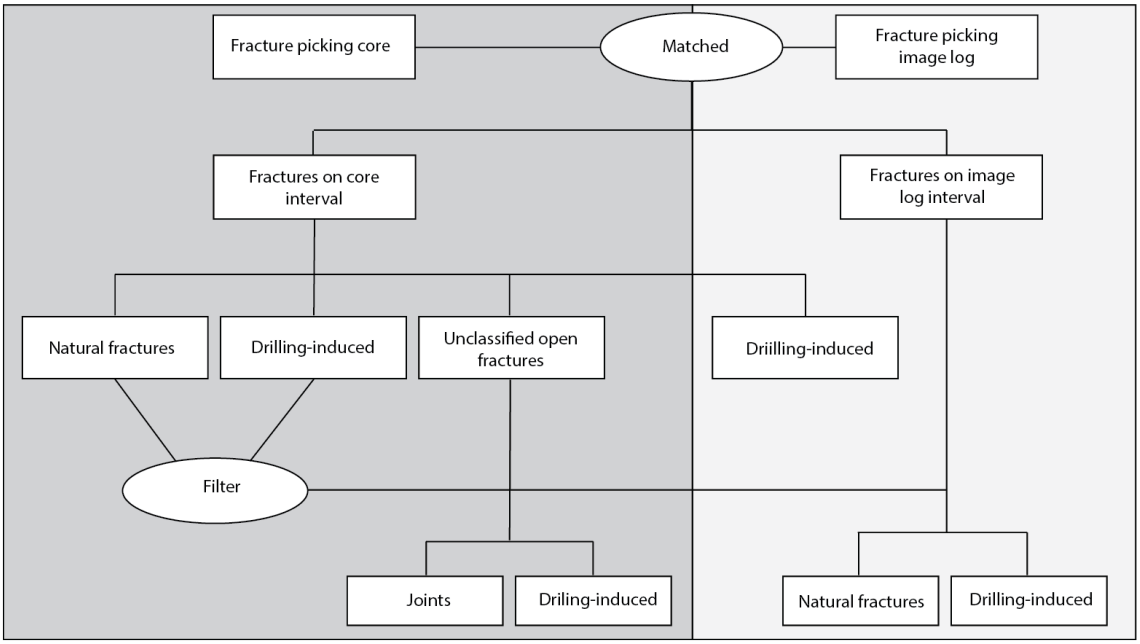

Figure 5.8: Flowchart for the classification of fractures based on their orientation on the core and image log

Classification of Fractures on Core

In Naaldwijk (NLW-GT-01), nine petal fractures have been found and oriented. They form the basis of the orientation of the drilling-induced fractures. They have a dip angle higher than 80° and a strike between 118° and 137°(figure 5.5 and 5.9). The natural fracture have almost the same orientation as the drilling-induced fractures. However, by comparing the drilling-induced fractures and the natural fractures, a distinct difference in dip angle can

be seen. The natural fractures have dip angles between 50-90° while the drilling-induced fractures are limited to a range of 80-90° and the drilling-induced fractures have strikes ranging from 118-137° and the natural fractures from 105-158° (figure 5.9). A conservative method is chosen for the interpretation of the joints based on these orientations.

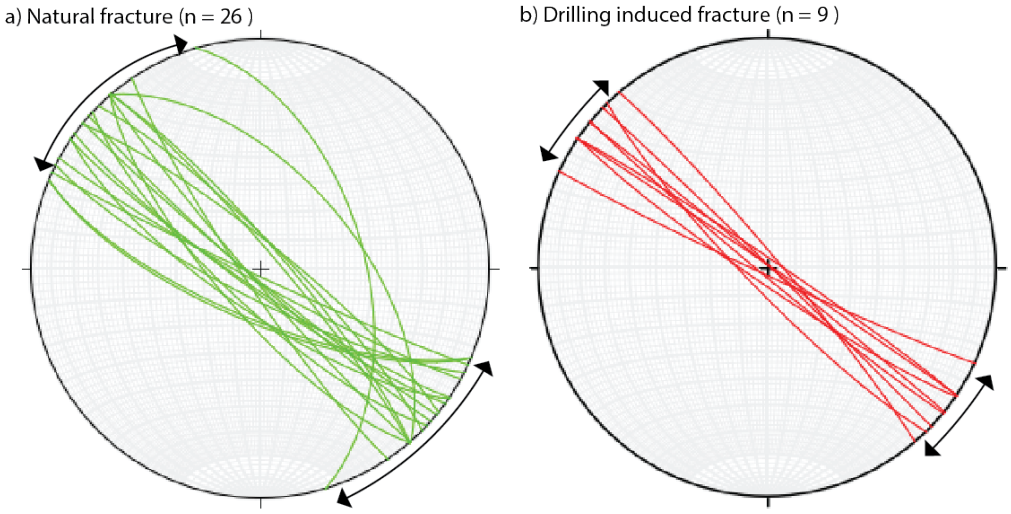

Figure 5.9: Stereoplot of the natural (a) and drilling-induced fractures (b) of NLW-GT-01

The open fractures are classified as drilling-induced fractures when they are in the range of the orientations of the drilling-induced fractures. The fractures with a dip angle higher than 80° and a strike between 118° and 137° are medium-confidence drilling-induced. The fractures with dip angles lower than 80°, are medium-confidence joints, and fractures with dip direction lower than 80° and higher than 127° are low-confidence joints (table 5.2).

Table 5.2: An overview of the characteristics of the drilling-induced fractures and joints and their confidence levels

Fracture type	**Characteristics**	**Abbreviation**	**Confidence**
Drilling-induced fractures	Irregular, centerline, desiccation fracture, petal fracture, non-planar	I	High
Drilling-induced fractures	Open, barren discontinuities with no displacement and a orientation with dip angles in the range of 80-90° and dip direction between 118° and 137° and a smooth fracture plane	I	Medium
Joint	Open, barren discontinuities with no displacement and an orientation with dip angles lower than 80° with a rough fracture plane	J	Medium
Joint	Open, barren discontinuities with no displacement and an orientation with dip direction lower than 118° and higher than 137° with a rough fracture plane	J	Low

5.2.3 Classification of Fractures on Image log

On the image log of NLW-GT-01 and VAL-01 all the interpretable discontinuities have been manually picked. Over the image log in NLW-GT-01, 749 discontinuities have been identified, and 1126 bedding orientations over the Detfurth and Volpriehausen Formation. On the image log of VAL-01, 58 discontinuities and 162 bedding planes have been picked. The fractures on the image log are matched to the fractures found on the core.

On the image log of NLW-GT-01, the sandstone, claystone and clay pebbles could be identified by differences in FMI response (figure 5.10). Based on several high confidence anchor points as clay pebbles and sharp sandstone-claystone transitions, a depth shift of 3 m is identified. Based on the individual fractures and bedding planes on the core compared to the image log and the gamma ray responses compared to the claystone intervals.

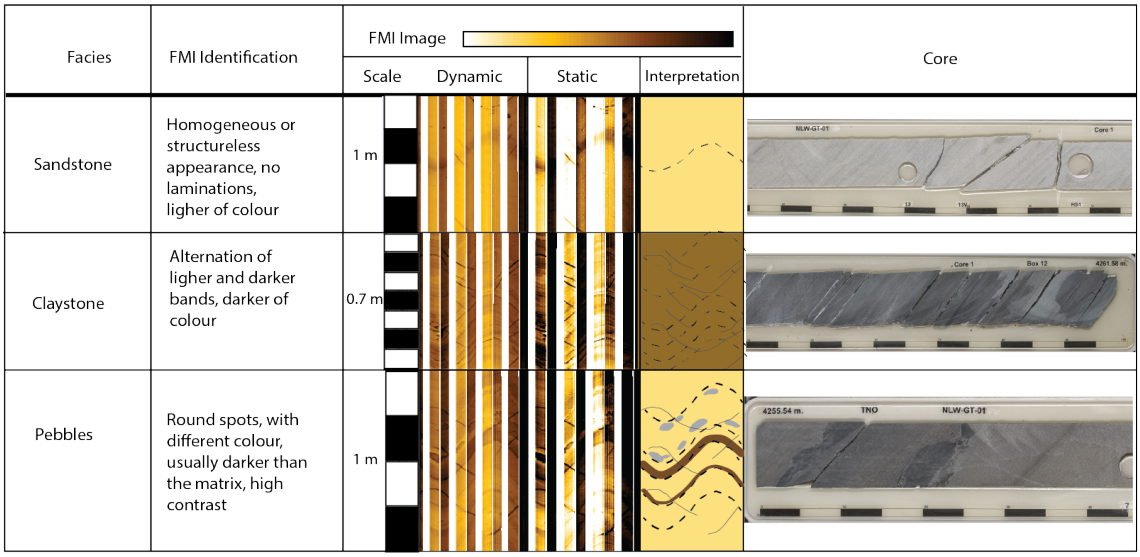

Figure 5.10: FMI and core facies characteristics in NLW-GT-01

In VAL-01, the different facies are not characterised by a distinct change in AST response. The depth shift here is based on the sharp boundary transition between sandstones and claystone bedding, which is identified as a higher impedance boundary. Here a 6.2 m depth shift is seen.

Over the core interval of NLW-GT-01, 34 natural fractures, 49 open fracture and 9 drilling-induced are identified and matched. However, in the image log over the core interval, there are 99 additional discontinuities recognisable, which are not found on the core. All the fractures which are not observed in the core have to be drilling-induced fractures. This means that at least 68% of the fractures found in the image log over the core interval are drilling induced in NLW-GT-01.

The natural fractures cannot be distinguished from the drilling-induced fractures based on their resistivity response. The cemented fractures on the core, seem to have a slightly

lighter response. However the drilling induced fractures can have both a lighter and a darker response (figure **??**). Therefor the fractures are classified based on their orientation only on the image log.

On the image log of VAL-01, 30 discontinuities have have been identified. 24 are matched to natural fractures and 6 drilling-induced fractures over the core interval. No additional discontinuities have been observed in the image log of VAL-01.

Knowing that 68% of the fracture over the core interval on the image log of NLW-GT-01 is drilling induced and 20% on VAL-01, it is expected that part of the fractures outside the core interval are also drilling-induced. To classify the fractures outside the core interval a classification based on the orientation of the drilling-induced fractures found on the core is proposed to get a representative fracture density of natural fractures outside the core interval on the image log. The objective is to balance filtering out the drilling-induced fractures and keeping the natural fractures. After filtering 227 natural fractures are identified over the image log in NLW-GT-01 and 50 in VAL-01

Uncertainty in the Fracture Classification Based on Orientation

The uncertainty in this classification, is assessed by looking at the original interpretation of the fractures on the core with the classification based on their orientation. For simplicity only the full range of the orientations is taken and the subdivision into medium and low confidence joints is not taken into account.

Initially over the core interval in NLW-GT-01, 51 natural fractures and 9 drilling induced fractures had been seen on the core and 99 drilling induced fractures were observed in the image log (159 total). By applying the classification based on the orientation of the fractures. 42% of the natural fractures have been misinterpreted as drilling induced and 20% (21x) of the drilling-induced fractures have been misinterpreted as natural fractures. This results in a 13% (21/159) chance of a fracture being misinterpreted as natural. The classification is under-counting the natural fractures, giving a conservative estimation of the fracture density.

When applying the classification on VAL-01, only one fracture is classified as drilling-induced, while there are 6 drilling induced fractures observed on the core and 24 natural fractures. This results in a 16% (5/30) chance of a fracture being misinterpreted as natural

The impact of the classification on the core-classified drilling-induced fracture and natural fractures is tested by analysing the impact of the selected orientation ranges. This is tested by applying a classification based on the extreme values of a normal distribution fitted to the orientations of the high-confidence drilling-induced fractures.

This gives a filter that filters dip angles lower than 77° and strikes lower than 113° and higher than 145°. These orientations are based on the lowest probability values from the normal distribution fitted on the drilling-induced dip angles and strikes (figure 5.11).

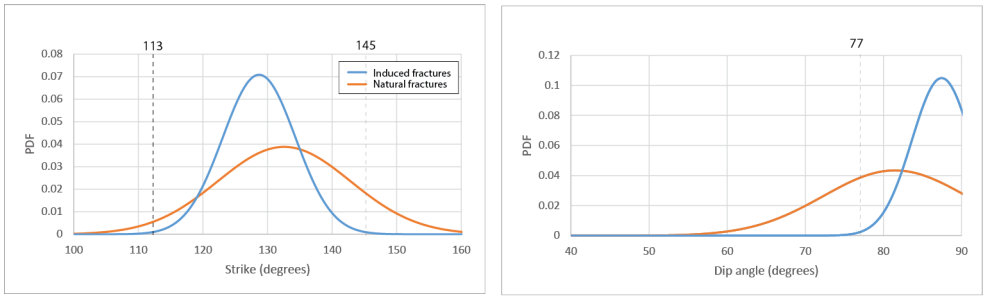

Figure 5.11: Normal distribution on backtilted fracture orientations of the core in NLW-GT-01 based on the high confidence drilling-induced fractures

In figure 5.12, the first column represents the initial data set where the filter has not been applied. There are 50 natural fractures, 99 drilling-induced fractures, and 749 resistive fractures outside the core interval. The second column gives the filtered fractures based on the fracture classification defined in Table 5.2. The number of fractures is reduced to 30 natural fractures, 21 drilling-induced fractures, and 227 resistive fractures outside the core interval. The third column represents the filtered fractures with the extreme filter. Here there are 20 natural fractures, 9 drilling-induced fractures, and 148 resistive fractures outside the core interval remaining. Looking at the three interpretations, it can be seen that the depth sections with high fracture densities remain the same.

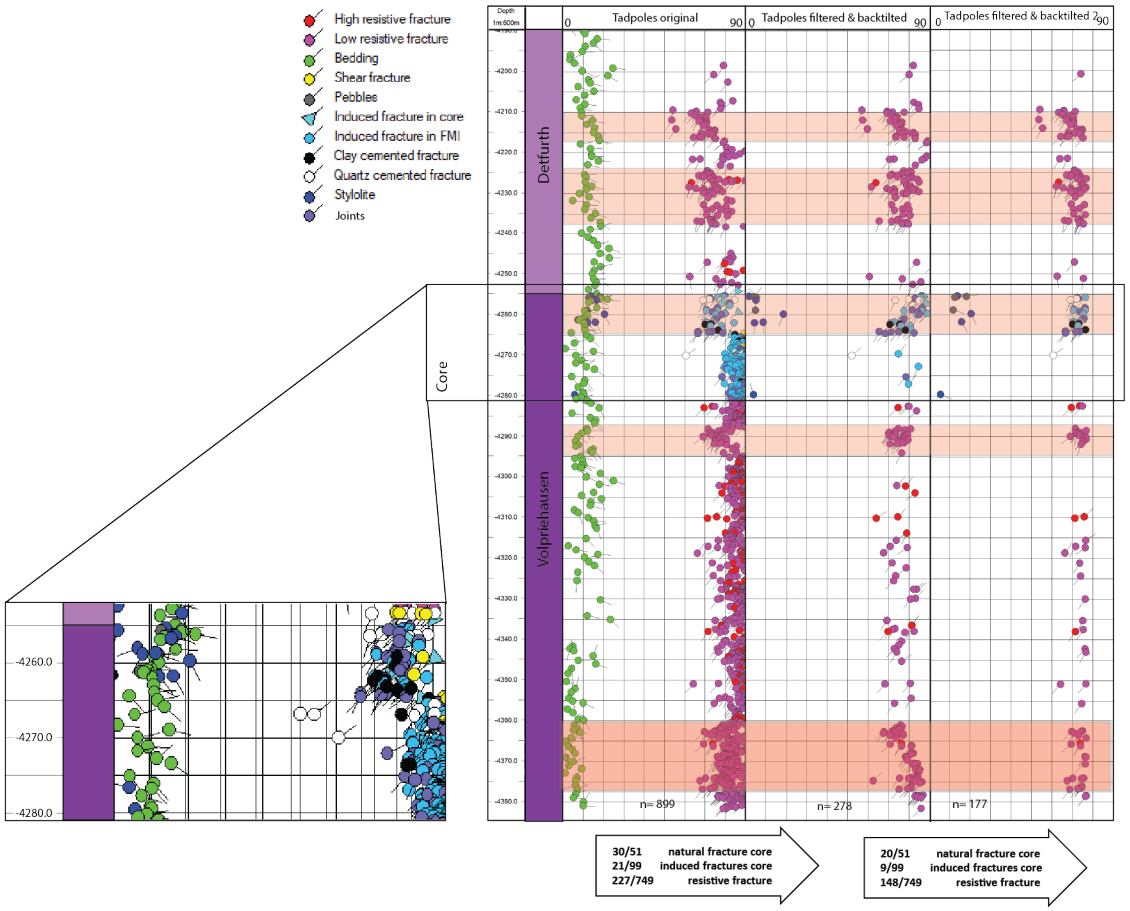

Figure 5.12: An overview of the different fracture densities identified on the FMI in NLW-GT-01, with the initial identification of the fractures (left), the fracture densities after applying the filter (middle) and after applying the extreme filter (right), in red highlighted the high fracture densities

5.2.4 Fractures Below the Resolution of the Image Logs

By comparing the fractures identified on the core and image logs, differences in fracture density have been observed. In NLW-GT-01, the initial interpreted fracture density is dominated by drilling-induced fractures. In VAL-01, the opposite can be seen. 84% of the natural fracture on the core is below the resolution of the AST. The FMI has a resolution of 5 mm, while the AST has an even lower resolution of 1 cm. Fractures with apertures smaller than this or with a low contrast with the formation will not be detected by the image logs.

By comparing the fracture density observed in the core with the image log, the impact of the resolution is assessed. It can be seen that the depth intervals with high fracture densities remain the same. When considering an appropriate fracture density for the VAL-01 well, a factor of 2.8 compared to the fracture density of the image log is expected.

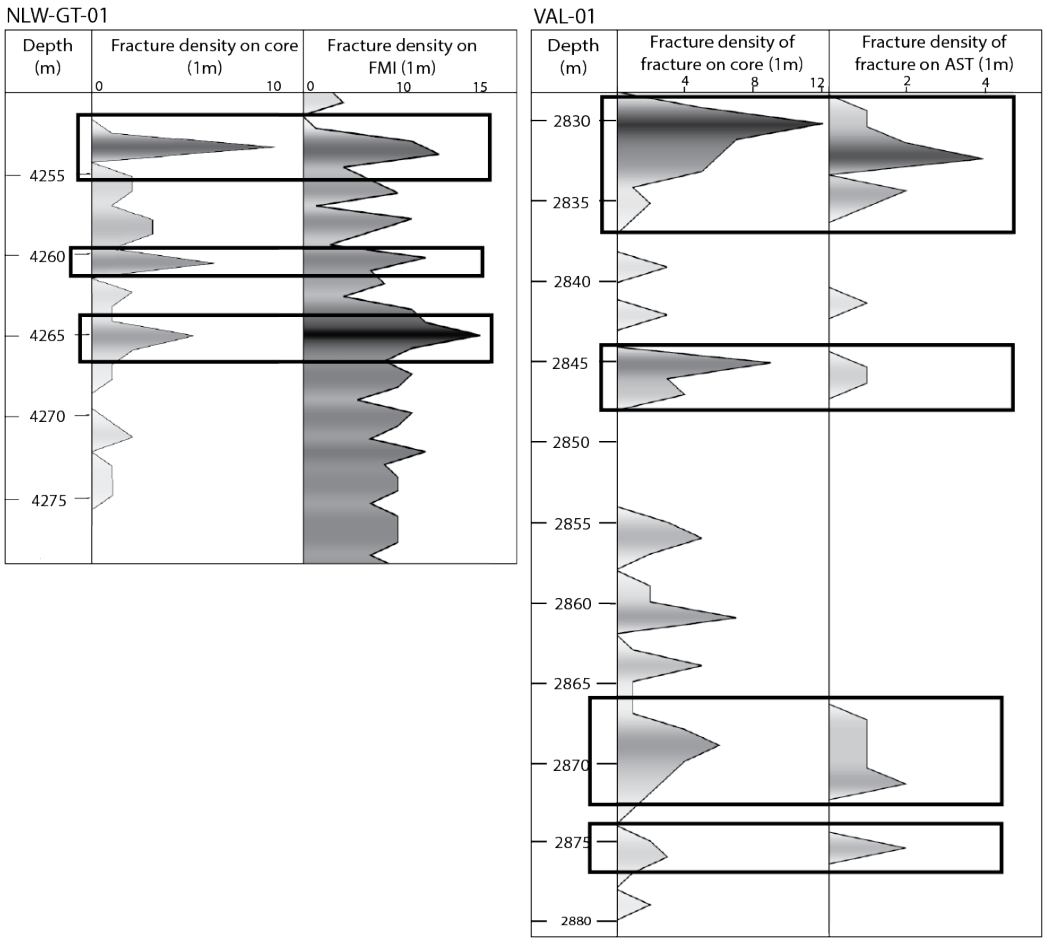

Figure 5.13: Overview of fracture density over the core comparing the resolution of the core and image log in NLW-GT-01 and VAL-01. The black box indicates the high fracture densities

5.2.5 Summary

- The drilling induced fractures in NLW-GT-01 are striking NW-SE perpendicular to the minimum horizontal stress direction. The NE-SW oriented breakouts in VAL-01, imply a NW-SE maximum horizontal in-situ stress direction.

- Fractures are classified based on their orientation on the image logs. The classification is based on the orientation of the drilling induced fractures on the core. This introduces an uncertainty of 13% in NLW-GT-01 and 16% in VAL-01 in the natural fracture to be drilling-induced.

- The high fracture density depth ranges are not effected by increasing the range of fracture orientations for the classification of natural fractures.

- The resolution of the data impacts the number of identified discontinuities, in VAL-01 84% fracture are below the resolution of the data.

5.3 Structural history and related fracturing in the Triassic sandstones on NLW-GT-01 and VAL-01

5.3.1 Relative chronology and fracture attitude analysis of NLW-GT-01

Core analysis

The history of the fractures found on the core of NLW-GT-01 is assessed by interpreting the abutment relations seen on the core. On the core, there are two intervals where the relative movements of the fractures can be seen (figure 5.14 and 5.16).

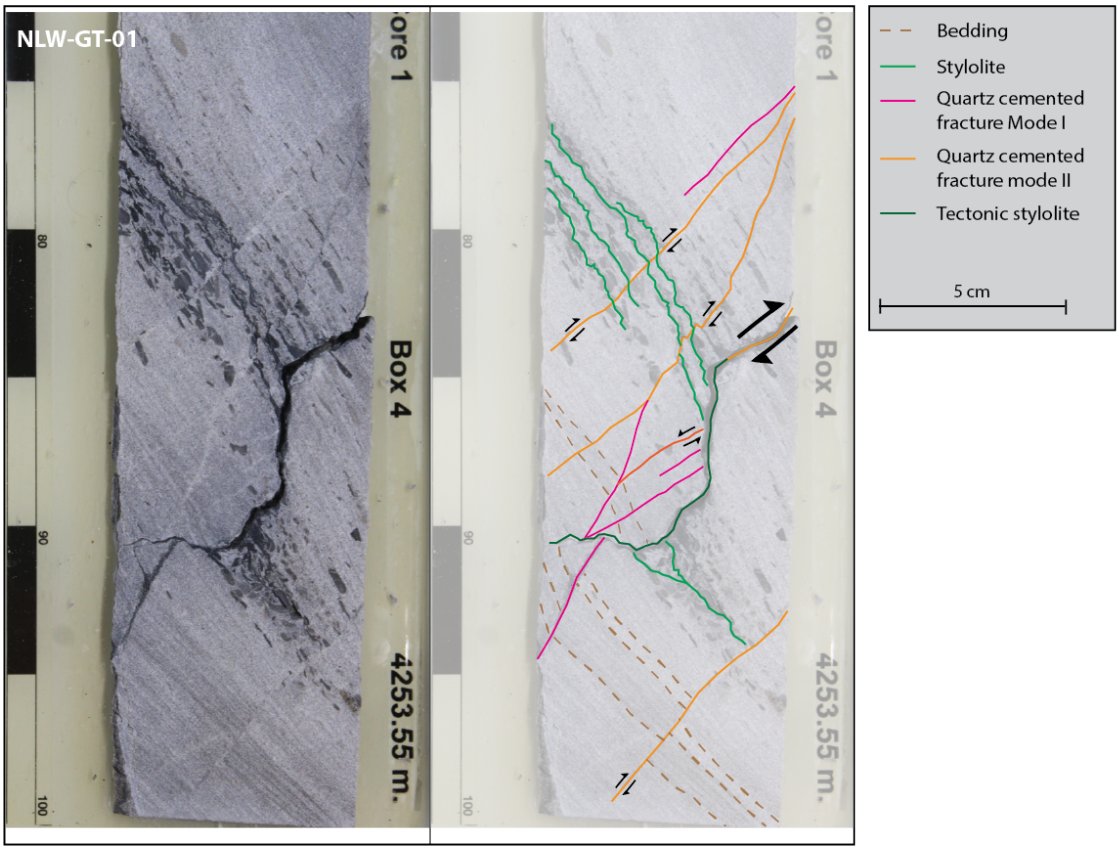

Figure 5.14: Relative chronology assessment by abutment relations on the core of NLW-GT-01 (4253.55m), showing bedding (dashed brown), a bedding parallel stylolite (light green), Mode I quartz veins (pink), Mode II shear fractures (orange), and a tectonic stylolite (dark green). Movements of the shear fractures are indicated with displacement arrows.

On the interval at a depth of 4253.55 m (figure 5.14), five types of features are seen. The dark grey features are bedding parallel stylolites. In the vicinity of this structure clay pebbled appear to be dissolved. On this section of the core, nine quartz filled fractures are found, which are either Mode I or Mode II fractures. The quartz cement was tested with hydrochloric acid. They show an offset of 0.5 mm to 8 cm. Four out of five shear fractures display dextral movement and one sinistral movement. A stylolite is formed at an angle

compared to the bedding. This is a tectonic stylolite (Heald, 1955; Martin Baron, 2007; Bruna, 2019). The irregular shape of the plane is assessed over the core in combination with the slab, figure 5.15. The plane is very angular and irregular and is not likely to be created by slip on a fracture plane. However, the bottom part of the stylolite plane is more planar and smooth. It can be seen that the bedding parallel stylolite has been displaced over 10 cm. This displacement could not have been created by the dissolution of the stylolite only. It could be that before the tectonic stylolite was created, the bedding parallel stylolite was displaced by a shear fracture. The tectonic stylolite could have been created at the location of the shear fracture, as it might have been open allowing flow and dissolution creating a preferential location for the stylolite to form. The displacement of the bedding can be partly created by the shear of the fracture and partly by the cannibalistic behaviour of a stylolite.

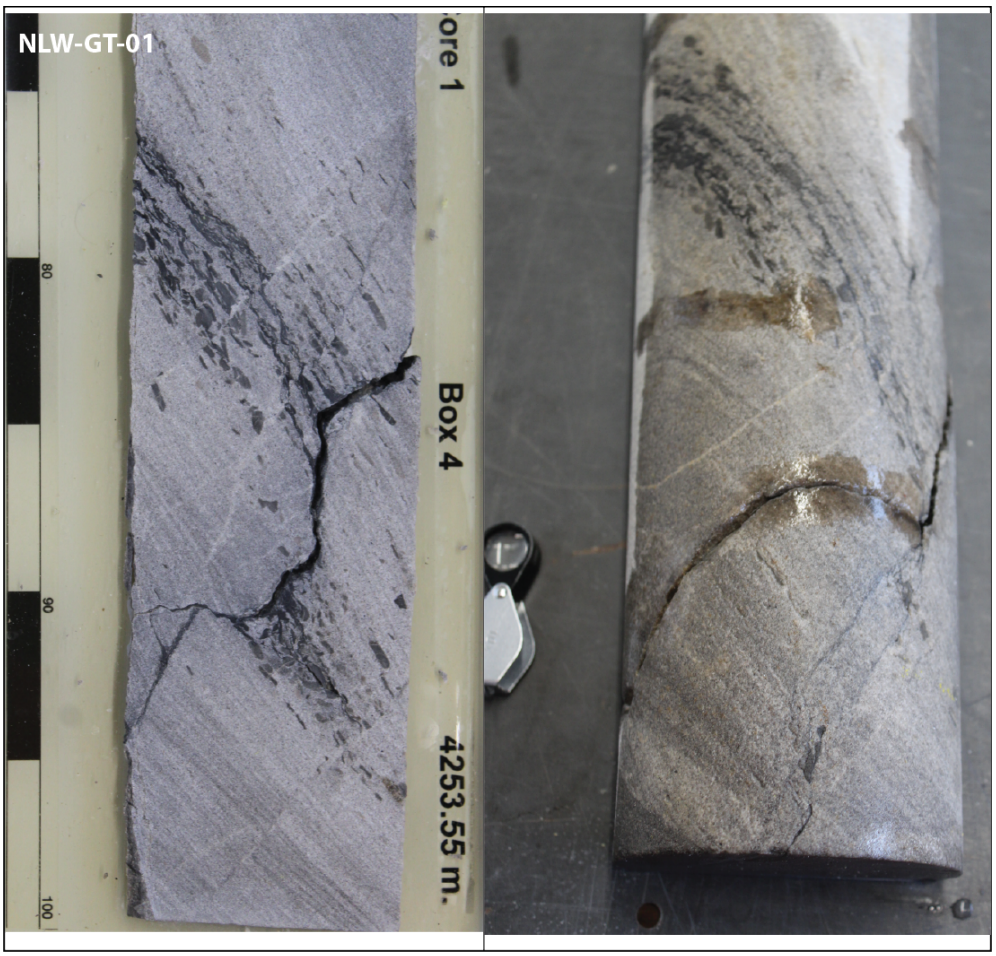

Figure 5.15: Stylolite on the core (right) and slab (left) of NLW-GT-01 (4253.33m).

The first structural feature that is formed in this section of the core is the bedding parallel stylolite. They are formed prior to the shear fractures as it can be seen that these fractures shear the stylolite. The timing of the quartz cemented mode I fractures relative to the shear fractures and the bedding parallel stylolite can not be determined. The tectonic

stylolite formed last as it overprints one of the shear fractures and two of the quartz cemented mode I fractures and one shear fracture terminate against the stylolite.

In figure 5.16 another section of the core is seen. Two other quartz cemented fractures can be seen with an aperture between 0.5 to 1.5 cm. On the slab, the movement of the fractures could not be determined. The broken pieces of the core on the polymer slab give a very uncertain interpretation. One clay filled fracture is seen, which terminates against the quartz cemented fracture indicating that it formed after the quartz cemented fracture.

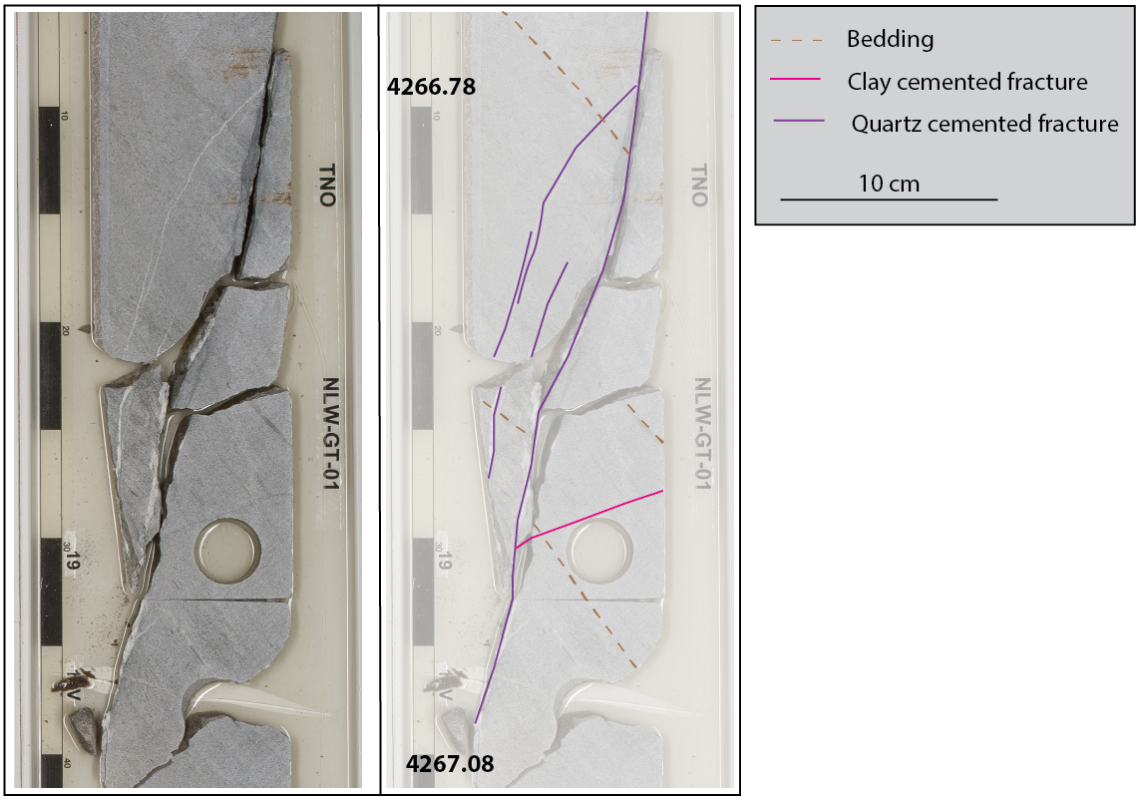

Figure 5.16: Relative chronology assessment by abutment relations on the core of NLW-GT-01 (4266.78), showing bedding (dashed brown), Mode I quartz veins (purple) and a clay filled Mode I fracture (blue).

Associated Stress Regimes

The stress regimes in which the fractures are formed can be interpreted by combining the relative chronology of the fractures with their back-tilted orientations (figure 5.17). All the fractures orientation found over the 30m core are taken into account.

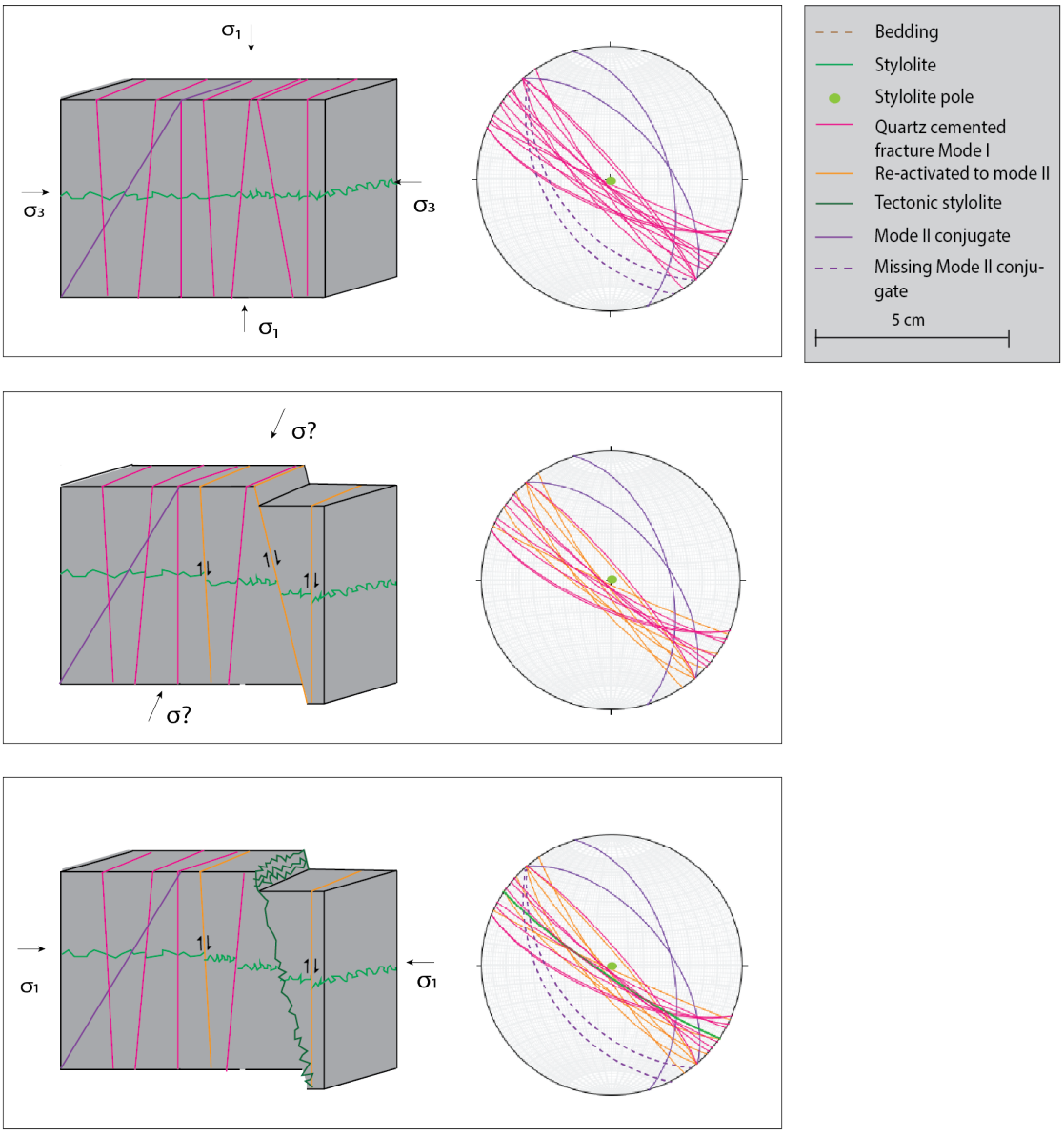

Figure 5.17: Three phases of fracturing on schematic block diagrams with stereoplot of all the backtilted fractures over the core of NLW-GT-01.

The bedding parallel stylolites are the first discontinuities that are created. These are created by a vertical maximum stress orientation. The quartz-cemented Mode I fractures are formed striking NNW-SSE at a 90° angle to the bedding parallel stylolites (figure

5.14) . These could be formed under the same vertical maximum stress. Additionally they indicate a horizontal minimum stress in the NE-SW orientation. The quartz cemented fractures from 5.16, which are also NNW-SSE oriented, could be one side of a conjugate set, where the shearing component of the fracture on the slab could have been missed. The other side of the conjugate set is expected to be oriented NNW-SSE dipping in the opposite direction, parallel to the borehole orientation of 075/040. These fractures are not seen on the core. These three features (figure 5.14), fit the combination of fractures for a normal regime according to Chapter 4.3.

The second phase is characterised by the shear fractures at 90° angle to the bedding. These fractures are with 90° angle to the bedding are 30° higher than the angle of the expected conjugate fractures in the previously mentioned normal regime.

The last phase is the regime in which a tectonic stylolite forms NNW-SSE oriented at a 90°angle to the bedding. The stylolite is formed at 90° to the maximum stress direction. This would indicate a maximum horizontal stress and thus a reverse system.

Image log analysis

By comparing the fracture orientation over the core interval and the full image log interval (figure 5.18). It can be seen that the bedding parallel stylolites are only picked on the core interval where the exact location of the stylolite was known or could be indirectly identified by the clay pebbles. Outside the core interval there have not been any other clay pebbles observed.

The orientations of the core are found over the image logs interval. Additionally, the NNW-SSE oriented fractures dipping south could form the counterpart of the conjugate pair fitting the expected orientation of approximately NNW-SSE oriented 60° south and a set of vertical fractures oriented WNW-ESE can be seen. This orientation is not observed in the core. They could have been formed as part of a polymodal set.

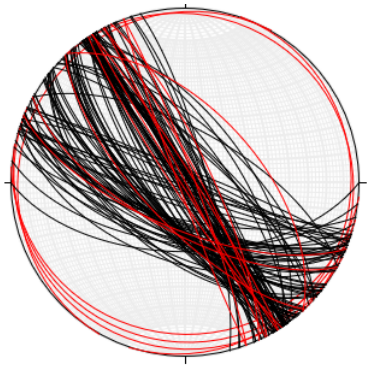

Figure 5.18: Stereoplot of all the fractures of the image log interpretation from NLW-GT-01, fractures in red on the core interval and fracture on the FMI in black.

5.3.2 Fracture attitude analysis of VAL-01

Core and Image log analysis

On the core of VAL-01, there is no section where the relative timing of the fractures and the fracture orientation could be interpreted together. The fracture attitude is therefor analysed on its own. However it is crucial to incorporate the fact one out of four fractures on the core is a mode II fracture (figure 5.19).

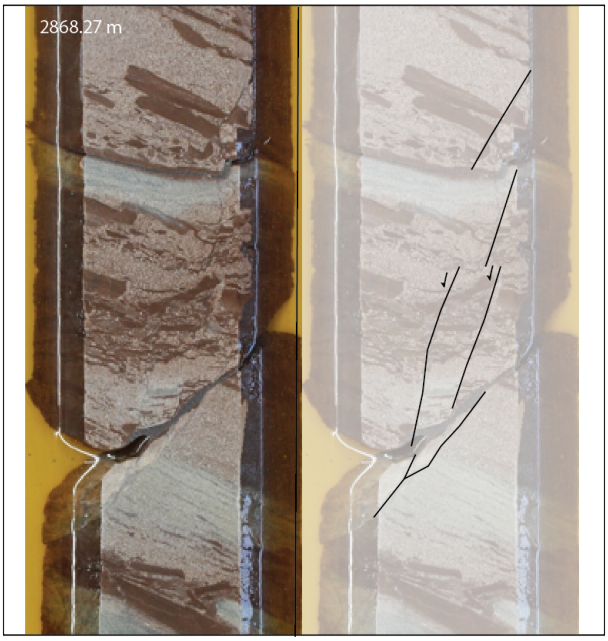

Figure 5.19: Example of Mode II fractures in VAL-01 (2868.27 m)

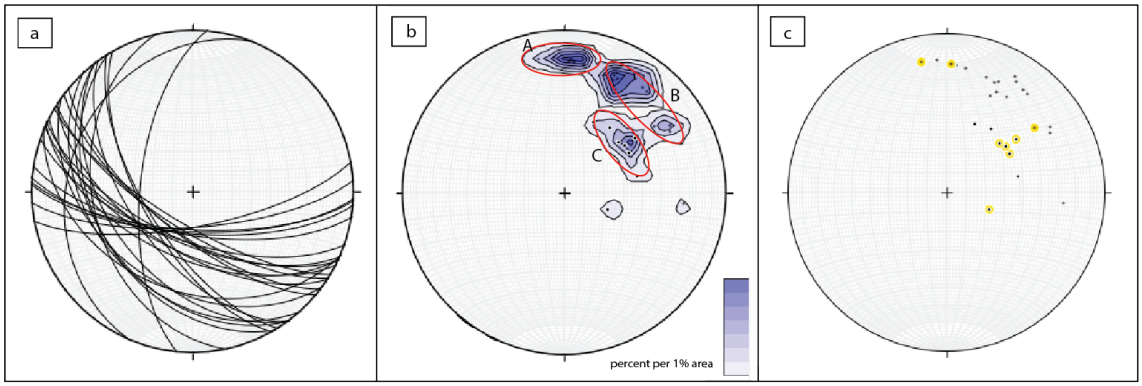

Figure 5.20: Stereoplot of all the backtilted fractures of core interpretation from VAL-01 and clustering based on their orientation, the plane projection (a), the clustering of poles are indicated by circles (b) and the poles with indication of observed offset (yellow)(c).

In figure 5.20, the back-tilted orientations of the fractures of the core can be seen. On the

core, three clusters are recognised: one striking E-W (A) at an angle of 60-70° and two striking NW-SE at an angle of 30-40°(C) and 50-70°(B). In all the clusters, both fractures with and without offset are seen, represented with a yellow dot (figure 5.20). The fractures with no visible shear could be shear fractures where the shear component was not seen on the 3.5 cm wide slab.

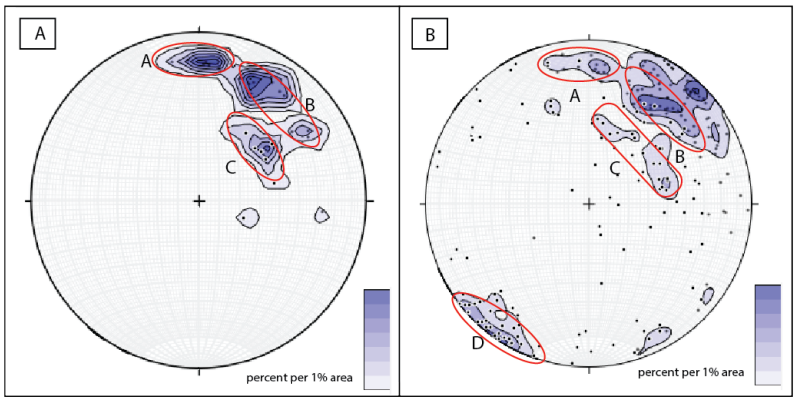

Figure 5.21: Stereoplot of the backtilted fractures on the core (A) and all the fractures of the image log interpretation (B) from VAL-01 and clustering based on their orientation

Looking at all the fracture interpreted on the image log and the core (figure 5.21), it can be seen that the fractures on the core form almost the same fracture set as in the image log. Only one fracture set is not observed in the core. This set is NW-SE striking at an angle of 90°(D).

Associated stress regimes

Based on the orientation and movement of the fractures, the stress regimes in which the fractures could have been formed are discussed. They could have been formed by a combination of a normal regime, a reserve regime, which is represented in a set of schematic block diagrams (figure 5.22). The order of the stress regimes is not known based on the attitude analysis.

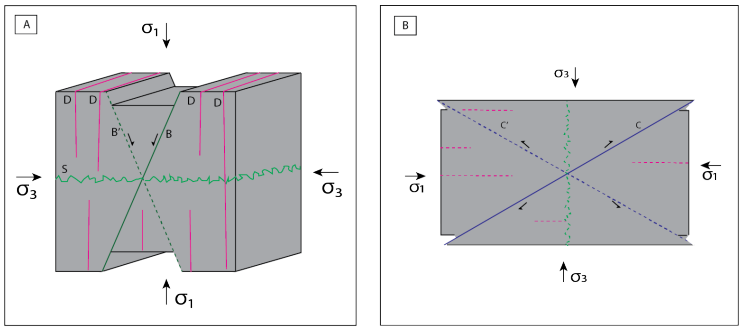

Figure 5.22: Schematic block diagram of the stress regime related to fracturing on VAL-01 based on orientations

First, in the core there are several bedding parallel stylolites seen, which are below the resolution of the AST (figure 5.23). These form perpendicular to the maximum stress direction, which in this case would be vertical indicating a normal regime. The normal regime fits the 90° dipping veins (D) and the fractures at 50-70° (B) in a NW-SE direction. The fracture (B) could form one side of a conjugate set, the other side of the conjugate set is expected to be oriented striking parallel but in the opposite direction, which is parallel to the orientation of the well, making it likely to be missed by the borehole.

Lastly, fracture set (C) can be formed as one side of a conjugate set in a reverse regime. The other side of the conjugate pair is expected to be oriented 30° dipping the opposite direction, which is sub-parallel to the orientation of the borehole and not observed.

The fractures in A are dipping south at an angle of 60° striking E-W. They are not striking parallel to the set B, C and D. They could be formed as one side of a conjugate set in a normal regime. The opposite side of the conjugate is not observed on the image log, which could be as the expected orientation is sub-parallel direction of the borehole.

It is also possible that the fractures ranging from A to B and within the spread of C are formed in a polymodal pattern, where three or more sets of faults planes have formed and slipped simultaneously (Healy et al., 2015). This could explain the spread in strike orientation.

Figure 5.23: Bedding parallel stylolite in VAL-01 (2868.45m)

5.4 Fracture Distribution in the Triassic sandstones in NLW-GT-01 and VAL-01

5.4.1 Distribution of Fracture in the NLW-GT-01 Well

Gamma Ray and Lithology The core of NLW-GT-01 is a grey sandstone with some finer-grained silt intervals. Cross-beddings with a few laminated sections dominate the sandstone in the cores. In the section, there are some clay pebbles present. These could be detrital clays reworked from floodplains near the channels. The depositional environment is considered to be braided channel deposits. In total, 2.5 m of claystones and 27.5 m of sandstones is seen. The claystones appear as small layers ranging from 1 cm to 25 cm in thickness. Looking at the fractures on the core, it can be seen that almost all the fractures are situated in sections of the core dominated by alternations of sand and claystones, or near clay pebbles (figure 5.24 and figure 5.14).

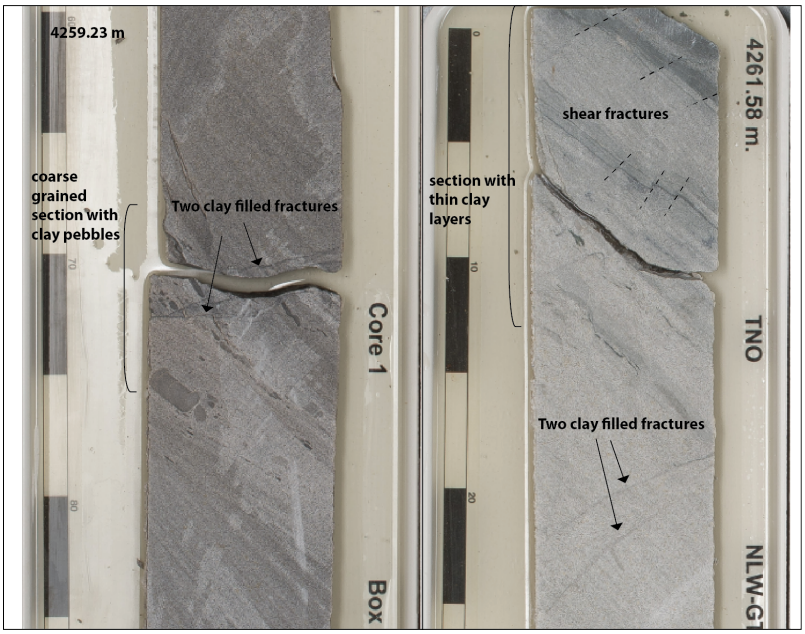

Figure 5.24: Fractures on the NLW-GT-01 core in sections with coarse grains (left) and thin clay layers (right)

In figure 5.25, it can be seen that three of the identified claystone sections (4255m, 4261m, and 4268m) of more than 20 cm correspond to gamma ray fluctuations of more than 35 API. The gamma ray fluctuation at 4257m corresponds to a section with large clay boulders (figure 5.26).

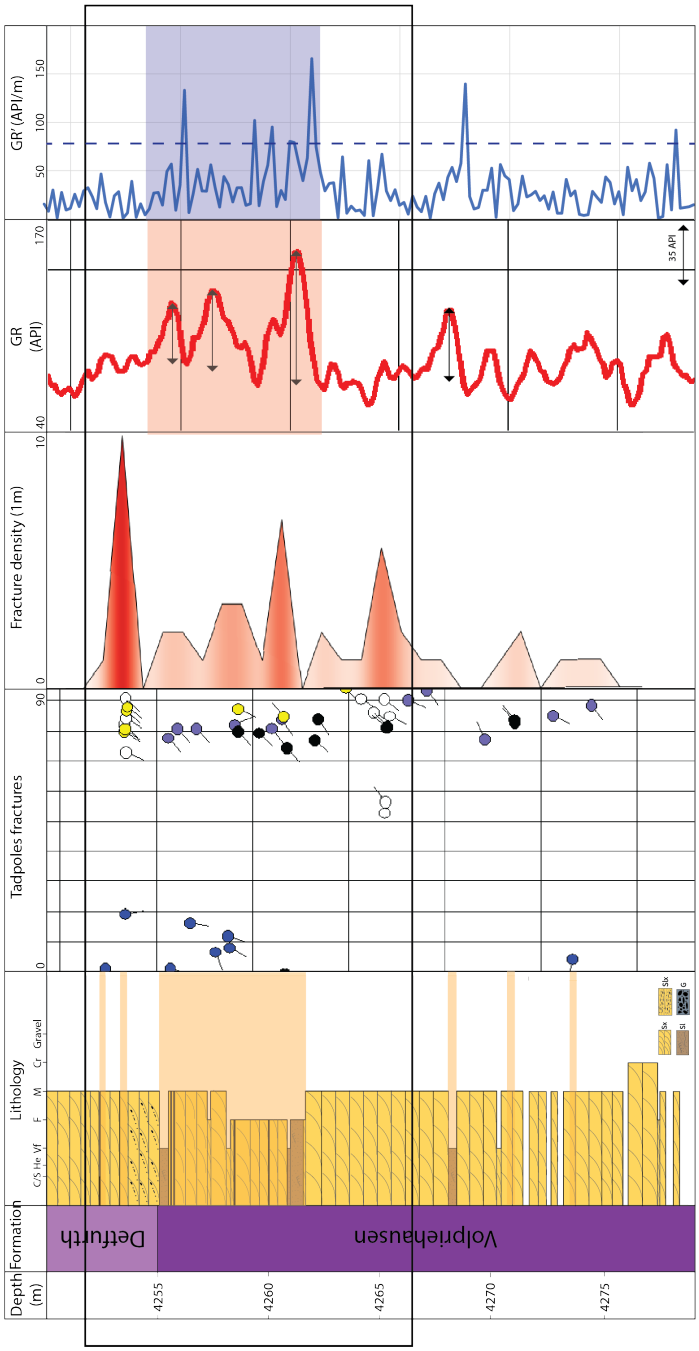

Figure 5.25: Distribution of fractures on the NLW-GT-01 core compared to the lithology and gamma ray distribution. The high fracture density within the black box, highlighted are the sections of the core with alternations in claystone and sandstone and clay pebbles (yellow) and the section with a sequence of 35 API fluctuations (red) and 75 API/m (blue).

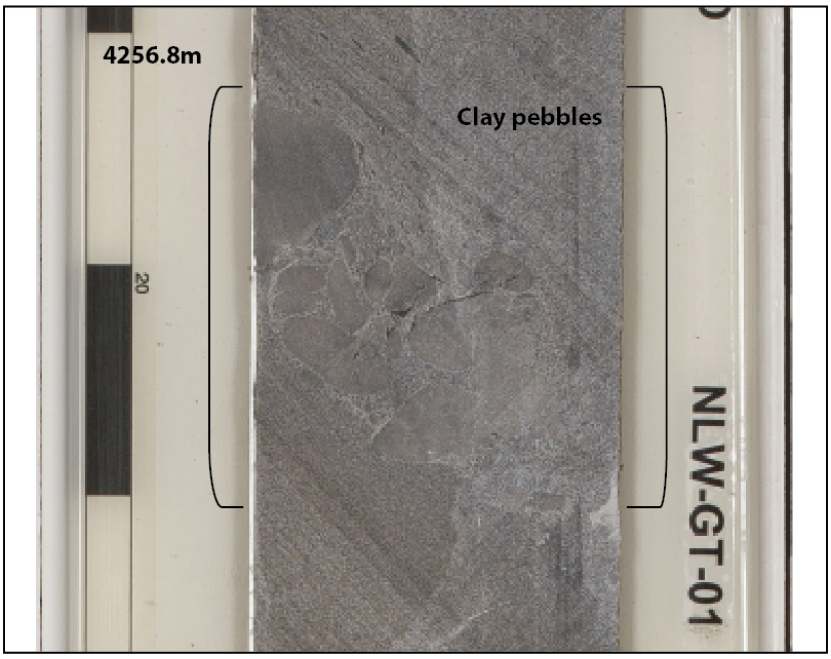

Figure 5.26: Clay pebbles on the NLW-GT-01 core (4256.8m)

The fluctuation in gamma ray is tested by the derivative of the log. The fluctuation corresponding to the clay layers are identified by a derivative of over 75 API/m.

Geomechanical Properities

A relation between high fracture densities and the geomechanical properties can be seen by comparing the density log, Poisson's ratio, the Shear modulus and Young's modulus to the high fracture densities. The Bulk modulus shows an overall increase in the average values of 35 GPa over the high fracture densities. In the Poisson's ratio, an increased value of 0.20 can be seen here. Correlations with density are not found with the high fracture densities. The Young's modulus and Shear modulus show a relation with strong fluctuation.

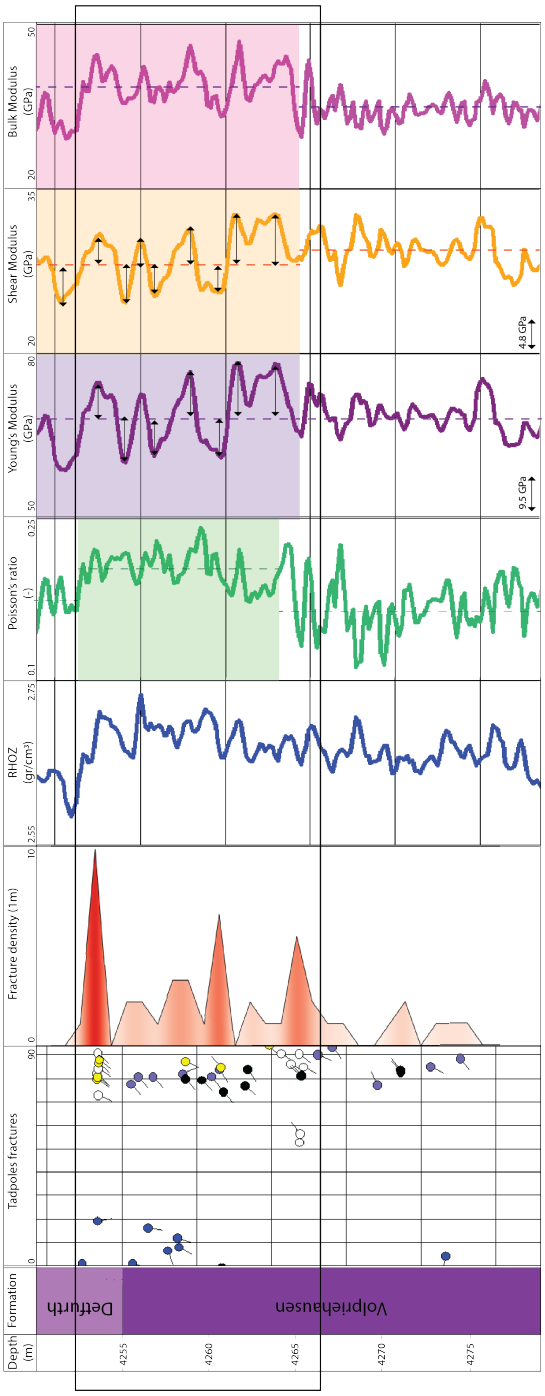

Figure 5.27: Distribution of fractures on the NLW-GT-01 core compared to the mechanical properties. The high fracture density within the black box, highlighted the Poisson's ratio above 0.2 (green), Young's modulus fluctuation (purple), Shear modulus fluctuation (yellow), Bulk modulus above 35 (pink). The arrow indicates fluctuation over the minimum fluctuation of 9.5 GPa/m and 4.8 GPa/m for Young's and Shear modulus, respectively

The fluctuations on the Young's and Shear modulus are assessed by analysing the derivative of the two logs at an increment of 20 cm. The fluctuation of 9.5 API and 4.8 API corresponding to Young's and Shear modulus fluctuation are identified by a derivative of over 25 GPa/m and 10 GPa/m, which can be seen in figure 5.28.

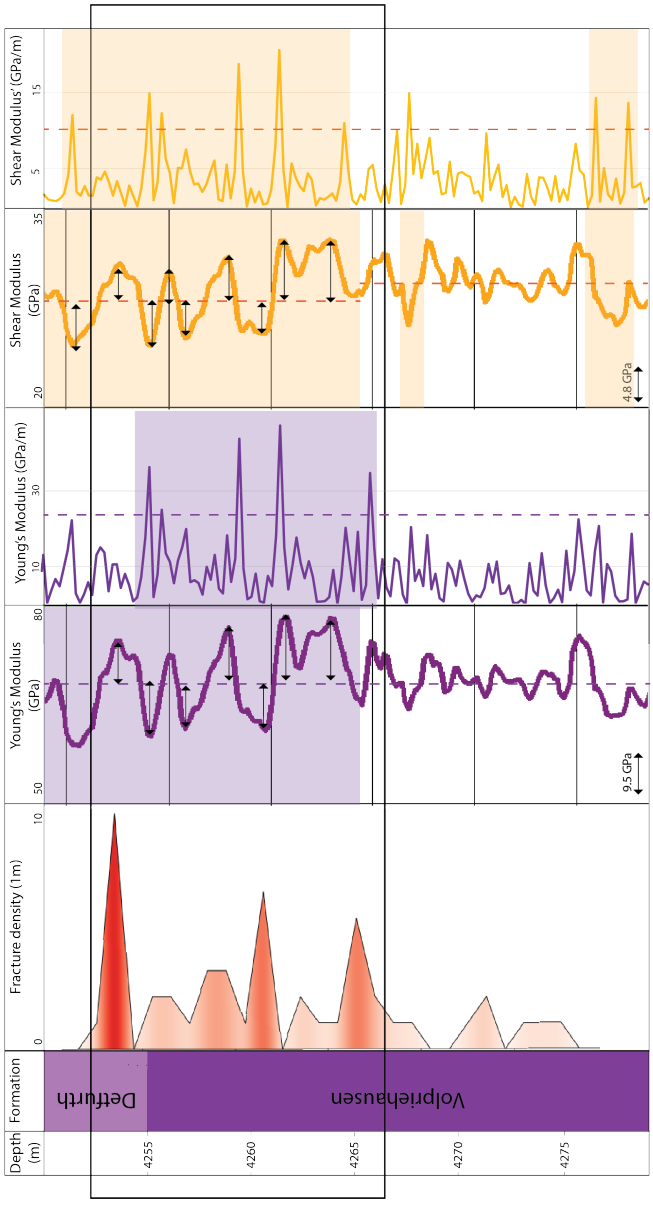

Figure 5.28: Distribution of fractures on the NLW-GT-01 core compared to the mechanical properties. The high fracture density within the black box, highlighted the Young's modulus fluctuation (purple), Shear modulus fluctuation (yellow). The arrow indicates fluctuation over the minimum fluctuation of 20 GPa/m and 10 GPa/m for Young's and Shear modulus, respectively

When looking at the image log, similar relations can be seen (figure 5.29). When comparing the gamma ray log with the fracture densities, one interval of a sequence of high gamma ray fluctuation at a depth of 4305 m does not coincide with a high fracture density area. The Bulk modulus does not show a correlation with all the high fracture density sections. The Young's modulus and Shear modulus, which are very similar, show a very consistent relation.

When looking at the image log, the Poisson's ratio of 0.2 shows a relationship with the high fracture densities, and the density log a weak correlation, where all the high fracture densities are found in sections of the well with a density higher than 2.70 gr/cm^3, but not all the sections with a higher density show high fracture densities as at a depth of 4330.0 m, (5.29).

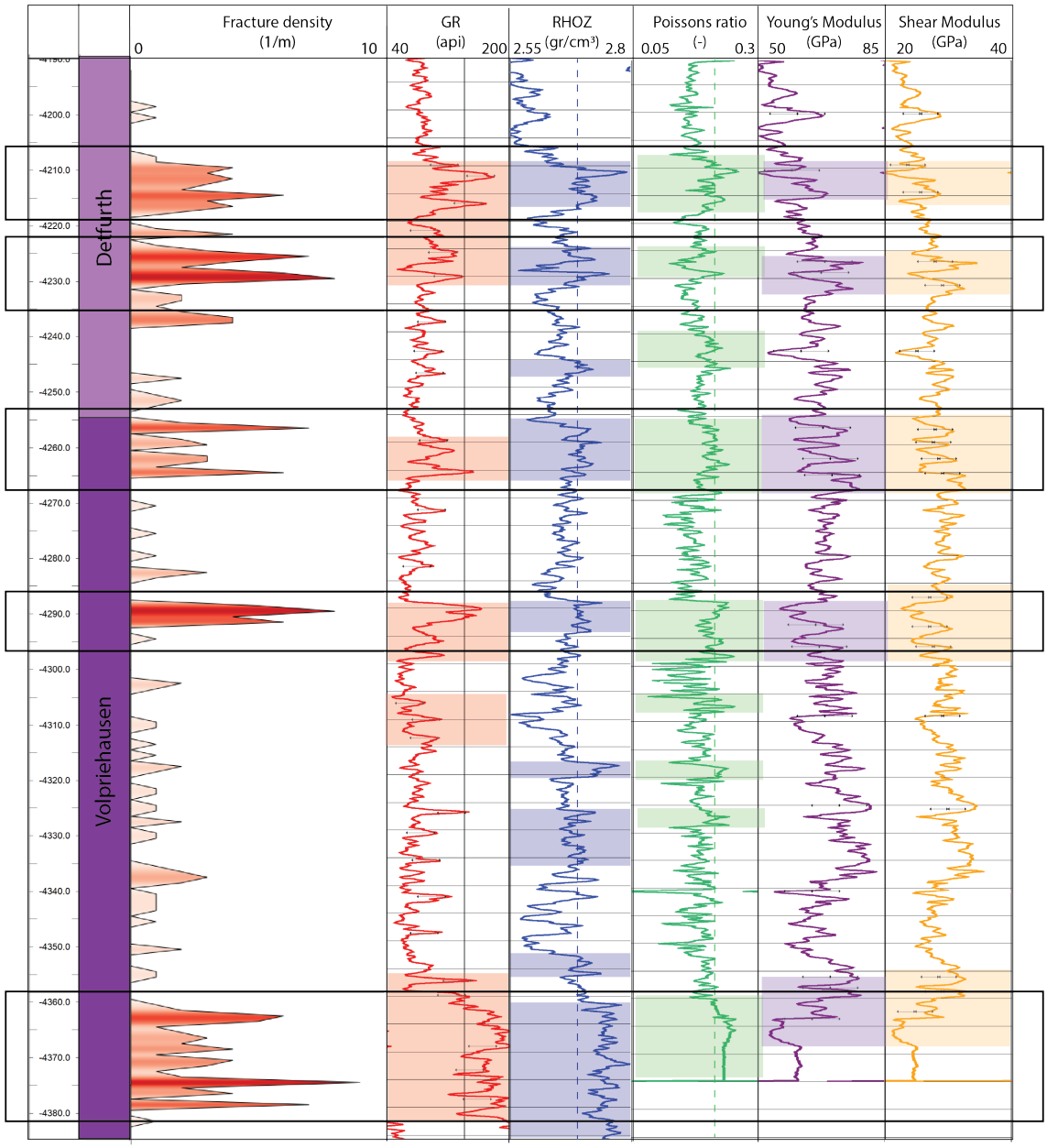

Figure 5.29: Distribution of fractures on the NLW-GT-01 image log compared to the mechanical properties. The high fracture density within the black box, highlighted the gamma ray fluctuation of 100 API/m (red), density above 2.70 gr/m3 (blue), the Poisson's ratio above 0.2 (green), Young's modulus fluctuation (purple), Shear modulus fluctuation (yellow). The arrow indicates fluctuation over the minimum fluctuation of 20 GPa/m and 10 GPa/m for Young's and Shear modulus, respectively and the 75 API/m fluctuation for the gamma ray log.

5.4.2 Distribution of Fractures in the VAL-01 Well

Gamma Ray and Lithology
In VAL-01, alternating sandstones and siltstones are observed with red to grey colours. The depositional environment is interpreted as an alluvial floodplain to a desert plain. Looking at the fractures on the core of VAL-01 it can be seen that the majority of the fractures are situated in sections of the core dominated by alternations of sand and claystones. The fractures are clustered closely together (5.30). Over the core a total of 55 m of claystone is observed and 65 m of sandstone. The claystone layers are ranging from 0.5 cm to 15 cm. There are many very thin alternations of claystone and sandstones.

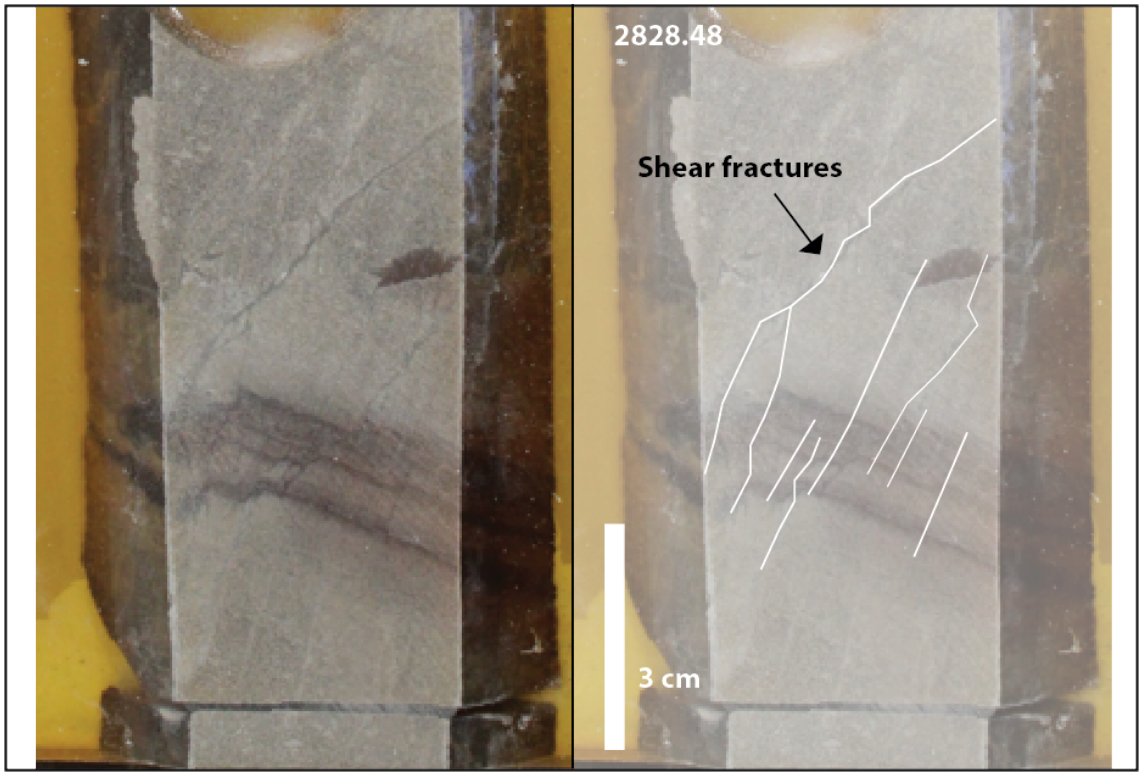

Figure 5.30: Fracture clustered on section of the VAL-01 core with alternation in bedding (2828.48m)

In figure 5.31, the distribution of the fracture density related to the gamma ray, the lithology and the grainsize boundaries can be seen. It can be seen that the high fracture dnesities are situated in intervals which have high gamma ray values of more than 75 API with fluctuation of 45 API. From 2828-2832 m and from 2854-2869 m the core is dominated by claystone, which is related to the increased gamma ray of 75 API.

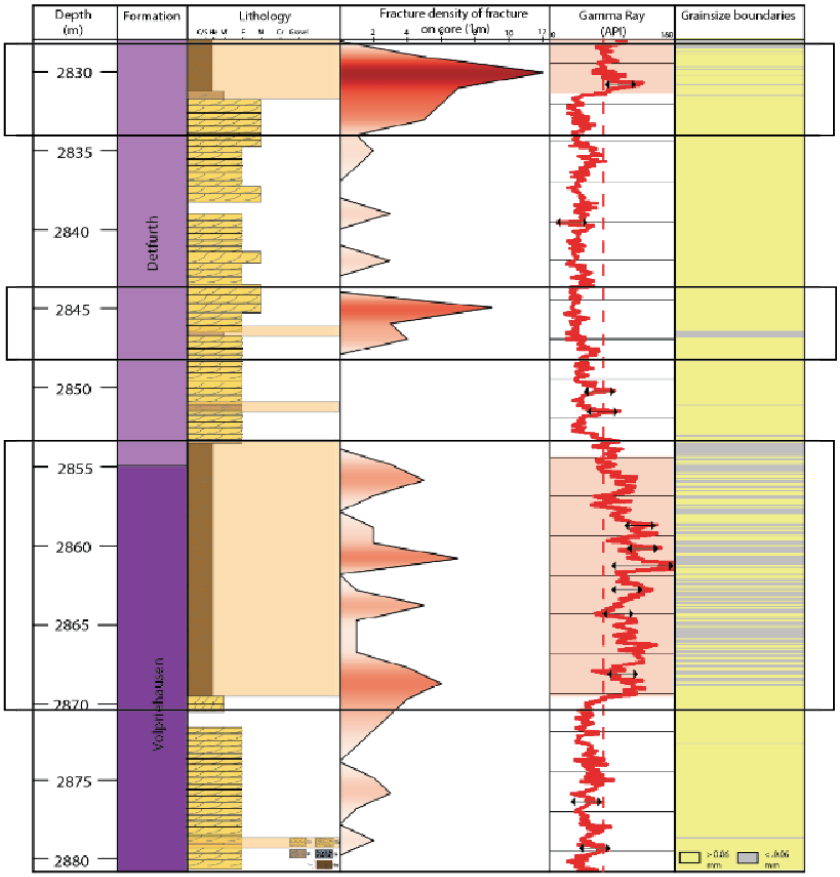

Figure 5.31: Distribution of fracture on the VAL-01 core compared to the lithology and gamma ray distribution. The high fracture density within the black box, highlighted are the sections of the core with alternations in claystone and sandstone and clay pebbles (yellow) and the section with a sequence of 45 API fluctuations (red).

The fluctuation of the gamma ray is assessed by an analysis of the derivative of the gamma ray logs (figure 5.32). It can be seen that the fluctuation correlate to the high fracture densities by a derivative of over 300 API/m.

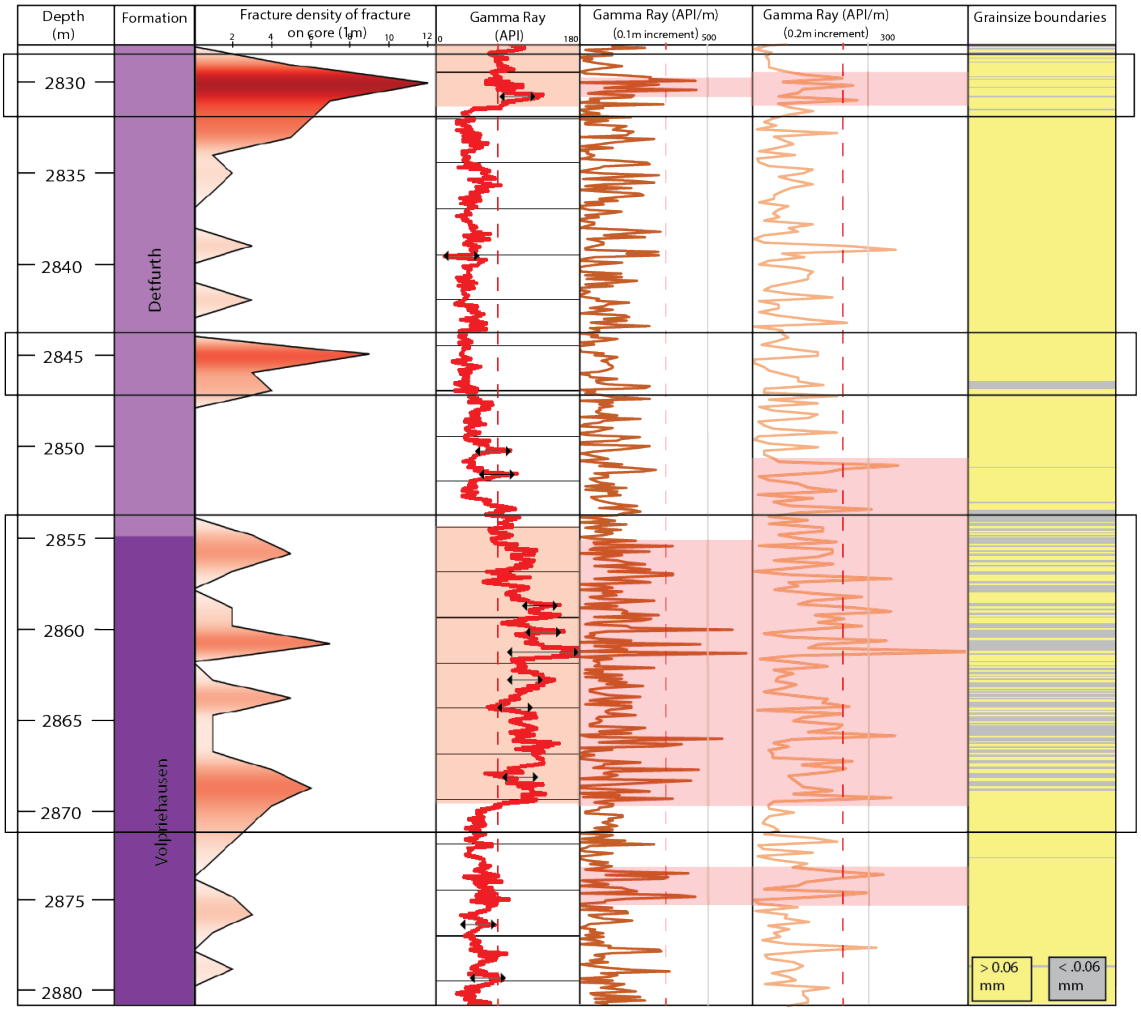

Figure 5.32: Distribution of fracture on the VAL-01 core compared to the lithology and gamma ray distribution.The high fracture density within the black box, highlighted are the sections of the core with alternations in claystone and sandstone and clay pebbles (yellow) and the section with a sequence of 45 API fluctuations (red).

Geomechanical Properties

Aside form that the same relation can be seen with the density log and the Poisson's ratio, where higher density values of $+2.65\ gr/cm^3$ and Poisson's ratio of $+0.21$ coincide with the high gamma ray intervals and the high fracture densities. The Young's and Shear modulus fluctuations and the high fracture densities show an occasional correlation with

fluctuation of 20.5 and 10 GPa respectively.

The fluctuations on the Young's and Shear modulus are assessed by analysing the derivative of the two logs. The fluctuation corresponding to Young's and Shear modulus fluctuation are identified by a derivative of over 30 GPa/m and 20 GPa/m (figure 5.33) .

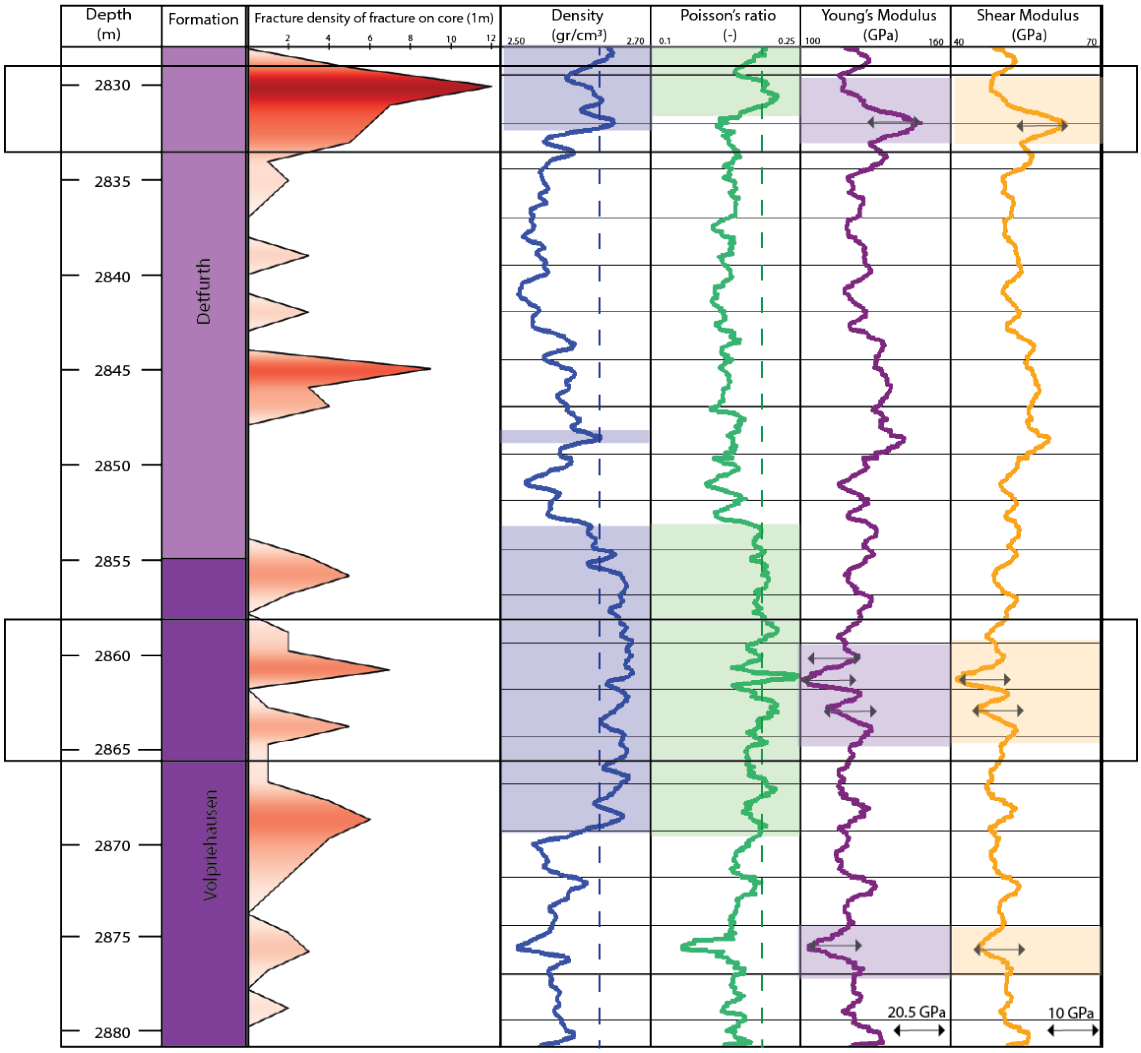

Figure 5.33: Distribution of fractures on the VAL-01 core compared to the mechanical properties. The high fracture density within the black box, highlighted density above 2.65 gr/m3 (blue), the Poisson's ratio above 0.21 (green), Young's (purple), Shear modulus fluctuation (yellow). The arrow indicate fluctuation over the minimum fluctuation of 30 GPa/m and 20 GPa/m for Young's and Shear modulus respectively and the 150 API/m fluctuation for the gamma ray log.

On the image log section (figure 5.21), the same relations as in the core can be seen. Here is could however be seen that the relation does not coincides at all times and in both directions from fracture density to Young's modulus, Shear modulus, Gamma Ray, Poisson's ratio and vice versa.

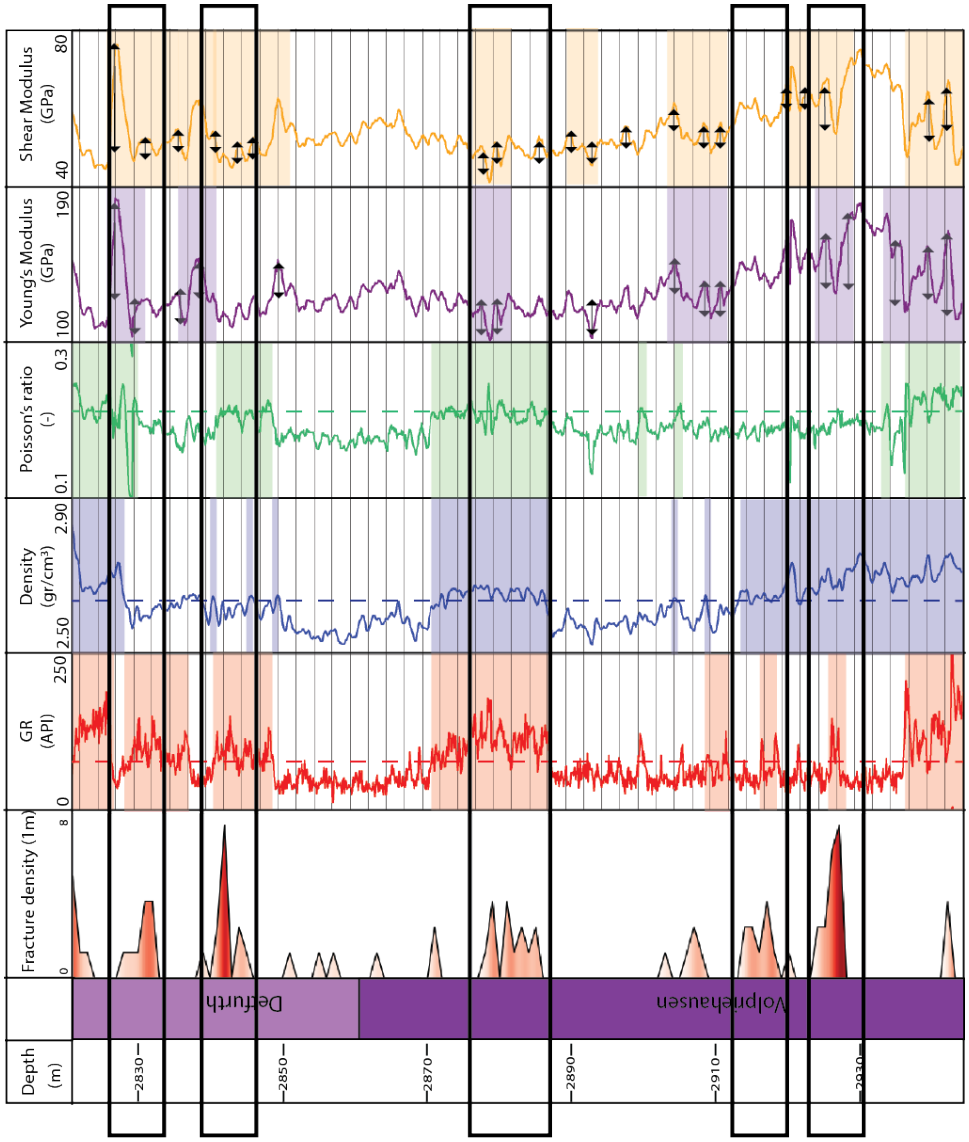

Figure 5.34: Distribution of fractures on the VAL-01 image log compared to the mechanical properties. The high fracture density within the black box, highlighted density above 2.65 gr/m3 (blue), the Poisson's ratio above 0.21 (green), Young's (purple), Shear modulus fluctuation (yellow). The arrow indicate fluctuation over the minimum fluctuation of 30 GPa/m and 20 GPa/m for Young's and Shear modulus respectively and the 150 API/m fluctuation for the gamma ray log (red).

Chapter 6

Discussion

In the previous chapters, the identified fractures on the core and image logs of VAL-01 and NLW-GT-01 are described. The impact of the fracture types on permeability, the stress regimes associated with the fractures and the distribution of the fractures over depth are assessed. Aside from that improvements of the research and future research are discussed.

6.1 Impact of the Different Fracture Types on Permeability

Joints
The joints will have the highest impact on fracture permeability, as they are likely to have the biggest aperture. The identification of joints on the core and image logs is very uncertain.

In the study by Boersma et al. 2021, they suggest to identify the joints based on the continuity of the sinusoidal form on the image log in combination with the resistivity response. However, by comparison of the individually matched fractures on the core and image log, no correlation between the different fracture types and image log response has been seen in resistivity nor in sinusoidal continuity (chapter 5.2.3).

The uncertainty in the joints is subjected to the uncertainty in the interpretation of the natural fracture and of the drilling-induced fractures. Based on the appearance on the core the joints could not have been distinguished from the drilling-induced fractures. The interpretation relies on the orientation of the drilling-induced fractures. On the core of NLW-GT-01 16 joints have been identified out of 50 natural fractures, which have a 16% uncertainty. On the core of VAL-01 17 joints have been classified out of 119 fracture, which have a 13% uncertainty.

For the analysis of fractures in the West Netherlands Basin in the Detfurth and Volpriehausen, two wells are used. This constrains the data to the immediate surroundings of the wells. The VAL-01 well is situated in a horst of the system and the NLW-GT-01 in the graben both near faults. The fracture density observed near faults is expected to be higher (?, ?; Nelson, 2001), especially in the graben. The fracture density thus the joint density in these well could be overestimating the number of fractures. This should

be taken into account when assessing the fracture density over the basin.

Stylolites
On the cores of both NLW-GT-01 and VAL-01 stylolites have been found. All stylolites were once conduits of flow which then later can become permanent or temporary baffles of flow (Bruna, 2019). For a stylolite to form and grow, it requires fluid circulation (Bruna, 2019; Martin Baron, 2007). The presence of the stylolite is therefore indirect proof of a past permeability of the formation.

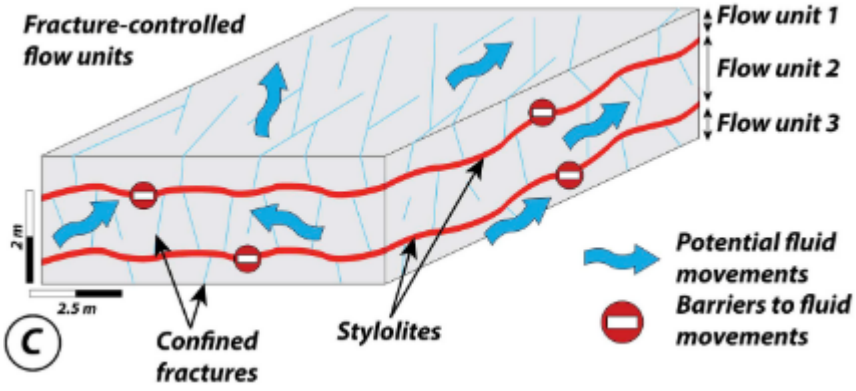

Figure 6.1: Block diagram showing the potential 3D fluid flow pathways. The reservoir is compartmentalised and fracture-controlled flow units can potentially be disconnected from each other (Bruna et al., 2019)

The bedding parallel stylolites are the first features formed in NLW-GT-01. Along the surface of the stylolite, insoluble minerals are concentrated, providing a mechanical discontinuity, which baffles flow across the stylolite but facilitates the flow along the stylolite(Bruna, 2019). As these stylolites are formed first, the fractures which are formed later cut the bedding parallel stylolites. So they will not form a horizontal baffle to the fractures.

Depending of the maturity of a stylolite, the stylolite can remain a conduit of flow. When the stylolite has reached its maximum roughening stage, the available pore space in the matrix is likely to be filled by the product of dissolution and stylolites became inactive (Bruna, 2019).

The tectonic stylolites at 90° to the bedding are formed in the last stress regime. These could have an impact on the fractures which were formed previously.

Drilling-Induced Fractures
Based on the drilling-induced fractures of the well in NLW-GT-01 and the borehole-break outs in VAL-01, the in-situ horizontal minimum and maximum stress orientations are identified. The in-situ horizontal minimum stress orientation is NE-SW and the in-situ horizontal maximum stress orientation is NW-SE. The observations from the two wells agree and are in accordance with the stress orientations found in other wells and with literature (Heidbach et al., 2018). The in-situ stress direction compared to the orientation

of the fractures and the stylolites can influence the aperture of the fractures, if they are oriented in a favourable direction opening to the minimum stress direction (Lorenz & Cooper, 2020).

The drilling induced fractures cannot contribute to the fracture permeability. They are artifacts created during the drilling process and penetrate not more than the the radius of the borehole into the formation (Aadnoy & Bell, 1998).

6.2 Tectonic events in the West Netherlands Basin related to fracturing

It is important to understand the tectonic events related to fracturing in the West Netherlands Basin. Different fracture patterns will be created in different regimes over the basin, which could lead to different combinations of fracture patterns and connectivity between the fractures. If the fractures are too aligned, they are connected along the strike but not normal to the strike direction. It is important to understand these when assessing the impact of fractures on the geothermal potential of a region.

6.2.1 Stress regimes in NLW-GT-01

In the south of the West Netherlands Basin (NLW-GT-01), in the edge of the basin, three tectonic events are recognised, a normal regime, a transition and a reverse regime (figure 5.17).

The normal regime is defined based on 7 high confidence stylolites on the core. These have to be created in a normal regime based on the relation of the sigma 1 normal to the bedding parallel stylolites. In NLW-GT-01, there has been seen a lot of evidence for pressure solution processes based on thinsection analysis (Maniar, 2019). Making it likely that pressure-solution had been taking place, creating the stylolites. There are not many reviews on how to recognize stylolites and compare them in clastic formations. There is a chance that not all the stylolites have been identified. A thin clay layer could have been misinterpreted as a clay layer while it is a stylolite. The additional Mode I fracture at 90° to the bedding and the possible conjugate set comply with this system.

The Mode I fractures perpendicular to the bedding, do not fit an Andersonian stress orientation. The shear fractures are formed at approximately 90°to the stylolite, which means that they are not at a compatible angle to be part of the conjugate set from the normal regime. The origin of the shearing event is not clear. The fractures could have formed as Mode I fractures during the normal regime and have sheared later when the stress orientation shifted. They could have formed due to a local stress anomaly or they could have formed during a time where the bedding was tilted.

The reverse regime is defined by the stylolite at a 90° angle to the bedding. On the core only one of these stylolites has been found. However, the identified clay filled veins could be stylolites and not veins. The clay cemented fractures could be analyzed and validated

by looking at the change in permeability normal to the stylolite plane on thinsections and by the pressure-solution behaviour. No Mode I or conjugate fractures have been identified fitting this regime. The conjugate set formed during the normal regime could be reactivated in this phase.

The fracture on the core interval are representative for the fractures on the image logs interval. Only one set of fractures is not observed in the core, which is at a slightly different strike. This fracture set could be created by a separate normal stress regime or be formed in association with the other normal fractures in a polymodal system.

6.2.2 Stress regimes in VAL-01

In VAL-01, two stress regimes are identified, similar to NLW-GT-01, consisting of a normal and a reverse regime.

The normal regime is defined by the bedding parallel stylolites on the core, there are 10 stylolites observed. The Mode I fractures at 90° to the bedding support this regime and one side of a possible conjugate pair. Part of these fractures did not show an offset on the core. This offset could have been missed on the 3 cm polymer slab.

The reverse regime is less certain as it is only supported by the indirect evidence of a conjugate set. Part of these fractures did not show an offset on the core, which could have been missed on the 3 cm polymer slab. There are no tectonic stylolites or Mode I fractures. The fractures display a range of orientations striking N-S to NW-SE. These fractures could have been formed in a polymodal system or by separated events.

6.2.3 Tectonic stress regimes in the West Netherlands Basin

The fracture patterns in VAL-01 and NLW-GT-01 both however show the same dominant dip direction and the same stress regimes (figure 6.2).

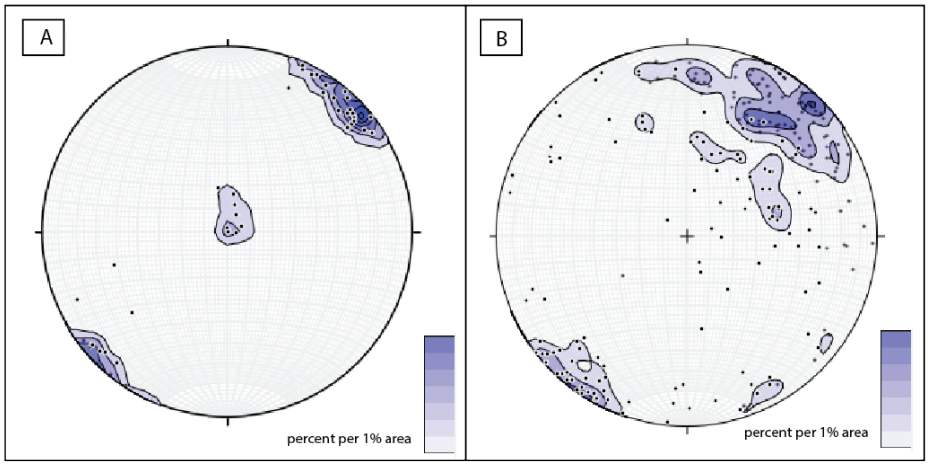

Figure 6.2: Backtilted fracture orientation at in NLW-GT-01 and VAL-01

When comparing the fracture orientations with the fault orientations it can be seen that these too are aligned (figure 6.3. Worum et al. (2005) studied fault orientations patterns over the West Netherlands Basin and the Roer Valley graben. In domain E, NLW-GT-01 is situated and in domain F, VAL-01. The main fault orientation from Worum et al. 2005 coincide with the main fracture orientations, this could indicate that the fractures are formed due the larger scale events and less likely formed in association of small scale anomalies.

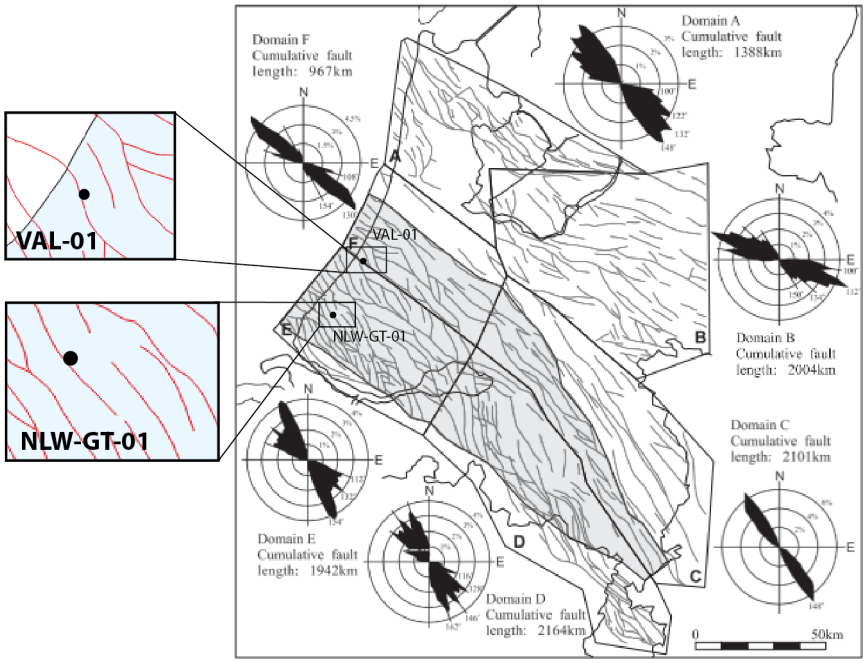

Figure 6.3: Distribution of Early to Middle Mesozoic faults in the West Netherlands Basin and the Roer Valley Graben (Modified after Worum et al., 2005)

The normal regime can be related to the burial of the formation during the extensional phase of the WNB during the Mesozoic, either in the Early, Mid or Late Kimmerian Phase. The reverse regime can be related to the inversion of the WNB during the Late-Mesozoic and Cenozoic. The conjugate fractures created in the normal regime could be reactivated in the reserve regime. This reactivation also happened on larger scale on the faults (van Wijhe, 1987; de Jager, 2007). The relative timing of the events is based on one section of the core in NLW-GT-01, however it is in accordance with the literature history (van Balen et al., 2000; de Jager, 2007).

6.3 Fracture distribution in the West Netherlands Basin

The distribution of the fracture over the length of the core and image log is assessed. In figure 6.5 and 6.4, it can be seen that there is a relation with the Gamma Ray values and with the geomechanical properties.

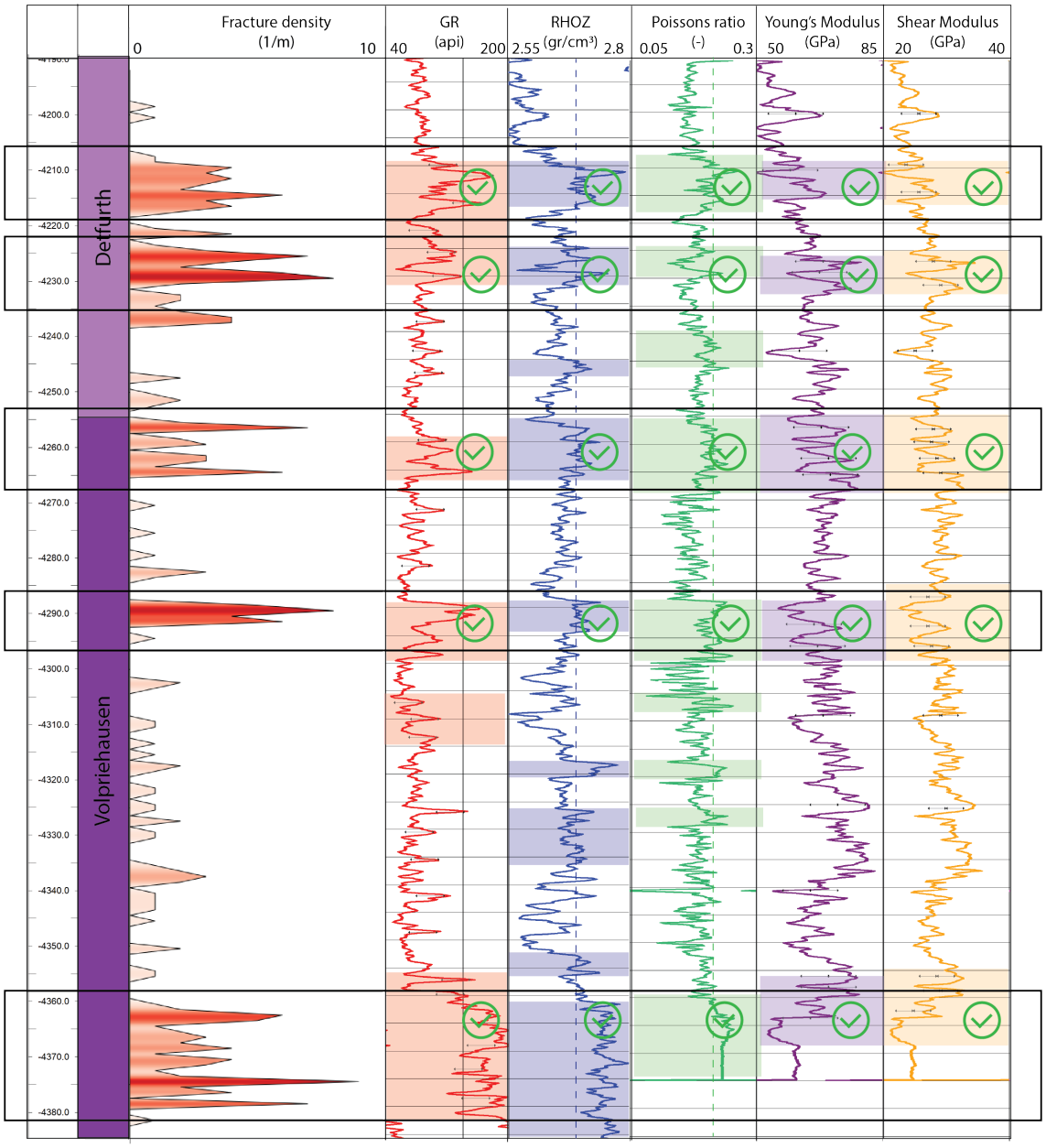

Figure 6.4: Distribution of fractures on the NLW-GT-01 image log compared to the mechanical properties. The high fracture density within the black box, highlighted density above 2.65 gr/m3 (blue), the Poisson's ratio above 0.21 (green), Young's (purple), Shear modulus fluctuation (yellow). The arrow indicate fluctuation over the minimum fluctuation of 25 GPa/m and 10 GPa/m for Young's and Shear modulus respectively and the 75 API/m fluctuation for the gamma ray log. A positive correlation is indicated by a green check-mark and a negative correlation by a red cross

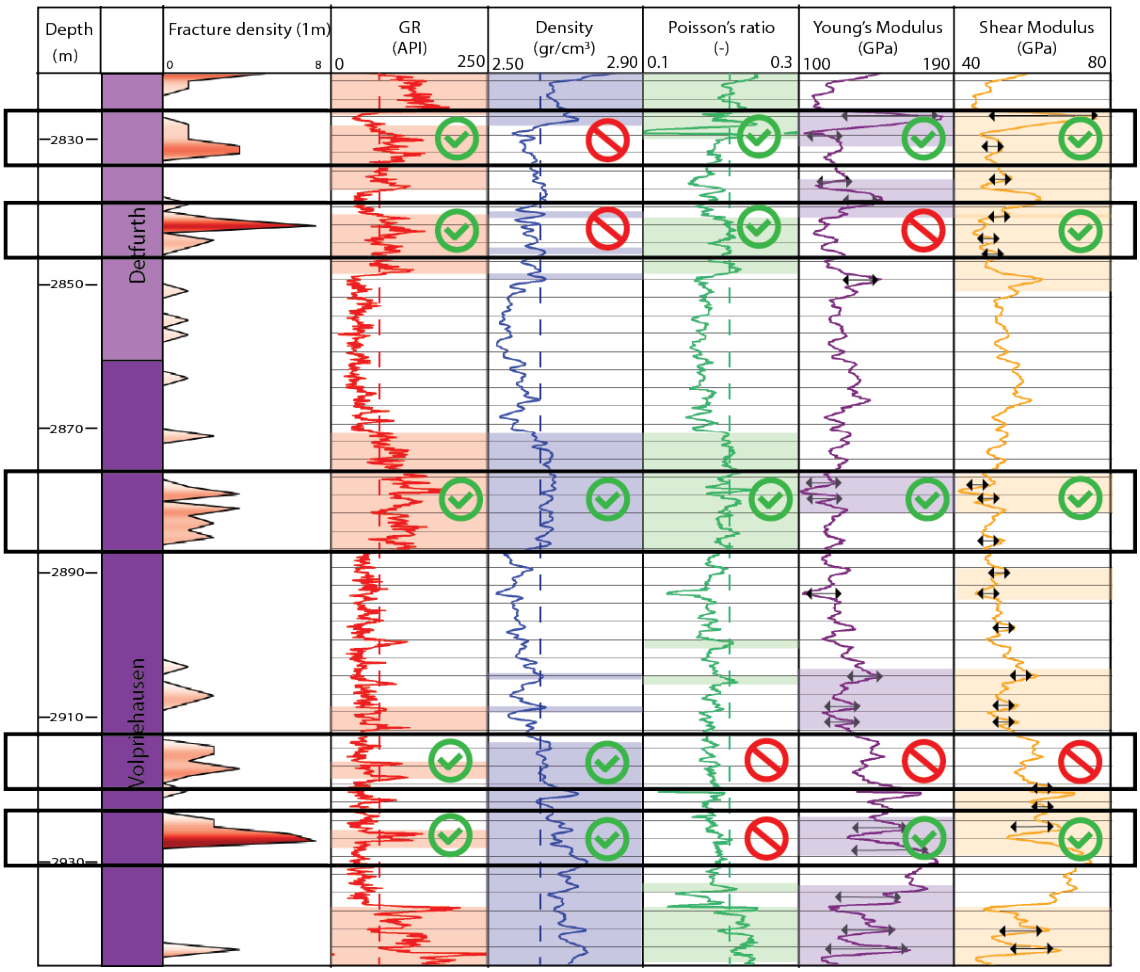

Figure 6.5: Distribution of fractures on the VAL-01 image log compared to the mechanical properties. The high fracture density within the black box, highlighted density above 2.65 gr/m3 (blue), the Poisson's ratio above 0.21 (green), Young's (purple), Shear modulus fluctuation (yellow). The arrow indicate fluctuation over the minimum fluctuation of 30 GPa/m and 20 GPa/m for Young's and Shear modulus respectively and the 150 API/m fluctuation for the gamma ray log. A positive correlation is indicated by a green check-mark and a negative correlation by a red cross

The high fracture densities are concentrated in section with alternations of sandstone and claystone layers in both the NLW-GT-01 and VAL-01 well. In NLW-GT-01 the alternations are characterised by fluctuation of 75 API/m. In this well no overall increase in the Gamma Ray has been encountered. In VAL-01 the alternation are characterised by fluctuation of over 300 API/m and a higher average of 75 API.

By comparison of the fracture densities in NLW-GT-01 and VAL-01 on the core, a overall fracture density of 1.6 and 2.0 is observed. As mentioned in chapter 2.3 by Geluk et al. 2005, in the southwestern region of the WNB, the formations are more sand-rich, implying a proximal position to the major fluvial system. This where NLW-GT-01 is probably

located. VAL-01 on the other side is located towards the northwest, indicating a more distal location from the main channel characterised by a succession of predominantly lacustrine siltstones and claystones with subordinate sandstones. In the more distal location more clay and sandstone alternations are expected, which could explain the overall higher fracture density

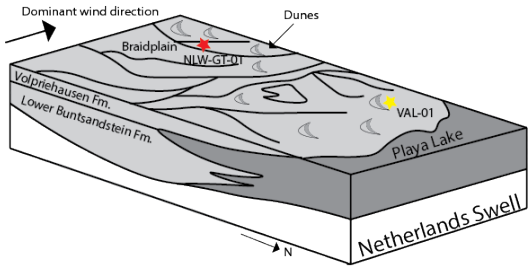

Figure 6.6: Depositional model for the Lower Buntsandstein and Volpriehausen Formation in the southern Netherlands. The red star indicated NLW-GT-01 and the yellow star VAL-01, light shading is predominantly sandstones; darker shading indicates predominantly claystones (Modified after Geluk et al., 2005)

The fluctuations in gamma ray are related to the alternating beds of sandstone and claystone. The difference in fluctuation in NLW-GT-01 and VAL-01 (75 API/m and 300 API/m), is dependent on average API of the clay and sandstones, which is also related to the depositional environment.

The lithological variability produces Young's and Shear modulus variability that seems to be driving increased fracture density rather than their absolute value.

This could be related to a common attribute of joints in layered sedimentary rock. It is observed that fracture spacing is proportional to layer thickness (Bai & Pollard, 2000; Bai et al., 2000; Olson, 2004), where the layer boundary forms a mechanical boundary. The distance between imposed fractures confined to a layer is subjected to tension.

With increasing strain eventually the fractures are spaced so closely that no more fractures can infill, even with increasing strain. The additional strain is accommodated by further opening of existing fractures. This minimum fracture spacing is called fracture saturation (Bai & Pollard, 2000; Bai et al., 2000).

The critical value of the fracture spacing to layer thickness ratio is independent of the average strain of the fractured layer, and it increases with increasing ratio of Young's modulus of the fractured layer to that of the neighboring layers. The critical value increases with increasing Poisson's ratio of the fractured layer, and with increasing overburden stress (depth), but it decreases with increasing Poisson's ratio of the neighboring layers (Bai & Pollard, 2000).

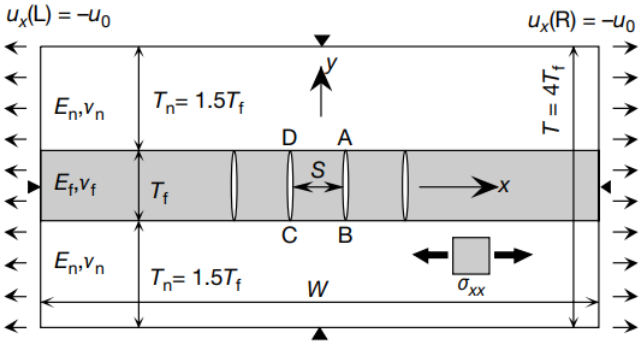

Figure 6.7: Finite element model and its boundary conditions with four fractures of spacing S in the fractured layer. Displacements are represented by u, and the subscripts x and y indicate the corresponding directions. L, left; R, right. The thicknesses are represented by T. The subscript n indicates the neighbouring layers, and f indicates the fractured layer. E, Young's moduli; n, Poisson's ratios; jxx, horizontal stress; W, width of the model(Bai et al. 2000)

Only 4 out of the 45 fractures in VAL-01 is seen to be bed confined fractured. The assessment of the fractures compared to the bedding is difficult on a 3.5 cm slab, so this could not be tested.

In NLW-GT-01, the fracture stratigraphy and the mechanical stratigraphy coincide completely. It is characterised by a sequence of fluctuations of 25 GPa/m and 10 GPa/m in Young's modulus and Shear modulus, respectively. While in VAL-01, the fracture stratigraphy and the mechanical stratigraphy partially coincide, by a sequence of fluctuations of 30 GPa/m and 20 GPa/m in Young's modulus and Shear modulus, respectively.

Fracture stratigraphy reflects a specific loading history and mechanical stratigraphy during failure. The mechanical properties in VAL-01 could have been altered with time due to changes in diagenesis or compaction. The mechanical stratigraphy and fracture stratigraphy need not coincide (Laubach et al., 2009).

6.4 Recommendations

To improve this research there are several ways to further limit the uncertainties and to extent on the study.

To assess the impact of the joints it is recommended to incorporate the uncertainty in the fracture classification and the fracture density in a fracture model as in Boersma et al., 2021. Aside from that the length of the fractures measured over the polymer slab can be used to estimate the fracture lengths in combination with the sinusoidal traces on the image logs. Ozkaya (2003) describes a method to estimate fracture length based on the relative frequency of fractures, which have a complete sinusoid traces on image logs.

For future projects it is recommended to perform a welltest, to reduce the uncertainty in the interpretation of the joints in the Main Buntsandstein Subgroup in the West Netherlands Basin.

The properties of the stylolites and the clay filled fractures could be analysed with thin-sections. This could also give more information on the cementation phases and diagenesis in the formation.

Thin sections of the cemented fractures can also evaluate the occurrence of partial cemented fracture. Field observations of fractures show great variability from being enlarged by dissolution reactions, to having only minute cement accumulations, to showing partial occlusion by cements but retaining porosity, to fully cement filled (Laubach et al., 2019; Tokan-Lawal et al., n.d.). Cements may greatly reduce both the local permeability and the large scale flow connectivity of fracture systems and dissolution may greatly increase them. The chemical effects on network connectivity need to be systematically investigated and included in fluid flow prediction (Laubach et al., 2019).

The mechanical stratigraphy in NLW-GT-01 and VAL-01 can be looked further into to assess why the fracture stratigraphy only partly coincides in VAL-01 and completely coincides in NLW-GT-01

Chapter 7

Conclusion

In this study, a re-evaluation is performed of the well data of the NLW-GT-01 and VAL-01 wells. An analysis comparing core, geophysical, and image logs is performed to document the drivers and characteristics of natural fracture distribution in the WNB and investigate the geological parameters influencing the development of natural fractures in the Main Buntsandstein Subgroup.

On the core of NLW-GT-01 and VAL-01, five types of fractures are observed: veins, joints, Mode II fractures, stylolites and drilling-induced fractures. They have a dominant NW-SE strike orientation.

The drilling-induced fractures and the borehole breakouts indicate a NE-SW oriented in-situ minimum stress and an NW-SE oriented maximum stress. The joints, veins and tectonic stylolites are favourably oriented to be open based on their orientation compared to the in-situ stress orientation in NLW-GT-01.

The fractures are associated with large-scale tectonic events. During the burial of the formation related to the extensional phase of the WNB during the Mesozoic, veins, joints, conjugate fractures, and stylolites could be formed in a normal regime. During the inversion of the basin in the Late Mesozoic-Cenozoic, tectonic stylolites could have been formed, and the previously formed conjugate fracture could have been reactivated in a reverse regime.

Natural fractures are concentrated in more heterolithic intervals of the VAL-01 and NLW-GT-01 wells in both image logs and cores. These heterolithic sections display alternations of medium sandstones with silt- and claystones. These can be recognised by fluctuation in the Gamma Ray. In NLW-GT-01, a minimum fluctuation of 75 API/m characterises the fracture concentrations, and in VAL-01, a minimum fluctuation of 300 API/m.

The identification of more fractures in VAL-01 compared to NLW-GT-01 can be explained by the difference in basin location. VAL-01 was located in the centre of the basin where distal playa environments produced more fine-grained material alternating with coarser sands. The more proximal NLW-GT-01 was dominated by fluvial sands. The lithologi-

cal variability produces Young's and Shear modulus variability that seems to be driving increased fracture density rather than the absolute value of the Young's modulus causes this. In NLW-GT-01, the fracture stratigraphy and the mechanical stratigraphy coincide completely. It is characterised by a sequence of fluctuations of 25 GPa/m and 10 GPa/m in Young's modulus and Shear modulus, respectively. In VAL-01, the fracture stratigraphy and the mechanical stratigraphy partially coincide, by a sequence of fluctuations of 30 GPa/m and 20 GPa/m in Young's modulus and Shear modulus, respectively.

References

Aadnoy, B. S., & Bell, J. S. (1998). Classification of drilling-induced fractures and their relationship to in-situ stress directions. *The Log Analyst*, *39*, 64-80.

Bai, T., Pollard, D., & Gao, H. (2000, 03). Explanation for fracture spacing in layered materials. *Nature*, *403*, 753-6. doi: 10.1038/35001550

Bai, T., & Pollard, D. D. (2000). Fracture spacing in layered rocks: a new explanation based on the stress transition. *Journal of Structural Geology*, *22*(1), 43-57. Retrieved from `https://www.sciencedirect.com/science/article/pii/S0191814199001376` doi: https://doi.org/10.1016/S0191-8141(99)00137-6

Bath, A. H., Milodowski, A. E., & Spiro, B. (1987). Diagenesis of carbonate cements in permo-triassic sandstones in the wessex and east yorkshire-lincolnshire basins, uk: a stable isotope study. *Geological Society, London, Special Publications*, *36*(1), 173-190. doi: 10.1144/GSL.SP.1987.036.01.14

Boersma, Q., Athmer, W., Haege, M., Etchebes, M., Haukas, J., & Bertotti, G. (2020). Natural fault and fracture network characterization for the southern ekofisk field: A case study integrating seismic attribute analysis with image log interpretation. *Journal of Structural Geology*, *141*(1), 375-389. doi: https://doi.org/10.1016/j.jsg.2020.104197

Boersma, Q., Bruna, P., de Hoop, S., Vinci, F., Tehrani, A., & Bertotti, G. (2021). The impact of natural fractures on heat extraction from tight triassic sandstones in the west netherlands basin: a case study combining well, seismic and numerical data. *Netherlands Journal of Geosciences*, *100*(e6), 1-23. doi: https://doi.org/10.1017/njg.2020.21

Bruna, P. O. (2019). Are stylolites fluid-flow efficient features? *Journal of Structural Geology*, *125*(1), 270-277. doi: https://doi.org/10.1016/j.jsg.2018.05.018

Chatterjee, S., & Mukherjee, S. (2023). Review on drilling-induced fractures in drill cores. *Marine and Petroleum geology*, *151*(106089), 270-277. doi: https://doi.org/10.1016/j.marpetgeo.2022.106089

Davis, G., & Kluth, C. (2012). *Structural geology of rocks and regions.* Wiley.

de Jager, J. (2007). Geological development. In T. Wong, D. Batjes, & J. de Jager (Eds.), *Geology of the netherlands* (p. 5-26). Amsterdam: Royal Netherlands Academy of Arts and Sciences.

Felder, M., & Fernandez, S. (2018, February). *Core hot shot nlw-gt-01* (Tech. Rep. No. -). The Hague: PanTerra Geoconsultants B.V.

Fossen, H. (2010). *Structural geology.* Cambridge University Press.

Geluk, M. (1998, 01). Palaeogeographic and structural development of the triassic in the netherlands, new insights. *Epicontinental Triassic 1*, *1*, 545-570.

Geluk, M. (2005). Stratigraphy and tectonics of permo-triassic basins in the netherlands and surrounding areas..

Geluk, M., Plomp, A., & van Doorn, T. (1996). Development of the permo-triassic succession in the basin fringe area, southern netherlands. In H. E. Rondeel, D. A. J. Batjes, & W. H. Nieuwenhuijs (Eds.), *Geology of gas and oil under the netherlands: Selection of papers presented at the 1983 international conference of the american association of petroleum geologists, held in the hague* (pp. 57–78). Dordrecht: Springer Netherlands. doi: 10.1007/978-94-009-0121-6-7

Geluk, M., & Röhling, H. (1997, 01). High-resolution sequence stratigraphy of the lower triassic buntsandstein in the netherlands and northwestern germany. *Geologie en Mijnbouw*, *76*, 227-246. doi: 10.1023/A:1003062521373

Geoscience, W. A. (1998, 7). *St image analysis and structural interpretation of well val-01* (Tech. Rep. No. 1). Den Helder: NAM.

Gonçalves, C. A., & Ewert, L. (1998). Development of the cote d'ivoire-ghana transform margin: evidence from the integration of core and wireline log data. *Geological Society, London, Special Publications*, *136*(1), 375-389. doi: 10.1144/GSL.SP.1998.136.01.30

Goodall, T. M., Møller, N. K., & Rønningsland, T. M. (1998). The integration of electrical image logs with core data for improved sedimentological interpretation. *Geological Society, London, Special Publications*, *136*(1), 237-248. doi: 10.1144/GSL.SP.1998.136.01.20

Haller, D., & Porturas, F. (1998). How to characterize fractures in reservoirs using borehole and core images: case studies. *Geological Society, London, Special Publications*, *136*(1), 249-259. doi: 10.1144/GSL.SP.1998.136.01.21

Heald, M. T. (1955). Stylolites in sandstones. *The Journal of Geology*, *63*(2), 101-114. doi: https://www.jstor.org/stable/30080871

Healy, D., Blenkinsop, T. G., Timms, N. E., Meredith, P. G., Mitchell, T. M., & Cooke, M. L. (2015). Polymodal faulting: Time for a new angle on shear failure. *Journal of Structural Geology*, *80*, 57-71. Retrieved from `https://www.sciencedirect.com/science/article/pii/S0191814115300316` doi: https://doi.org/10.1016/j.jsg.2015.08.013

Heidbach, O., Rajabi, M., Cui, X., Fuchs, K., Müller, B., Reinecker, J., ... Zoback, M. (2018). The world stress map database release 2016: Crustal stress pattern across scales. *Tectonophysics*, *744*, 484-498. Retrieved from `https://www.sciencedirect.com/science/article/pii/S0040195118302506` doi: https://doi.org/10.1016/j.tecto.2018.07.007

Hunfeld, L., Foeken, J., & van Kempen, B. (2021, dec). *Geomechanical parameters derived from compressional and shear sonic logs for main geothermal targets in the netherlands* (Tech. Rep. No. -). Utrecht: TNO.

Khoshbakht, F., Azizzadeh, M., Memarian, H., Nourozi, G., & Moallemi, S. (2012). Comparison of electrical image log with core in a fractured carbonate reservoir. *Journal of Petroleum Science and Engineering*, *86-87*, 289-296. doi: https://doi.org/10.1016/j.petrol.2012.03.007

Kilhams, B., Kukla, P., Mazur, S., Mckie, T., Mijnlieff, H., van Ojik, K., & Rosendaal,

E. (2018, 05). Mesozoic resource potential in the southern permian basin area: The geological key to exploiting remaining hydrocarbons whilst unlocking geothermal potential. *Geological Society, London, Special Publications*, *469*, SP469.26. doi: 10.1144/SP469.26

Kombrink, H., Doornenbal, J., Duin, E., den Dulk, M., ten Veen, J., & Witmans, N. (2012). New insights into the geological structure of the netherlands; results of a detailed mapping project. *Netherlands Journal of Geosciences*, *91*(e4), 419-446. doi: https://doi.org/10.1017/S0016774600000329

Kourta, M., & Jocker, J. (2018, February). *Fracture analysis on basis of fmi and sonic scanner* (Tech. Rep. No. -). The Hague: Schlumberger SIS Data services.

Kramers, L., van Wees, J.-D., Pluymaekers, M., Kronimus, A., & Boxem, T. (2012). Direct heat resource assessment and subsurface information systems for geothermal aquifers; the dutch perspective. *Netherlands Journal of Geosciences*, *91*(4), 637–649. doi: 10.1017/S0016774600000421

Kunkel, C., Aehnelt, M., Pudlo, D., Kukowski, N., Totsche, K. U., & Gaupp, R. (2018). Subsurface aquifer heterogeneities of lower triassic clastic sediments in central germany. *Marine and Petroleum Geology*, *97*, 209-222. doi: https://doi.org/10.1016/j.marpetgeo.2018.06.022

Lai, J., Wang, G., Wang, S., Cao, J., Li, M., Pang, X., ... Qin, Z. (2018). A review on the applications of image logs in structural analysis and sedimentary characterization. *Marine and Petroleum Geology*, *95*, 139-166. Retrieved from `https://www.sciencedirect.com/science/article/pii/S0264817218301946` doi: https://doi.org/10.1016/j.marpetgeo.2018.04.020

Laubach, S. E., Lander, R. H., Criscenti, L. J., Anovitz, L. M., Urai, J. L., Pollyea, R. M., ... Pyrak-Nolte, L. (2019). The role of chemistry in fracture pattern development and opportunities to advance interpretations of geological materials. *Reviews of Geophysics*, *57*(3), 1065-1111. Retrieved from `https://agupubs.onlinelibrary.wiley.com/doi/abs/10.1029/2019RG000671` doi: https://doi.org/10.1029/2019RG000671

Laubach, S. E., Olson, J. E., & Gross, M. R. (2009, 11). Mechanical and fracture stratigraphy. *AAPG Bulletin*, *93*(11), 1413-1426. Retrieved from `https://doi.org/10.1306/07270909094` doi: 10.1306/07270909094

Lofts, J. C., & Bristow, J. F. (1998). Aspects of core-log integration: an approach using high resolution images. *Geological Society, London, Special Publications*, *136*(1), 273-283. doi: 10.1144/GSL.SP.1998.136.01.23

Lorenz, J. C., & Cooper, S. (2017). *Atlas of natural and induced fractures in core.* Wiley Blackwell.

Lorenz, J. C., & Cooper, S. (2020). *Applied concepts in fractured reservoirs.* John Wiley and Sons Ltd.

Mahmood, B., Khoshnaw, F., Abdalqadir, M., & Rezaei Gomari, S. (2023, January 21). Natural fracture characterization and in situ stress orientation analysis using fullbore formation micro imager (fmi): a case study on the x oil filed, kurdistan region, iraq. *Arabian Journal of Geosciences*, *16*(2). doi: 10.1007/s12517-023-11178-7

Major, C., Pirmez, C., Goldberg, D., & party, L. . S. (1998). High-resolution core-log integration techniques: examples from the ocean drilling program. *Geological Society, London, Special Publications*, *136*(1), 285–295. doi:

doi:10.1144/GSL.SP.1998.136.01.24

Makel, G. (2007). The modelling of fractured reservoirs: constraints and potential for fracture network geometry and hydraulics analysis. *Geological Society*, *292*(2), 375-403. doi: 10.1144/SP292.21

Maniar, Z. (2019). *Reservoir quality analysis of the triassic sandstones in the nederweert and naaldwijk areas* (Unpublished master's thesis). Delft University of Technology, Delft.

Martin Baron, J. P. (2007). Relationships between stylolites and cementation in sandstone reservoirs: Examples from the north sea, u.k. and east greenland. *Elsevier, Sedimentary Geology*, *194*(1), 17-35. doi: doi:10.1016/j.sedgeo.2006.04.007

Matev, P. (2011). *Comprehensive reservoir assessment of buntsandstein reservoirs in west netherlands basin for geothermal applications in zuid-holland province area* (Unpublished master's thesis). Delft University of Technology, Delft.

Mazaheri, A., Memarian, H., Tokhmechi, B., & Araabi, B. (2015, 08). Developing fracture measure as an index of fracture impact on well-logs. *Energy, Exploration & Exploitation*, *33*, 555-574. doi: 10.1260/0144-5987.33.4.555

Mijnlieff, H. (2020). Introduction to the geothermal play and reservoir geology of the netherlands. *Netherlands Journal of Geosciences*, *99*(e2), 1-23. doi: . https://doi.org/10.1017/njg.2020.2

Nelson, R. A. (2001). *Geologic analysis of naturally fractured reservoirs (2nd edition).* Elsevier. Retrieved from `https://app.knovel.com/hotlink/toc/id:kpGANFRE01/geologic-analysis-naturally/geologic-analysis-naturally`

Olson, J. E. (2004). Predicting fracture swarms — the influence of subcritical crack growth and the crack-tip process zone on joint spacing in rock. *Geological Society, London, Special Publications*, *231*(1), 73-88. Retrieved from `https://www.lyellcollection.org/doi/abs/10.1144/GSL.SP.2004.231.01.05` doi: 10.1144/GSL.SP.2004.231.01.05

Peacock, D., Nixon, C., Rotevatn, A., Sanderson, D., & Zuluaga, L. (2016, 09). Glossary of fault and other fracture networks. *Journal of Structural Geology*, *92*. doi: 10.1016/j.jsg.2016.09.008

Pharaoh, T., Dusar, M., Geluk, M., Kockel, F., Krawczyk, C., Krzywiec, P., ... Van Wees, J. (2010). Tectonic evolution. In J. Doornenbal & A. Stevenson (Eds.), *Petroleum geological atlas of the southern permian basin area* (p. 25-57). Houten: EAGE Publications b.v.

Prioul, R., & Jocker, J. (2009, 11). Fracture characterization at multiple scales using borehole images, sonic logs, and walkaround vertical seismic profile. *AAPG Bulletin*, *93*(11), 1503-1516. doi: 10.1306/08250909019

Purvis, K., & Okkerman, J. (1996a). Inversion of reservoir quality by early diagenesis: an example from the triassic buntsandstein, offshore the netherlands. *Netherlands Journal of Geosciences*, 179-189. doi: 10.1007/978-94-009-0121-6-16

Purvis, K., & Okkerman, J. (1996b). Inversion of reservoir quality by early diagenesis: an example from the triassic buntsandstein, offshore the netherlands..

Rijkers, R., Becker, A., van Campenhout, I., Drijver, B., Heijnen, M., Nieuwland, D., ... Willemsen, S. (2014, 7). *Geothermal energy from triassic aquifers in noord-brabant* (Tech. Rep. No. 1). -: IF technology.

Schlumberger. (n.d.). *Energy glossary.*

Schlumberger. (2001). *Log interpretation principles/applications.* Schlumberger Educational Services. (Porosity and Density)

Schlumberger. (2018, February). *Deviation nlw-gt-01 def geodetic report* (Tech. Rep. No. -). Naaldwijk: Trias Westland.

Spain, D., & Conrad, C. (1997, 9). Quantitative analysis of top-seal capacity: offshore netherlands, southern north sea. *Geologie en Mijnbouw*, *76*, 217-2226. doi: https://doi.org/10.1023/A:1003056609771

Swennen, R., van der Voet, E., Wei, W., & Muchez, P. (2021). Lower carboniferous fractured carbonates of the campine basin (ne-belgium) as potential geothermal reservoir: Age and origin of open carbonate veins. *Geothermics*, *96*, 102147. Retrieved from `https://www.sciencedirect.com/science/article/pii/S0375650521001073` doi: https://doi.org/10.1016/j.geothermics.2021.102147

Tartarotti, P., Ayadi, M., Pezard, P. A., Laverne, C., & Larouziere, F. D. D. (1998). Multi-scalar structure at dsdp/odp site 504, costa rica rift, ii: fracturing and alteration. an integrated study from core, downhole measurements and borehole wall images. *Geological Society, London, Special Publications*, *136*(1), 391-412. doi: 10.1144/GSL.SP.1998.136.01.31

Teama, M. A., Kassab, M. A., Cheadle, B. A., Mesbah, M. A., Mohamed, I. F., & El-Din, E. S. (2018). 3d seismic and formation micro-imager (fmi) integrated study to delineate depositional pattern of abu madi (upper miocene) clastic reservoir rocks in el-wastani gas field, onshore nile delta, egypt. *Egyptian Journal of Petroleum*, *27*(4), 747-758. doi: https://doi.org/10.1016/j.ejpe.2017.11.003

TNO-GDN. (2023a). *Formatie van detfurth. in: Stratigrafische nomenclator van nederland, tno - geologische dienst nederland.* Retrieved 25-01-2023, from `http://www.dinoloket.nl/stratigrafische-nomenclator/formatie-van-detfurth`

TNO-GDN. (2023b). *Formatie van volpriehausen. in: Stratigrafische nomenclator van nederland, tno - geologische dienst nederland.* Retrieved 25-01-2023, from `http://www.dinoloket.nl/stratigrafische-nomenclator/formatie-van-volpriehausen`

Tokan-Lawal, A., Prodanović, M., & Eichhubl, P. (n.d.). Investigating flow properties of partially cemented fractures in travis peak formation using image-based pore-scale modeling. *Journal of Geophysical Research: Solid Earth*, *120*(8), 5453-5466. doi: https://doi.org/10.1002/2015JB012045

van Balen, R., van Bergen, F., de Leeuw, C., Pagnier, H., Simmelink, H., van Wees, J., & Verweij, J. (2000). Modelling the hydrocarbon generation and migration in the west netherlands basin, the netherlands. *Netherlands Journal of Geosciences*, *79*(e1), 29-44. doi: 10.1017/S0016774600021557

van Wijhe, D. H. (1987). Structural evolution of inverted basins in the dutch offshore. *Tectonophysics*, *137*, 171-219.

Vidal, J., & Genter, A. (2018). Overview of naturally permeable fractured reservoirs in the central and southern upper rhine graben: insights from geothermal wells. *Geothermics*, 57-73. doi: 10.1016/j.geothermics.2018.02.003

Vinci, F. (2018, February). *Core analysis nlw-gt-01* (Tech. Rep. No. -). Leiderdorp: PanTerra.

Wentworth. (1922). A scale of grade and class terms for clastic sediments. *The journal of geology*, -. doi: -

Willems, C., Vondrak, A., Mijnlieff, H., Donselaar, M., & van Kempen, B. (2020). Geology of the upper jurassic to lower cretaceous geothermal aquifers in the west netherlands basin - an overview. *Netherlands Journal of Geosciences*, *99*(e1). doi: doi:10.1017/njg.2020.1

Worum, G., Michon, L., van Balen, R. T., van Wees, J.-D., Cloetingh, S., & Pagnier, H. (2005). Pre-neogene controls on present-day fault activity in the west netherlands basin and roer valley rift system (southern netherlands): role of variations in fault orientation in a uniform low-stress regime. *Quaternary Science Reviews*, *24*(3), 473-488. doi: https://doi.org/10.1016/j.quascirev.2004.02.020

Zoback, M. D. (2010). *Reservoir geomechanics*. Cambridge University Press. (In situ stress)

Appendix A

WellCAD

A.1 Image log analysis

A.1.1 Importing Image Logs

Importing FMI DLIS Files

The FMI data is stored in a DLIS file. This can be imported by File > Import. The DLIS header contains information like wellname, service company, ect. Press 'import selection'. For the data import select the following logs: Relative bearing, Hole Azimuth, Hole deviation, the buttons (ABCD pads, rows 1234, so a total of 16) and the corrected buttons, the pad 1 azimuth and the caliper logs.

To process the data go to Process > LIS > BHI Data Processing. Here WellCAD automatically recognises the log names and chooses the correct configuration to orient the data. Press OK. This makes the image log. Adjust the conductivity values to an appropriate range (0-600) to make the images nicely visible and set a appropriate colour scheme.

Importing an image

If your image log is only available as an image this can also be imported in WellCAD. Go to Import, select your image (JPG), select RGB log.

A.1.2 ISI workspace

Orientation picking

To interpret the data, WellCAD creates a ISI Workspace. Press New ISI workspace, select the image log and caliper log you want to interpret and press OK. In this workspace features on the FMI can be interpreted manually. To interpret fractures and bedding orientations a sinosoid can be fitted to the image. By pressing shift and hovering over the fracture a + symbol appears. By clicking on the fracture at the highest and lowest point of the sinusoid, the feature is fitted. Additional clicks can help to better fit the curve. Now by hovering about the curve at the tops and bottoms a ↕ symbol appears. This allows to adjust the steepness of the curve. When hovering at the middle of the curve a cross arrow

symbol appears, this allows to move the curve from position. When pressing shirt + ctrl a ⇳ symbol appears. This allows to measure the aperture of the fracture.

Classification (TadCAD)

The identified features can be grouped by type. This is done within the "Classification", press the blue + symbol, select 'type'. Now when selecting a feature the type can be added by selecting the chosen type. The automatic types are Broken Zone, Major Open Joint, Minor Open Joint, Partially Open Joint, Filled Fracture, Bedding, Induced Fracture. In ToadCAD a customized classification can be made. Go to "New File", enter the Dictonary name you want to use. Make a number of different tadpoles by pressing "Insert Tadpole", to each individual tadpole a colour, size of the pin, and tail can be chosen and named.

Confidence

The confidence levels per feature can be manually adjusted by dragging the confidence bar to the appropriate level. This log can also be used to filter the data by confidence level. By positioning the vertical limit-line, the data is filtered accordingly.

Apparent to True dip

Structural dips picked from an image created in an inclined borehole need to be corrected for the inclination and azimuth of the borehole axis. To do this select "Apparent to True Dip and Azimuth" and select the azimuth and inclination logs, select apparent to the North, name a new log as Output and press "run".

Exporting data

The generated data on the bedding and fractures can be exported by selecting the wanted logs going to Edit > Export log, selecting the wanted logs, pressing OK. This exports the files out of the workspace, now from the main file, you select the wanted logs go to File > Export single log and select the wanted file type.

A.2 Geomechanical properties

To calculate the geomechanical properties first the log data of the sonic logs:V_p and V_s logs and the density log need to be imported. This is done by "File" > "import into Current Document" > "Single file". Here you can select you data set.

The geomechanical properties can be calculated based on the V_p, V_s logs and density log. By going to "Edit" > "insert new generic log" > "formula log". In the window, a formula be entered based on the logs that are already imported.

While doing the calculation make sure to use the correct unit convention.

Appendix B

Stereonet

To interpret the data generated with the FMI interpretation a program called Stereonet is used. This program allows to import the interpreted fracture planes and bedding planes. The dip direction and dip angle can be imported and a stereoplot is generated, poles can be calculated.

Import from excel edit > Paste into dataset > fill in Planes, appropriate decimal point, 1st row with data.

B.1 Unfolding bedding

In the program the fractures can be back-tilted. This can be done by going to "calculations" > "unfold bedding". In the window that opens you need to specify which fractures you want to unfold using which bedding data set. Make sure the bedding data set corresponds to the fracture set as it uses the first bedding input for the first fracture input and the second bedding for the second fracture ect.